Towards solitons in a 2D BEC apparatus

by

Charlotte Alicia Susan O'Neale

A thesis submitted to
The University of Birmingham
for the degree of
DOCTOR OF PHILOSOPHY

Ultracold Atoms Group
School of Physics and Astronomy
College of Engineering and Physical Sciences
The University of Birmingham

January 2015

UNIVERSITY OF BIRMINGHAM

University of Birmingham Research Archive

e-theses repository

Abstract

This thesis presents work towards the realisation of dark solitons in a two-dimensional Bose–Einstein condensate.

The technical redesign of two sets of coils, necessary for magnetic trapping of the atom cloud in order to create a condensate, is reported. Two different types of coil technology are presented, discussed, and used. The fabrication of the coils is described, and each set of coils is characterised. Both sets of coils have been installed on the main experiment and are fully operational.

A key aspect of this thesis is the development of an optical system capable of achieving resolution on the micrometer scale, which can be used for manipulation of a two-dimensional condensate by the method of phase imprinting. The optical system demagnifies the image on a spatial light modulator and focuses the image on the atom plane. Characterisation of the resolution of the optical system shows that a resolution of $3~\mu$m is achieved. The optical system has successfully been implemented on the main experiment and has been used to manipulate the condensate.

A two-dimensional BEC of ^{87}Rb with 31000 atoms and a temperature of 88 nK is realised in a dipole trap of frequencies $\omega_x = 2\pi \cdot 5.8$ Hz, $\omega_y = 2\pi \cdot 19.1$ Hz, $\omega_z = 2\pi \cdot 269.4$ Hz, with gravity being in the z-direction. The method of phase imprinting is used to create the first observed soliton in a 2D BEC. Preliminary analysis of the soliton velocity, width and curvature is presented.

'To Dad'

ACKNOWLEDGEMENTS

CONTENTS

LIST OF FIGURES

LIST OF TABLES

CHAPTER 1

INTRODUCTION AND MOTIVATION

In 1995, the experimental realisation of a Bose–Einstein Condensate (BEC) of ^{87}Rb [1] and a BEC of ^{23}Na [2] opened a door into a quantum world. Bose–Einstein condensates, a state of matter where a macroscopic fraction of the bosons are in the lowest energy state, were first predicted by N. Bose [3] and extended upon by A. Einstein [4] in the 1920s. In practice, this state of matter is obtained at very low ($\approx$100 nK) temperatures.

The 70 year experimental route to a BEC necessitated the development of tools such as the laser [5] to address the atoms, laser cooling in order to slow down and cool the atoms to the mK regime, and controlled evaporative cooling [6] to further cool the atoms down to the required 100 nK regime. In addition to cooling methods, ways of trapping the atoms, such as Magneto-optical traps (MOTs) also needed to be developed [7].

BECs offer access to quantum systems where the strength of the interaction between atoms can be modified by the use of Feshbach resonances [8], as demonstrated in [9, 10]. Optical lattices, laser arrangements which give rise to periodic potentials [11], allow BECs to become quantum simulators, especially since single-site resolution has been achieved [12, 13].

Optical lattices can also be used to create BECs in lower dimensions, as demonstrated in [14] where two-dimensional BECs were obtained. Lower dimension BECs can also be obtained by careful manipulation of the trap potential in which the condensate is formed, as demonstrated by [15], where 2D and 1D BECs of sodium were reported. Lower dimension BECs are of interest because the inter-atomic interactions and excitations are dimension dependent, see References [16, 17]. The intrinsic nonlinearity of a BEC makes them a useful tool for studying nonlinear phenomena, such a vortices [18] or solitons.

Solitons are waves which propagate in one direction through a non-linear medium without broadening. They

were historically observed by John Scott Russell on a canal in Scotland, and are present in many media, such as water, optical fibres, or chains of molecules [19]. Solitons in a Bose–Einstein condensate have attracted significant theoretical interest [20], see References [21, 22] for reviews. Depending on whether the BEC is governed by repulsive (e.g. a ^{87}Rb condensate) or attractive (e.g. a ^{85}Rb condensate) interactions, the soliton will be either dark or bright. A dark soliton is characterised by a density dip or notch, whereas a bright soliton is characterised by a density peak.

The first experimental observations of a dark soliton in a BEC were reported in References [23, 24]. In [23], the BEC was a ^{87}Rb cigar-shaped condensate and the soliton was generated by a technique of phase engineering, named phase imprinting. In [24], the same species of atoms and method of soliton generation were used, however, the condensate was spherical (3D).

The technique of phase engineering consists of changing the phase of the BEC, most often by the use of matter-light interactions [25]. In the original experiments, the solitons were short-lived, with lifetimes of less than 10 ms. Because the solitons decay, they are technically soliton-like matter-waves, but the two terms will be used interchangeably.

Bright solitons have also been experimentally observed in ^{7}Li [26] and in ^{85}Rb [27]. In both cases, the solitons were generated by manipulation of the inter-atomic interactions, by the use of Feshbach resonances.

Dark solitons have also been generated using density engineering, where a density defect is induced on the condensate by the use of slow light (quantum shock) [28].

The creation of long-lived solitons in a cigar-shaped ^{87}Rb BEC [29] allowed a study of the soliton oscillation frequency and of the effects of a head-on collision between two distinguishable dark solitons. The observation of the head-on collisions validated the concept that two solitons collide non-destructively. Collisions between a dark soliton and a bright soliton have also been observed [30].

All of the investigations cited above have been done in cigar shaped condensates. Solitons in 2D (disk-shaped) condensates have attracted significant theoretical interest [31, 32, 33, 34], as the additional physical dimension adds excitations to the BEC, most likely rendering the soliton observable but unstable [35]. Fundamental questions, such as how, and if, solitons interact when crossing could be addressed, as solitons could be made to cross at angles to each other, and not just head on.

This experiment described in this thesis aims to create a ^{87}Rb disk-shaped BEC using novel technologies for the study of solitons, generated by the technique of phase imprinting.

Thesis outline

The structure of this thesis is the following:

- **Chapter 2** presents Bose–Einstein condensation in 3D, the Gross–Pitaevskii equation, and the characteristic properties of a BEC, such as the speed of sound and the healing length. The definition and effect of dimensionality is discussed, along with a focus on collective excitations in a 2D BEC. Solitonic solutions to the non-linear Schroedinger equation are given, along with a discussion of the stability requirements of a soliton.

- **Chapter 3** introduces the experimental apparatus used. The vacuum system is described and characterised. The laser system, methods of atom trapping, and the computer control of the experiment are presented. Methods and protocols for image analysis will also be discussed.

- **Chapter 4** presents the redevelopment of two set of coils carried out as part of this thesis. The chapter includes simulations of the magnetic gradient, design, fabrication and characterisation of both sets of coils. Successful redesign of the coils is achieved.

- **Chapter 5** will present the spatial light modulator and associated set-up utilised in this experiment for the phase imprinting. The chapter will discuss the choice of spatial light modulator (SLM), present tests of the SLM and quantify the resolution of the system.

- **Chapter 6** presents the results of this thesis. The stability of the system is characterised, as is the BEC. Preliminary results of soliton-like features on the BEC are presented and discussed.

- **Chapter 7** presents conclusions and outlook for the experiment.

CHAPTER 2

THEORY

This chapter presents the process of Bose–Einstein condensation in a harmonic trap. The key properties of a condensate are presented. The role of dimensionality on a BEC is discussed, with particular emphasis on condensates in two-dimensions. The Gross–Pitaevskii equation is introduced, and is shown to be part of a category of non-linear equations. Solitonic solutions to the non-linear Schroedinger equation are presented. A brief introduction to the dipole potential is given, in order to understand the principles behind phase imprinting, which will be experimentally used to manipulate the condensate.

2.1 Bose–Einstein condensation

A Bose–Einstein Condensate (BEC) is a state of matter where a macroscopic fraction of the atoms of a cold dilute bosonic gas are in the lowest energy state. In this state, the atoms in the ground state act as an ensemble and display collective behaviour.

Consider the thermal de Broglie wavelengths of the atoms. At high temperatures, the thermal wavelengths of the atoms are short compared to the inter-atomic separation. As the temperature decreases, the de Broglie wavelength increases, see Equation 2.1. If the temperature decreases enough, the thermal wavelength will be greater than the inter-atomic separation, and the wavelengths of the atoms will overlap, and a BEC is formed [36].

The condition for this state of matter to happen in three dimensions is [37]

$$n\lambda_{dB}^3 = n\left(\frac{2\pi\hbar^2}{mk_BT}\right)^{3/2} \geq \zeta_{(3/2)}, \tag{2.1}$$

where n is the density of the atoms, λ_{dB} is the thermal de Broglie wavelength, $\hbar$ is the reduced Planck constant, m is the mass of an atom, k_B is the Boltzmann constant, T is the temperature of the atoms, and ζ is the Riemann Zeta function, with $\zeta_{(3/2)}$ approximately equal to 2.612. From Equation 2.1, it can be seen that the main parameters in creating a BEC are the temperature and density of the atoms. The higher the temperature, the higher the necessary density for the phase transition to occur, with room-temperature atoms needing to be denser than most condensed matter systems for this transition to arise. Consequently, BECs are obtained by reducing the temperature of the system.

The number of bosons in a trap is in general thermodynamically given by Bose–Einstein statistics [38]

$$N = \sum_{n_x, n_y, n_z} \frac{1}{\exp[\beta(\epsilon_{n_x, n_y, n_z} - \mu)] - 1}, \tag{2.2}$$

where $\beta = 1/k_B T$, μ is the chemical potential, and ϵ_{n_x, n_y, n_z} is the energy of a given energy level, with $\epsilon_{n_x, n_y, n_z} = \left(n_x + \frac{1}{2}\right)\hbar\omega_x + \left(n_y + \frac{1}{2}\right)\hbar\omega_y + \left(n_z + \frac{1}{2}\right)\hbar\omega_z$ for a harmonic trap, with ω_i the trapping frequency in the corresponding direction. When the chemical potential, μ, approaches the energy of the lowest state in the harmonic trap ($\epsilon_{0,0,0} = \frac{3}{2}\hbar\frac{\omega_x + \omega_y + \omega_z}{3}$) the lowest state will contain a number of atoms, N_0, which is a large fraction of the total atom number N. Taking N_0 out of the sum yields

$$N - N_0 = \sum_{n_x, n_y, n_z \neq 0} \frac{1}{\exp[\beta\hbar(\omega_x n_x + \omega_y n_y + \omega_z n_z)] - 1}. \tag{2.3}$$

Under the assumption that the number of trapped atoms, N, is large and $k_B T \gg \hbar\omega_{HO}$, namely that the excitations are bigger than the levels fixed by the oscillator lengths, Equation 2.3 can be turned into the integral

$$N - N_0 = \int_0^\infty \frac{dn_x dn_y dn_z}{\exp[\beta\hbar(\omega_x n_x + \omega_y n_y + \omega_z n_z)] - 1} = \int_0^\infty \frac{\rho(\epsilon)d\epsilon}{\exp(\beta\epsilon) - 1}, \tag{2.4}$$

where $\rho(\epsilon)$ is the density of states, which in three dimensions is $\rho(\epsilon) = (1/2)(\hbar\omega_{HO})^{-3}\epsilon^2$. The solution is known to be [38]

$$N - N_0 = \zeta(3)\left(\frac{k_B T}{\hbar\omega_{HO}}\right)^3, \tag{2.5}$$

where $\zeta(n)$ is the Riemann Zeta function, and $\omega_{HO} = (\omega_x \omega_y \omega_z)^{1/3}$ is the geometric average of the trapping frequencies. The critical temperature, namely the temperature at which the BEC will form, is given by imposing the condition $N_0 \to 0$ on Equation 2.5 at the transition, and gives

$$k_B T_c = \hbar\omega_{HO}\left(\frac{N}{\zeta(3)}\right)^{1/3} = 0.94\hbar\omega_{HO}N^{1/3}. \tag{2.6}$$

2.2   The Gross–Pitaevskii equation

So far, no interactions within the BEC have been assumed. In reality, the system will be interacting. Here the focus will be on the weakly interacting system, meaning that the strength of the interaction energy is less than the strength of the kinetic energy. The Gross–Pitaevskii equation [39] governs the behaviour of a weakly interacting BEC and is given by

$$\left[-\frac{\hbar^2}{2m}\nabla^2 + V_{ext}(r) + V_{int}|\Psi(r,t)|^2\right]\Psi(r,t) = i\hbar\frac{\partial}{\partial t}\Psi(r,t), \tag{2.7}$$

where Ψ is the wavefunction of the ground state, V_{ext} is the external potential applied to the atoms (generally the trap potential), and V_{int} is the interaction potential. The interaction potential, commonly denoted as g in the Gross–Pitaevskii equation, is associated with the mean field energy between the atoms and is given by [38, 40]

$$g = \frac{4\pi\hbar^2 a}{m}, \tag{2.8}$$

where a is the s-wave scattering length of the atomic species, which is 5.77 nm for ^{87}Rb [41].

The wavefunction of the condensate can be rewritten as [38]

$$\Psi(r,t) = \psi(r)\exp(-i\mu t/\hbar), \tag{2.9}$$

where ψ is normalised real part of the wavefunction, and μ is the chemical potential. Substituting into Equation 2.7 yields [38]

$$\left[-\frac{\hbar^2}{2m}\nabla^2 + V_{ext}(r) + g\psi^2(r)\right]\psi = \mu\psi. \tag{2.10}$$

It can be noted that when there are no interactions, namely, $g{=}0$, the BEC is again governed by the traditional Schroedinger equation.

2.3 Properties of a BEC

In the Thomas–Fermi limit (the limit in which the kinetic energy term is significantly smaller than the interaction term, and therefore is neglected), the chemical potential is expressed as [36, 42]

$$\mu_{TF} = \frac{1}{2} \left[15\hbar^2 m^{1/2} N \omega_{HO}^3 a \right]^{2/5} = \frac{1}{2} \hbar \omega_{HO} \left(\frac{15Na}{a_{HO}} \right)^{2/5}, \tag{2.11}$$

where N is the number of atoms in the condensate, $\omega_{HO} = (\omega_x \omega_y \omega_z)^{1/3}$ is the geometric mean of the trap frequencies, $a_{HO} = \sqrt{\hbar/(m\omega_{HO})}$ is the harmonic oscillator length, and a is the s-wave scattering length. This expression is of great importance as the chemical potential can be established from known experimental parameters, namely the number of atoms and the trapping frequencies.

The healing length, the shortest distance over which the wavefunction can change [40], is obtained by equating the kinetic energy term $(\nabla^2 \psi = \hbar^2/(2m\xi^2))$ and the interaction term $(gn = 4\pi\hbar^2 an/m)$. It is therefore given by [38, 40, 42]

$$\xi = \sqrt{\frac{1}{8\pi na}} = \sqrt{\frac{\hbar^2}{2mgn}}, \tag{2.12}$$

where n is the density of the atoms, a is the scattering length of the atom, m is the mass of the atom, and g is the coupling constant introduced in Equation 2.8.

The speed of sound, c_s, in a BEC is given by [38, 40, 42]

$$c_s = \sqrt{\frac{gn}{m}} \approx \sqrt{\frac{\mu}{m}}, \tag{2.13}$$

where n is the density of the atoms, and g is the coupling constant.

The three quantities ξ, c_s and μ are related to each other by permutations [42]

$$\xi = \frac{\hbar}{\sqrt{2}mc_s} = \frac{\hbar}{\sqrt{2m\mu}}, \mu = gn = mc_s^2 = \frac{\hbar^2}{2m\xi^2}. \tag{2.14}$$

The timescale associated with the healing length is the correlation time, τ_{corr}, namely the shortest time before which the BEC can react to any external effects, and is given by [42]

$$\tau_{corr} = \frac{\xi}{c_s} = \frac{\hbar}{\sqrt{2}\mu} \tag{2.15}$$
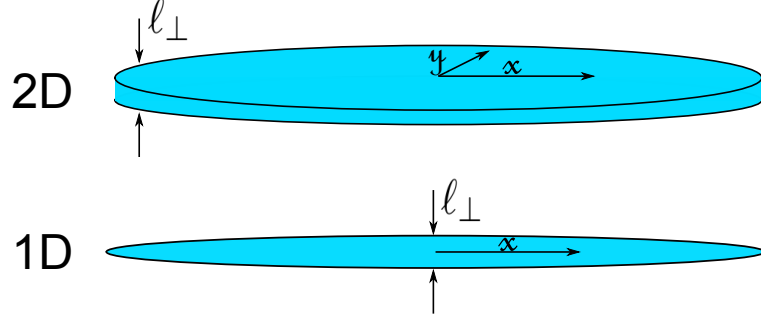
Figure 2.1: Definition of $\ell_\perp$ for different dimensions: (top) in the 2D case, and (bottom) in the 1D case. After Reference [44].

2.3.1 Dimensionality

Strictly speaking a BEC is only a 3D object. However, macroscopic fractions can be obtained in lower dimensions [38].

Experimentally, the production of a 3D, 2D or 1D BEC is dependent on the shape of the trap. If $k_B T$ is smaller than one oscillator energy, $\hbar\omega$, then the BEC is said to be 2D [38, 43]. If $k_B T$ is smaller than two oscillator energies the BEC is said to be 1D [38].

Equivalently, a lower dimensional regime is reached when the chemical potential in the dimension (i.e. μ_{2D} or μ_{1D}) is smaller than the confining oscillator energies, i.e. $\mu_{2D} \ll \hbar\omega_\perp$ for a 2D BEC, and $\mu_{1D} \ll \hbar\omega_\perp$ for a 1D BEC, where $\omega_\perp$ is the confining dimension(s), see Figure 2.1 [44].

As the dimensionality changes, the interaction also changes. The temperatures at which BECs are obtained, as well as key properties of the BECs, are therefore expected to change with dimensionality.

In the 2D case, the second integral in Equation 2.4 can be solved in the presence of a harmonic potential, hence a true BEC can be obtained in 2D in the presence of a harmonic trap [38]. Experimental 2D BECs have been observed, with the first reported one being by Görlitz *et al* [15]. One of the consequences of this change in the dimensionality is that the critical temperature is no longer given by Equation 2.6, but by [38, 44]

$$k_B T_{2D} = \hbar\omega_{2D} \left(\frac{N}{\zeta(2)}\right)^{1/2}. \tag{2.16}$$

The Thomas–Fermi chemical potential is no longer given by Equation 2.11 but by [45]

$$\mu_{TF}^{2D} = 2\hbar\omega_r \left(\frac{Na}{\sqrt{2\pi}a_z}\right)^{1/2}, \tag{2.17}$$

where $\omega_r = (\omega_x \cdot \omega_y)^{1/2}$ is the frequency in the plane of the BEC, and $a_z = \sqrt{\hbar/(m\omega_z)}$ is the oscillator length

Dimension	Speed of sound	Healing length	Coupling constant	Density
3D	$c_s^{3D} = \sqrt{\frac{gn}{m}} \approx \sqrt{\frac{\mu}{m}}$	$\xi_{3D} = \sqrt{\frac{1}{8\pi na}} = \sqrt{\frac{\hbar^2}{2mgn}}$	$g_{3D} = \frac{4\pi\hbar^2 a}{m}$	n_{3D}
2D	$c_s^{2D} = \sqrt{\frac{3}{2}}\sqrt{\frac{\mu_{3D}}{m}}$ [1]	$\xi_{2D} = \sqrt{\frac{2m\mu_{3D}}{3}}\xi_{3D}$	$g_{2D} = \frac{g_{3D}}{\left(\sqrt{2\pi}\ell_\perp\right)^{3-2}}$ [2,3]	$n_{2D} = \frac{3\sqrt{2\pi}l_\perp}{2}n_{3D}$
1D	$c_s^{1D} = \frac{1}{\sqrt{2}}c_s^{3D}$ [4]	$\xi_{1D} = \sqrt{2}\xi_{3D}$ [5]	$g_{1D} = \frac{g_{3D}}{2\pi\ell_\perp^2}$ [6]	$n_{1D} = \pi a_{HO}^2 n_{3D}$ [7]

Table 2.1: Expressions of key properties of the BEC, in a dimension dependent format.

in the confining direction.

In the 1D case, even the presence of a harmonic potential does not allow the integral of Equation 2.4 to be solved, hence a pure BEC cannot be obtained in 1D. However, large macroscopic fractions of atoms can be in the ground state, hence a BEC is experimentally achievable. The critical temperature in the 1D case is given by [38]

$$k_B T_{1D} = \hbar\omega_{1D}\frac{N}{\ln(2N)}. \tag{2.18}$$

The key properties of a BEC described in Section 2.3 are dimension dependent [42]. Table 2.1 collates the key properties for different dimensions.

2.3.2 2D BECs

As this experiment aims to produce a two-dimensional condensate, attention to the properties and regimes of 2D BECs will now be given.

Key properties

A 2D BEC is not superfluid at all temperatures. It is only superfluid at temperatures well below the (2D) critical temperature T_c, where the phase fluctuations are small [48]. Between this low temperature regime and the critical temperature, the 2D BEC displays phase fluctuations and is considered to be a quasi-condensate [48]. This has been confirmed experimentally [49], where a 2D BEC of sodium atoms displays a bimodal distribution at temperatures below T_c and a trimodal distribution at temperatures well below T_c, associated with the onset of superfluidity.

The phase transition from quasi-condensate to superfluid condensate is called the Berezinskii–Kosterlitz–

---

[1] See Reference [46].
[2] $\ell_\perp = \sqrt{\hbar/(m\omega_\perp)}$.
[3] See References [44, 47].
[4] See Reference [42].
[5] See Reference [42].
[6] See References [44, 47].
[7] See Reference [42].

Thouless (BKT) transition[1]. It is associated with the pairing of vortices, and occurs when the quantity $n_s \lambda_T^2$ jumps from 0 to 4, where n_s is the superfluid density and $\lambda_T = h/\sqrt{2\pi m k_B T}$ is the thermal wavelength [43, 14]. The superfluid density is not to be confused with the total density, as the total density at the critical point will vary depending on the strength of the interactions, see Reference [43] for details.

The BKT transition has been experimentally studied in 2D ^{87}Rb BECs obtained by splitting a 3D cloud into 2D BECs by the use of an optical lattice [14].

Dynamics

Depending on how the confining oscillator length, $\ell_\perp$ compares to the 3D scattering length, a, the 2D BEC can be thermodynamically 2D but collisionally 3D ($\ell_\perp > a$) or can be both thermodynamically and collisionally 2D ($\ell_\perp < a$) [44]. As the case of both thermodynamically and collisionally 2D is exotic [44], and will not be the case for the BEC reported here, it will not be considered further. A theoretical study can be found in References [16, 17].

Collective excitations in a 2D BEC

Collective excitations of a BEC allow the characterisation of the trap frequencies. The lowest collective excitation is the dipole excitation, caused by the trapping frequencies, ω_0. It is due to motion of the centre-of-mass, and does not depend on the interaction energy of the system [50], or the dimensionality. It has been experimentally studied for ^{87}Rb atoms in a disk-shaped trap [51] and for sodium atoms in a cylindrical trap [52]. Theoretical predictions of a dipole frequency of $\omega_{dipole} = \omega_0$ are in good agreement with the experiments.

There are three other low energy collective excitation modes in a 2D BEC, the monopole ('breathing') mode, the quadrupole mode, and the scissor mode, all illustrated in Figure 2.2. The monopole, or breathing, mode is a compression mode [50] where the two in-plane frequencies oscillate in phase. In 2D, the monopole mode has an oscillation frequency of $\omega_{monopole} = 2\omega_r$, where ω_r is the geometric average of the trap frequencies in the 2D plane [55, 50]. The quadrupole mode is a compression mode where the frequencies oscillate out of phase. The frequency of the quadrupole mode is $\omega_Q = \sqrt{2}\omega_r$ [53, 55, 50]. The scissor mode is a signature of superfluidity [53] and oscillates with a frequency of $\omega_s = \sqrt{\omega_y^2 + \omega_x^2}$.

---

[1]Also referred to as the KT transition.
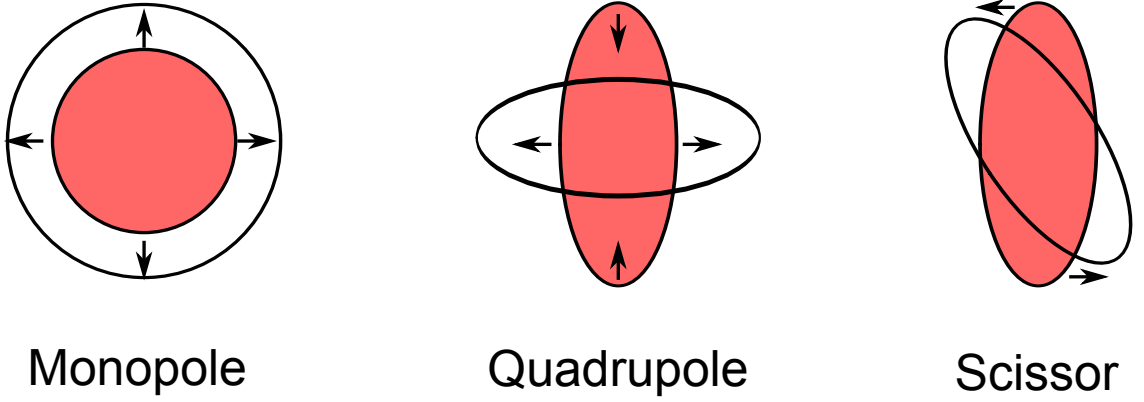
Figure 2.2: Schematic representation of collective excitations in a 2D BEC. After References [53, 54].

2.4 The non-linear Schroedinger equation

2.4.1 From the Gross–Pitaevskii equation to the non-linear Schroedinger equation

As can be seen from the Gross–Pitaevskii equation introduced in Equation 2.10, the wavefunction $\Psi(r,t)$ has a non-linear dependence on the interaction term V_{int}. This makes the GPE part of a class of equations known as the Non-Linear Schroedinger (NLS) equations.

2.4.2 Solutions to the NLS equation: solitons

The Non-linear schroedinger equation is generically given by [56]

$$E\Psi = \left[-\frac{\hbar^2 \nabla^2}{2m} + \kappa |\Psi|^2 \right] \Psi, \tag{2.19}$$

where E is the energy, m is the mass of the particle, Ψ is the wavefunction, and κ is the coefficient of the non-linear term. Comparing Equations 2.10 and 2.19, one can notice that the NLS equation is the Gross–Pitaevskii equation with $V_{ext} = 0$, and $\kappa = V_{int}$. The external potential, V_{ext}, in which the BEC is formed is designed to vary adiabatically over the extent of the condensate. It can therefore be neglected in this discussion.

Equation 2.19 is a 3D equation. Reducing it to a 1D problem for mathematical simplicity yields

$$E\Psi(x) = \left[-\frac{\hbar^2}{2m} \frac{\partial^2}{\partial x^2} + \kappa |\Psi(x)|^2 \right] \Psi(x). \tag{2.20}$$

The Non-linear Schroedinger equation has two solitonic solutions, depending on the sign of the non-linear coefficient. A soliton is a wave which does not disperse as it propagates, and is maintained due to a balance of the kinetic energy and the inter-particle interactions.

In the case of a negative scattering length, namely an attractive BEC or a focusing medium, the solution to the NLS is [56, 57]

$$\psi(x,t) = \frac{\ell_r}{\sqrt{2|a|\kappa}} sech\left(\frac{x - vt}{\kappa} \right) \exp\left[i \frac{mv}{\hbar} x - \frac{i}{\hbar} \left(\frac{mv^2}{2} - \frac{\hbar^2 \kappa^2}{2m} \right) t \right], \tag{2.21}$$

where a is the (negative) scattering length, ℓ_r is the radial harmonic oscillator length, κ is the soliton width, and v is the velocity of the soliton.

This solution gives rise to a 'bright soliton', so called because it is characterised by a rise in the local density. Because ^{87}Rb does not form an attractive BEC, no further consideration to bright solitons will be given. The NLS equation solution in the case of a positive scattering length, namely a repulsive BEC or defocusing medium, is [30]

$$\Psi(x,t) = \sqrt{n_0} \left\{ i\frac{v}{c_s} + \sqrt{1 - \frac{v^2}{c_s^2}} \tanh\left[\frac{\sqrt{1 - \frac{v^2}{c_s^2}}}{\xi} (x - q(t)) \right] \right\} e^{-ign_0 t/\hbar}, \tag{2.22}$$

where n_0 is the peak density of the BEC, v is the velocity of the soliton, q is the position of the soliton, c_s is the 1D speed of sound, ξ is the 1D healing length, and g is the 1D interaction term. Plotting $|\Psi(x,t)|^2$ for different values of v/c_s yields the graph shown in Figure 2.3. Depending on the value of v/c_s, the soliton has different depths. A black soliton, a soliton which does not move and where the density dip goes all the way to zero, it obtained when $v/c_s = 0$. The smaller the v/c_s ratio, the deeper the soliton.

By plotting the phase of $\Psi(x,t)$ at different values of v/c_s the graph shown in Figure 2.4 is obtained. The case of a black soliton corresponds to a phase of π.
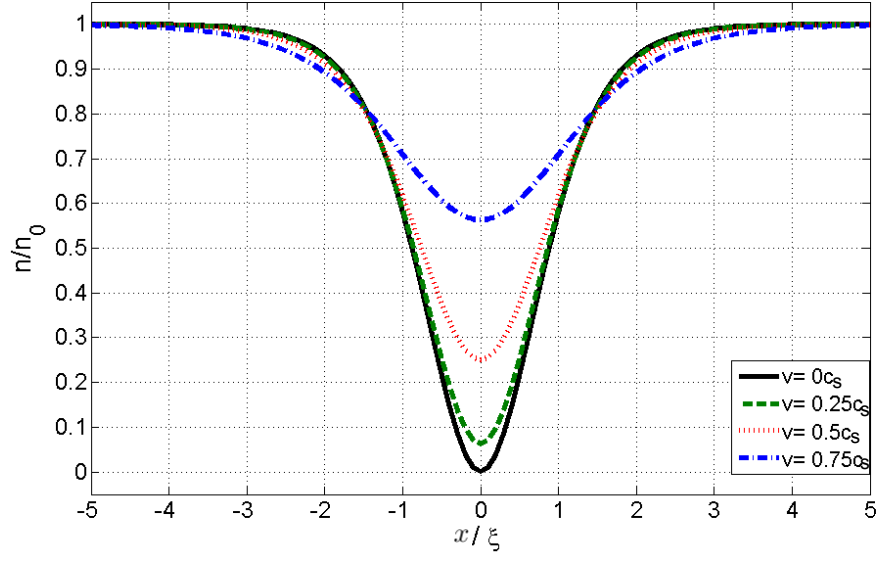
Figure 2.3: Depth of the soliton for different v/c_s ratios. It can be noted that the smaller the v/c_s ratio, the deeper the soliton.
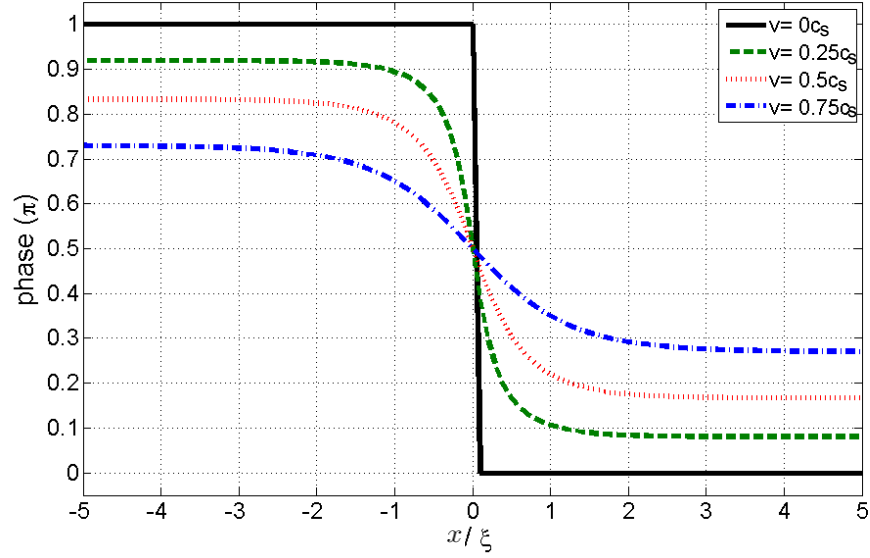
Figure 2.4: Phase across the soliton for different v/c_s ratios. It can be noted that the smaller the v/c_s ratio, the sharper the feature.

The width of the soliton is given by [20, 42]

$$\kappa = \frac{\hbar}{mc_s\sqrt{1 - \left(\frac{v}{c_s}\right)^2}} = \frac{\sqrt{2}\xi}{\sqrt{1 - \left(\frac{v}{c_s}\right)^2}}, \tag{2.23}$$

13

where ξ is the dimensionally-corrected healing length. It can be seen that the size of the soliton is closely linked to the size of the healing length. The density of the soliton, n_s, is given by [42]

$$\frac{n_s}{n_0} = 1 - \left(\frac{v}{c_s}\right)^2 = \sin^2(\phi/2), \tag{2.24}$$

where n_0 is the dimensionally-corrected density, and ϕ is the applied phase shift. Equation 2.24 can also be used to assess the phase shift from the soliton velocity.

2.4.3 Stability of a soliton

Theoretical studies have shown that solitons are unstable to the transverse excitations of the BEC [35, 58, 59]. It is therefore recommended that the radial degrees of freedom be suppressed by tight confinement in two dimensions, resulting in 1D-BECs [35] in order to observe long lived, stable solitons. Long-lived solitons have been experimentally observed in References [29, 30, 60].

In higher dimensions, specifically 2D, the soliton is unstable, and is therefore technically a solitary wave and not a soliton. However, the terms are used interchangeably. The instability, known as the 'snake instability' causes the unstable soliton to decay to more stable structures, such as vortices [58, 59]. The instability is so called because the originally straight soliton curves, due to the difference in density across the BEC, and ultimately bends (or 'snakes') to the point where is breaks up into vortices. This has been experimentally observed by [61, 62].

An additional source of soliton instability is interactions with the thermal cloud. The soliton can couple with the surrounding thermal cloud, causing damping and therefore decay of the soliton [58, 63]. The lower the temperature, and the higher the BEC fraction, the less important this effect will be.

2D solitons

Solitons in 2D BECs have attracted significant theoretical interest. G. Huang *et al* [32] have theoretically modelled a 2D soliton moving only in the x-direction by

$$\Psi(x) = u_0 \left(1 - \frac{p^2}{2c_s^2} sech^2(K)\right) \exp\left(-x^2 - i\mu t - i\frac{p}{c_s} \times \tanh(K)\right), \tag{2.25}$$

where

$$K = p\left[x - c_s\left(1 - \frac{p^2}{2c_s^2}\right)t - x_0\right]. \tag{2.26}$$

14

The parameter p determines the greyness of the soliton ($0 \leq p^2 \leq 2c_s^2$), and u_0 is the ground state configuration of the condensate.

The study showed that, with repulsive 2D BECs in the Thomas–Fermi limit, the soliton decays when it interacts with the boundary in the case of a low-depth soliton, and that a high-depth soliton decays due to the snake instability.

2.5 Creation of solitons

Having defined what a soliton is and discussed some of its properties, experimental methods for generating solitons will now be considered.

As seen from Section 2.4.2, a soliton corresponds to a change in the density of the condensate, associated with a change in phase. Because it is associated with a change in phase, a way of generating a soliton is to manipulate the phase of the BEC so as to recreate the phase slip. This is best done by the use of light-matter interactions, by the use of a technique commonly known as 'phase imprinting', and previously demonstrated in References [23, 24], for example.

2.5.1 Phase imprinting

The technique of phase imprinting, illustrated in Figure 2.5, relies on applying a light potential (the dipole potential) on only part of the BEC, thus creating a phase difference across the condensate. The phase of the exposed part of the BEC will evolve according to [42]

$$\psi(z,t) = \psi(z,0)e^{-i\phi} = \psi(z,0)e^{-\frac{i}{\hbar}U_{dip}(z)t_{pulse}}, \tag{2.27}$$

where ψ is the wavefunction, U_{dip} is the dipole potential (discussed below), and t_{pulse} is the duration for which the light field is applied. As can be seen, the phase of the imprint can therefore be variable, depending on the time of the imprint, or on the strength of the dipole potential U_{dip}. In order to imprint a phase shift of π, the condition $\phi = U_{dip}t_{pulse}/\hbar = \pi$ needs to be fulfilled. The form of U_{dip}, arising from matter-light interactions will now be discussed.

2.5.2 Dipole potential

This Section is based on Reference [64]. An electric field $\mathbf{E}$ of a light source of frequency ω will induce an dipole moment $\mathbf{p}$ in the atom, which will oscillate with the same frequency as the light source. The amplitude
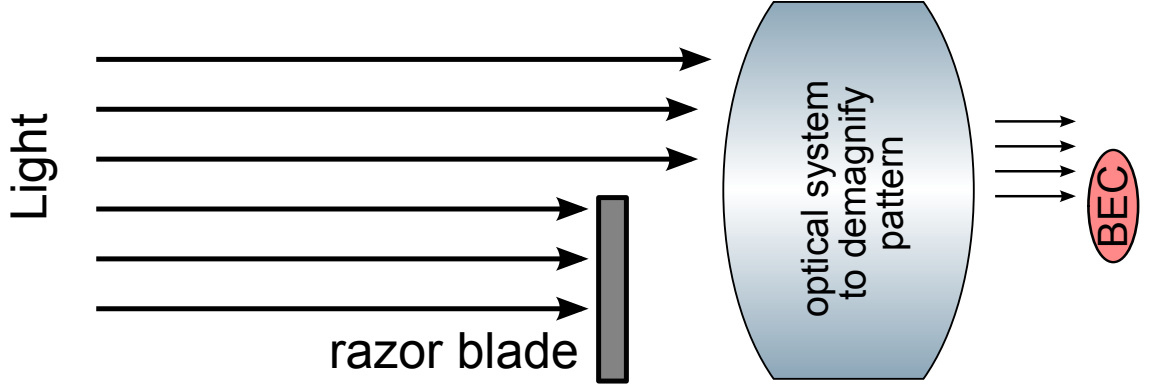
Figure 2.5: Schematic representation of the principle of phase imprinting. Light is shone on only part of the BEC, with a razor blade [24] or a pattern from a spatial light modulator [23] used to block the light. The optical system to demagnify the pattern will be discussed in Chapter 5.

of the dipole $\tilde{p}$ is given by

$$\tilde{p} = \alpha \tilde{E}, \tag{2.28}$$

where $\tilde{E}$ is the amplitude of the electric field, and α is the complex polarizability.

The interaction between the dipole and the electric field is given by [64]

$$U_{dip} = -\frac{1}{2} \langle \mathbf{pE} \rangle = -\frac{1}{2\varepsilon_0 c} Re(\alpha) I, \tag{2.29}$$

where I is the field intensity, given by $I = 2\varepsilon_0 c |\tilde{E}|^2$, and the factor of $1/2$ reflects the oscillating, rather than permanent, nature of the dipole. In the rotating wave approximation (RWA), which stipulates that the light be near detuned ($\Delta = |\omega_0 - \omega_L| \ll \omega_0$), the dipole potential can be rewritten as

$$U_{dip}(r) = \frac{3\pi c^2}{2\omega_0^3} \frac{\Gamma}{\Delta} I(r), \tag{2.30}$$

where ω_0 is the optical transition frequency, Γ is the linewidth (spontaneous decay rate) of the excited state of the atom, Δ is the detuning of the applied light compared to the transition frequency, and I is the intensity of the light. From Equation 2.30, it can be seen that all the constants are known, with the detuning and the intensity profile being the two experimentally controllable variables.

2.6　Conclusion

This chapter has presented the formation of a condensate in 3 dimensions, and discussed the criteria and consequences of being in lower dimensions, with emphasis placed on a two-dimensional condensate. The key properties of a condensate, such as the coupling constant, the healing length, the chemical potential, the speed of sound, and the correlation time have been presented in all three dimensions. The Gross–Pitaevskii equation has been presented, and it has been shown that it is part of the more general class of non-linear equations. Solitonic solutions to the non-linear Schroedinger equation have been presented, and the stability of a soliton has been discussed.

<center>CHAPTER 3</center>

<center># THE EXPERIMENTAL SET-UP</center>

This chapter aims to introduce the experimental set-up used in this project. The vacuum chambers are presented, and the quality of the vacuum is discussed. The laser system and optics used for magneto-optical trapping of the atoms are described. The different coils used for magnetic trapping of the atoms are described, along with the dipole trap which is used to trap the condensate. The detection system for imaging the atoms is introduced, with some relevant background information. The computer control of the experiment is briefly described.

3.1 The vacuum system

Vacuum is a necessary condition for most cold atoms experiments. In air, collisions between the atoms held in a magnetic trap and the background gas excite the atoms out of the trap, resulting in atom loss. In vacuum, as the quantity of background gas is decreased, so are the collisions which excite the atoms out of the trap [39]. The ultra-high vacuum system is therefore an integral part of the experimental apparatus.

3.1.1 The vacuum system

The vacuum system [65] is designed to be compact, especially in thickness, as this allows smaller magnetic fields, and therefore coils, to be used. It is also designed to maximise the available optical access [66]. A rendering of the experimental system is shown in Figure 3.1.

The dispensers[1] are housed at the top of the experiment. The system has a lead sealed 2D MOT chamber [65] and an indium sealed 3D MOT chamber [66] with a differential pumping stage in between the two. In order to have a versatile detection system, a glass cell is also present, with a 16 mm diameter differential

---

[1] two rubidium dispensers from SAES getters and one enriched Potassium-40 source from Alvatech
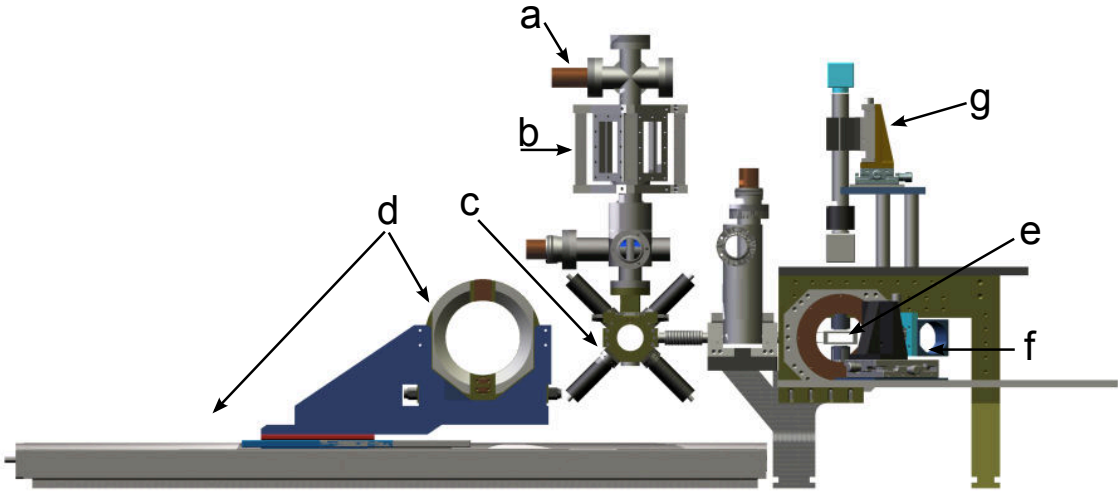
Figure 3.1: Schematic drawing of the experimental set-up. (a) the dispensers, (b) the 2D MOT chamber and permanent magnets, (c) the 3D MOT chamber, coil and telescopes, (d) the moving coils on the rail, (e) the glass cell, (f) the dipole trap, and (g) the vertical detection system. Not shown: the vertical illumination and the horizontal detection systems.

pumping stage between it and the 3D MOT chamber [65]. The glass cell[1] is epoxy sealed, 33 mm thick, 23 mm high and 60 mm long, and features a series of anti-reflection coatings.

3.1.2 Characterisation of the vacuum

In the experiment, the vacuum is monitored by the gauges present on the ion pumps. As shown in Figure 3.2, the values read by the gauges fluctuate with humidity in the room, which limits the reliability of the measurement.

A more accurate and relevant measurement of the quality of the vacuum is obtained by studying the rate of loss of atoms from a magnetic trap [39]. Every time a collision between a trapped atom and a background atom occurs, the trapped atom will be lost from the trap. The higher the pressure, the more background atoms, the shorter the time between collisions. By holding the atoms in the trap for different lengths of time and counting the number of atoms for each hold time, the rate of loss is established. This measurement is called a lifetime measurement. The number of atoms is counted by the use of absorption imaging, which will be described in Section 3.4.2.

With an experimental cycle taking roughly 1 to 1.5 minutes, and with the evaporative stages in the glass cell taking 20 seconds, lifetimes less than 30 seconds are not acceptable, as they would lead to too high an atom

---

[1]Japan Cell.
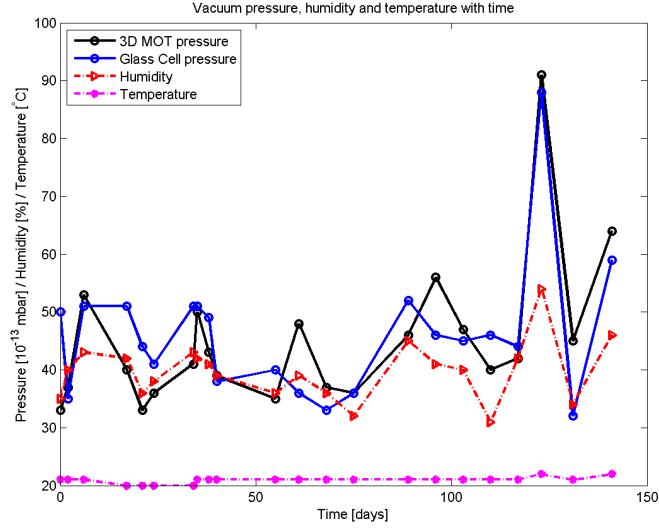
Figure 3.2: Pressure readings from the gauges of the ion pumps, humidity and temperature as a function of time.

number loss due to background gas as well as any pertaining to the evaporative cooling process.

The lifetime of the atoms in the glass cell lowers over time. Fourteen months after the main baking of the system, a lifetime measurement showed a lifetime of 17.5 s, see Figure 3.3, which is too low for the experiment to run successfully. Having eliminated that stray light or magnetic fields could be responsible for the shortened lifetime, it was deduced that there had to be a vacuum issue, even if the pressure readings from the gauges indicated vacuum to the order of 10^{-12} mbar.

The original vacuum system failed because of the epoxy at the MOT chamber allowing water vapour to diffuse into the vacuum over time, as discussed in detail in [65]. The glass cell is held together with epoxy, so it is feasible that this phenomenon is occurring at the glass cell, but with a longer time scale than the original epoxy MOT.

In order to increase the lifetime in the glass cell, it was baked to 100 °C, so that water present in the epoxy could evaporate out. The lifetime experiment was carried out after the bake and gave a lifetime of 48.9 s, see Figure 3.3.

Vacuum monitoring with lifetime measurements (Figure 3.3) shows that suitable vacuum lasts for 7 months. Recordings from the less reliable vacuum gauges (Figure 3.2) also indicate a slight rise in pressure over that time period, once variations due to humidity are accounted for.
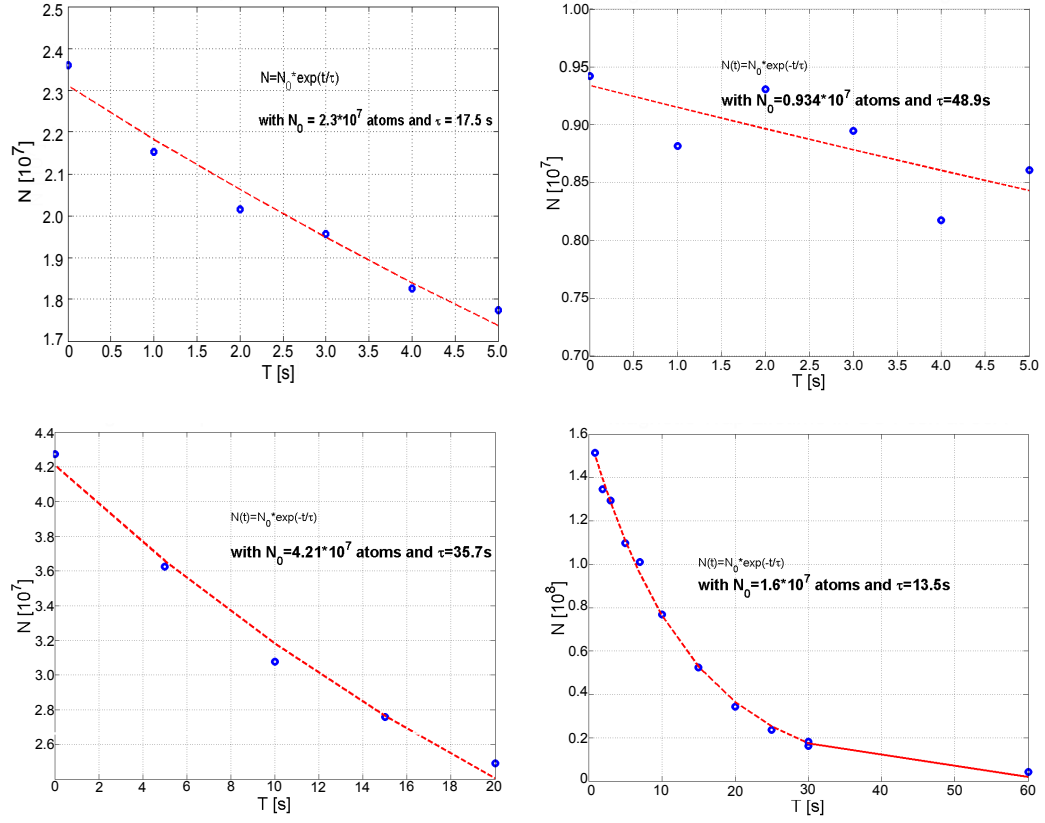
Figure 3.3: Lifetime of the atoms. From left to right, top to bottom: before the first glass cell bake; straight after the glass cell bake; four months after the glass cell bake; and seven months after the glass cell bake.
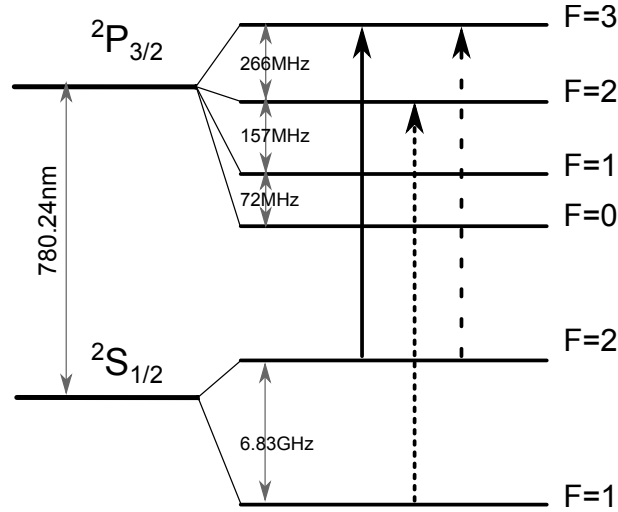
Figure 3.4: ^{87}Rb D2 line diagram, showing the frequencies of the transitions: the cooling transition (full line); the repumper transition (dashed line); and the pushing, optical pumping and imaging transition (dotted line). All numbers taken from Reference [67].

3.2 Laser system

3.2.1 Rubidium-87

The species used in this experiment is the alkali ^{87}Rb, which has a positive s-wave scattering length of 5.77 nm [41], resulting in a repulsive interaction BEC. The level diagram for the D2 line of ^{87}Rb is shown in Figure 3.4.

In order to cool the atoms down from room temperature to BEC temperature, i.e. from $\approx$100 K to less than 100 nK, laser cooling followed by evaporative cooling is employed. In laser cooling of ^{87}Rb two transitions are addressed: the $|^2S_{1/2}, F = 2 >$ to $|^2P_{3/2}, F = 3 >$ (cooling) transition and the $|^2S_{1/2}, F = 1 >$ to $|^2P_{3/2}, F = 2 >$ (repumper) transition, both of which are also shown on Figure 3.4. The $|^2S_{1/2}, F = 2 >$ to $|^2P_{3/2}, F = 3 >$ transition is also used for resonant absorption imaging of the atoms and optical pumping.

3.2.2 The laser system

The laser system is stable, compact, and modular, allowing for versatility in the set-up. Full details can be found in Reference [66]. Each module performs a designated task (e.g. stabilising light, distributing light) and the light is fibre-coupled from one module to the next.

The logic diagram of the laser system is shown in Figure 3.5. The first module, the master module, ensures that the reference light, and therefore all subsequent light, is of a stable and selected frequency. The external

cavity diode laser (ECDL) [66, 68] is stabilised via frequency modulation spectroscopy [69] to the crossover transition CO23 ^{87}Rb atomic transition via a cell of rubidium.

In order to stabilise the cooling light, the reference light from the master module is beaten with light generated by the DFB (distributed feedback) laser diode in the cooling light module. The beat frequency is then stabilised with an offset lock technique via a voltage-controlled oscillator (VCO) [66, 70]. The presence of the VCO allows the frequency of the cooling light to be tuned on a scale of hundreds of MHz. The same process is done in parallel to generate the repumping light.

In order to have enough power at the experiment, the light is then amplified by a tapered amplifier. Owing to losses due to the fibre-coupling between each module, the typical light power after the amplifier is of the order of 1 W. Because significantly more cooling light is needed at the experiment, the cooling light undergoes two stages of amplification.

The amplified light is then distributed to different distribution modules. In these modules, the cooling and repumping light both go through a double pass (acousto-optic modulator) AOM before being combined and fibre-coupled to the relevant part of the experiment. The presence of the AOMs allows switching and further control of the frequency of the light, with approximately 40 MHz range allowed. The distribution modules also feature shutters to ensure that no stray light goes to the experiment.

3.2.3   The MOT optics

The 2D MOT optics consist of two beams which contain both the cooling and repumping light, a $\lambda/4$ waveplate to circularly polarise the light, two cylindrical lenses to elliptically expand the beams, and two large prisms to retro-reflect the beams. The position of the beams can be adjusted by two steering mirrors present in both beam paths. Full details can be found in Reference [66].

A pushing beam is mounted at the top of the vacuum chamber and is used to push the atoms from the 2D MOT into the 3D MOT.

The light at the 3D MOT is given by three pairs of beams: one axial pair, and two cross pairs. All have circularly polarised light. The axial light is collimated by a telescope and back-coupled, indicating that the two telescopes are sufficiently well aligned that the light from the one can be coupled into the fibre of the other. The two cross pairs are fixed directly onto the 3D MOT chamber. This light is divergent, primarily due to space constraints [66].
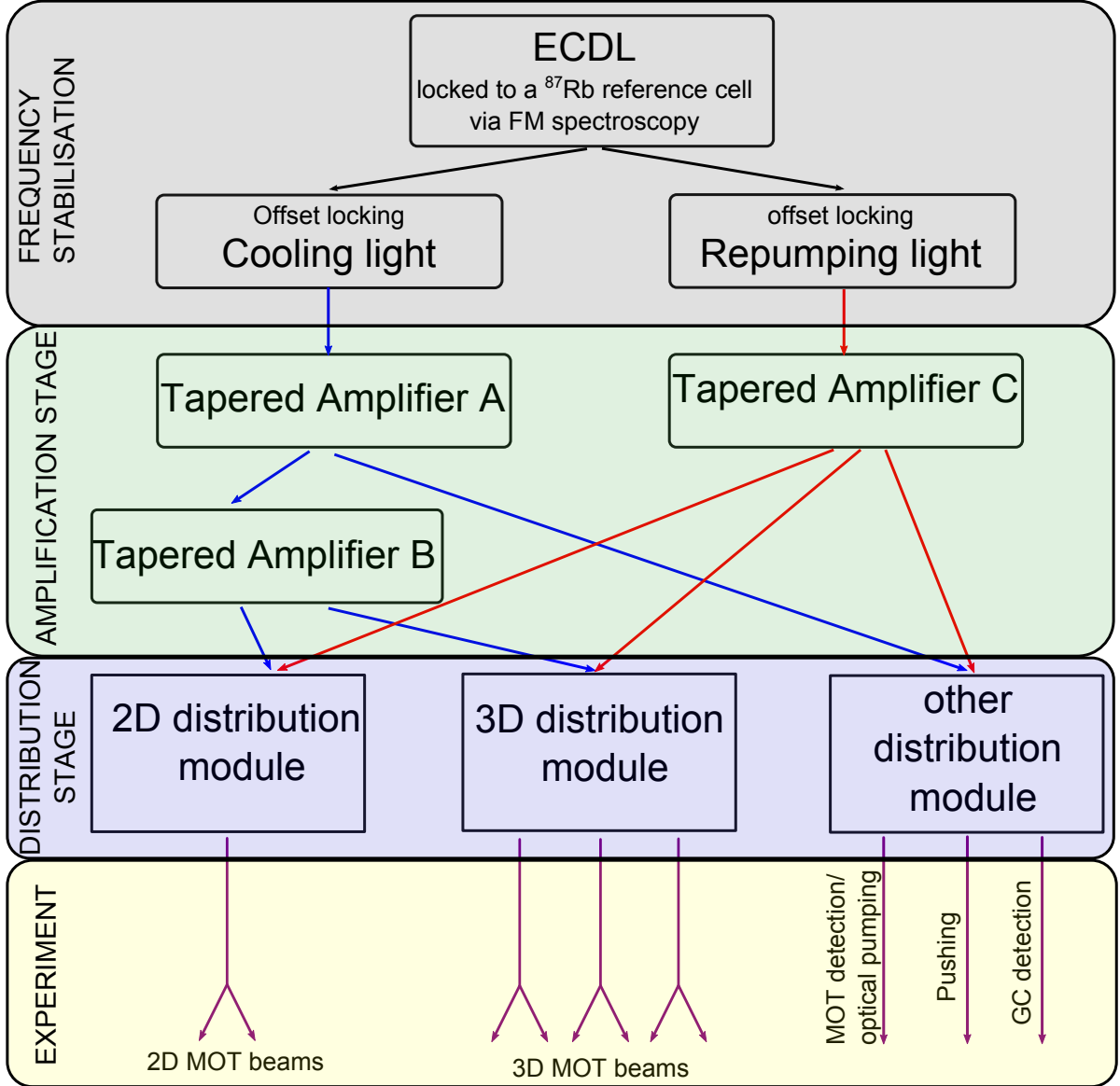
Figure 3.5: Laser system logic diagram: in the frequency stabilisation stage, frequency stabilised light is generated for both the cooling and repumping transitions. The light is then amplified in the amplification stage by tapered amplifiers before being combined and distributed in the distribution modules. The light is then sent to the experiment. All light is fibre-coupled between stages.

3.3 Trapping of cold atoms

Two different methods of trapping atoms are used in this thesis work: magnetic trapping and trapping via a dipole trap.

3.3.1 Magnetic fields

The experiment features various techniques to produce magnetic fields. In the 2D MOT, four sets of permanent magnets create a 2D quadrupole field [65]. In the 3D MOT, the 3D MOT coils [66] are designed in an anti-Helmholtz configuration and define the magnetic centre of the MOT trap. Around the 3D MOT chamber, three sets of compensation coils (one in each direction) are present to aid temperature optimisation in the molasses phase, by compensating for residual magnetic fields [66]. In order to move the atoms from the 3D MOT chamber to the glass cell, another set of anti-Helmholtz coils, named the moving coils, are used. These coils are on a rail which allows precision positioning and motion of the coils [71]. At the glass cell, a further set of anti-Helmholtz coils, called the Feshbach coils, is present. A small pick-up coil used for RF evaporation rests on the glass cell.

Owing to leaking of the coolant, both the moving coils and Feshbach coils have been reworked as part of this thesis. Full details are given in Chapter 4.

3.3.2 The dipole trap

A dipole trap, the full details of which can be found in Reference [71], is used in the final stages of the BEC experimental protocol. Such a trap is used because, unlike an anti-Helmholtz magnetic trap, it avoids Majorana spin flip [72] losses[1], and the trap can be made to produce two- or three-dimensional clouds.

Far detuned 1550 nm light is focused onto the atom cloud via cylindrical and aspherical lenses, which produce an astigmatic beam with two foci, 4 mm apart in the propagation direction. The original trap had a power of 5 W, featured a seed laser, an amplifier, and a computer controlled AOM.

Improvements to the power were made by splitting the seed light in the splitting module and adding a second amplifier and combining this beam with the original beam, resulting in a total power of 10 W. Both set-ups are shown in Figure 3.6. The waists remain unaffected by the change in power. The 10 W trap frequencies are $\omega_x = 2\pi \cdot 72$ Hz, $\omega_y = 2\pi \cdot 110$ Hz, and $\omega_z = 2\pi \cdot 3.3$ kHz.

---

[1]Other traps, such as TOP traps [73], Ioffe–Pritchard traps [74, 39] QUIC traps [75] or plugged traps [76] can also be used to avoid Majorana losses.
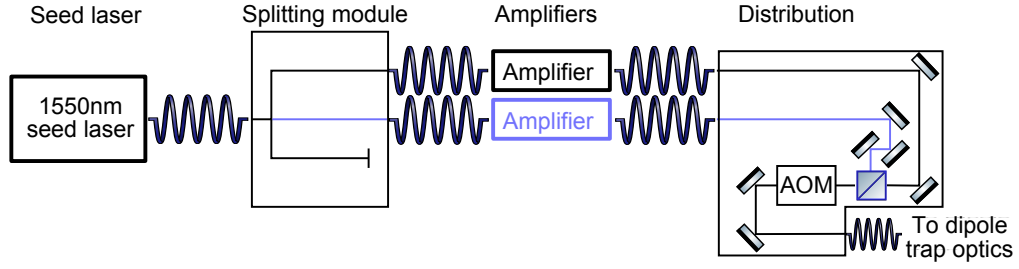
Figure 3.6: Schematic of the dipole trap set-up. The 5 W set-up is shown in black, and the improvements are shown in blue. The schematic does not show all the optical elements, such as those used for beam sizing.

A comparative characterisation profile of the 10 W dipole trap was done, and is shown in Figure 3.7. Other than the gain in power, it can be noted that the main difference is the linearity of the calibration on the new dipole trap. This can be explained by the fact that, in the improved set-up, the AOM remains on when not in use, with the light being deflected away from the experiment by a change in the radio frequency applied to the AOM.
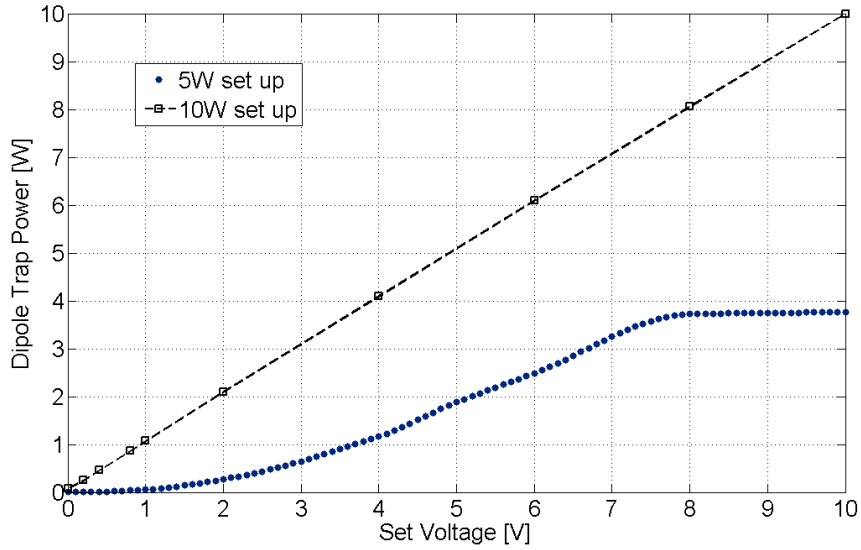
Figure 3.7: Graph showing the power of the 5 W (filled circles) and 10 W (dashed line) dipole traps as a function of the AOM voltage setting.

fluorescence imaging

camera

fluorescence
from the atom

absorption
imaging

camera

resonant
light
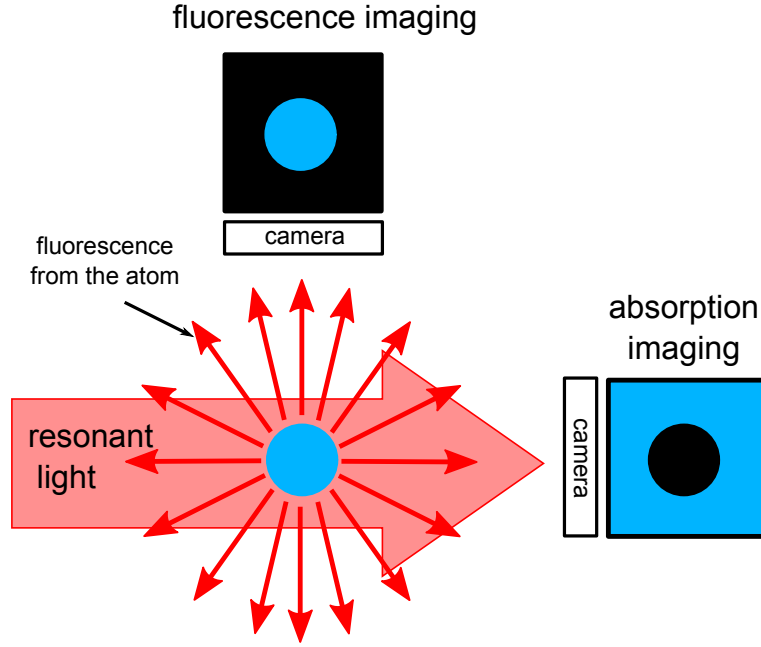
Figure 3.8: Schematic representation of the different imaging methods: in fluorescence imaging, the light emitted from the atom cloud is recorded, whereas in absorption imaging it is the shadow of the cloud which is recorded.

3.4   Imaging

3.4.1   Motivation

In order to take quantitative measurements, destructive imaging of the atom cloud is done. As shown in Figure 3.8, there are two main methods of imaging: absorption and fluorescence. As can be seen from the schematic representation in Figure 3.8, fluorescence from the atoms is scattered in all directions, and the camera can only capture information which falls in its solid angle. In the case of absorption imaging, the detection light and the camera are head-on, and the shadow of the cloud is imaged, as it is on axis imaging, more information about the cloud is retained. Because of this, Absorption imaging is predominantly used this system. In order to increase the information that can be extracted, the time of flight (TOF) technique [36] is used. In this technique, the atoms are left to expand for a given but variable time, the TOF time, before they are imaged. The atoms will fall under gravity, changing the position of the centre of mass, but the atomic cloud will also expand thermally or, in the case of a BEC, according to the appropriate scaling relation (see Section 6.2.1). By varying the time of flight, the extent of the thermal expansion can be assessed, hence yielding information about the temperature of the cloud, for example.

3.4.2 Absorption imaging theory

The intensity, I, of the original intensity, I_0, making it past its absorption by a gas is described by Beer's law which states that [77]

$$I = I_0 e^{-OD} = I_0 e^{-n\sigma}, \tag{3.1}$$

where n is the column density of the atoms and σ is the absorption cross section. Rearranging and substituting for σ yields [39, 77]

$$-\ln \frac{I}{I_0} = OD = n \frac{\sigma_0}{1 + 4\left(\frac{\Delta}{\Gamma}\right)^2 + \frac{I_0}{I_{sat}}}, \tag{3.2}$$

where Δ is the detuning, Γ is the linewidth of the atomic transition[1], I_{sat} is the saturation parameter and σ_0 is the resonance cross section. The resonance cross section is given by [39, 77]

$$\sigma_0 = \frac{\hbar \omega \Gamma}{2 I_{sat}} = \frac{3 \lambda^2}{2\pi}, \tag{3.3}$$

where ω is the frequency of the detection light, and the saturation intensity is given by [39]

$$I_{sat} = \frac{\pi h c}{3 \lambda^3 \tau}, \tag{3.4}$$

where h is Planck's constant, c is the speed of light in vacuo, λ is the wavelength of the light, and $\tau = 1/\Gamma$ is the lifetime of the excited state. Substituting in equation 3.2 and rearranging for n yields

$$n = -\ln\left(\frac{I}{I_0}\right) \frac{\omega^2}{6\pi c^2} \left(1 + 4\left(\frac{\Delta}{\Gamma}\right)^2 + \frac{I_0}{I_{sat}}\right). \tag{3.5}$$

In order to convert the column density into an atom number, the column density is summed over all pixels. The size of a CCD camera pixel, A has to be taken into account, as well as the magnification, M. The polarisation of the light will also affect the response of the atoms, so a parameter Q is also introduced, and is equal to 1 in the case of circularly polarised light. Doing so gives the number of atoms [66, 78]

$$N = -\ln \frac{N_A}{N_B} \frac{M A Q \omega^2}{6\pi c^2} \left(1 + 4\left(\frac{\Delta}{\Gamma}\right)^2 + \frac{I_0}{I_{sat}}\right), \tag{3.6}$$

where N_A is the intensity recorded by the camera in the atoms image, and N_B is the intensity in the background image. The intensity of the illumination is linked to the saturation intensity of the atoms, and care is taken not to exceed $\sim 10\%$ of the saturation parameter because otherwise some of the atoms might

---

[1] $2\pi \cdot 6.06$MHz for ^{87}Rb [67]

28
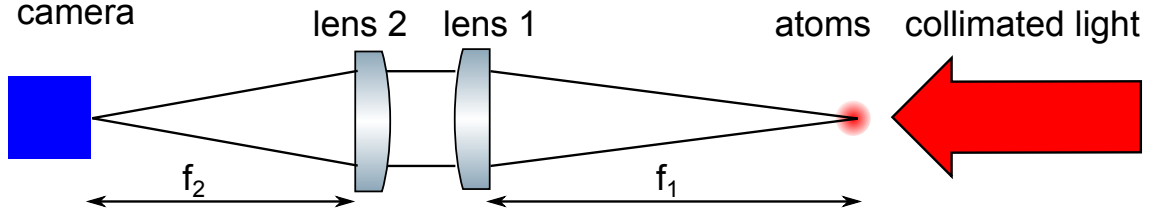
Figure 3.9: Schematic representation of the horizontal detection system in the experimental set-up.

start becoming transparent, leading to erroneous information in the imaging. Because the no-atoms image is 'subtracted' from the atoms image, it is important that both images have the same intensity. Resonant light is used for imaging.

3.4.3 Imaging optics

Absorption imaging is the primary imaging method used in the experiment. A $1''$ collimated beam of resonant light probes the atoms, with magnification or demagnification optics placed head-on with the detection beam, as illustrated in Figure 3.9. The demagnification optics consist of two achromatic lenses, with the atoms at the focus of the first lens, and the CCD camera at the focus of the second lens. Because the atom cloud is treated as a point source, it is not necessary to have a strict 4-f configuration as the information-carrying light is collimated between the two lenses, as shown in Figure 3.9. The camera used in our imaging system is a pixelfly qe camera[1], which has pixels of dimension 6.45 μm $\times$ 6.45 μm.

3.4.4 Magnification

In order to correctly assess the number of atoms in a given cloud, the magnification of the system needs to be known. Magnification, by definition, is given by the ratio of the two focal lengths of the lenses. In an optics system where the lenses have focal lengths of 300 mm and 200 mm respectively, a magnification of 2/3 is expected. In order to verify this experimentally, a ruler was focused on, imaged, and the magnification extracted by comparing the physical separation between the markings and the number of pixels between each marking. The magnification is given by

$$\frac{1}{m} = \frac{\text{object size}}{\text{camera pixel size} \times \text{object pixels}}, \tag{3.7}$$

---

[1]Chip size: 1024×1392 pixels, from PCO.

where m is the magnification, object size is the real size of the object (here, the spacing between gratings, i.e. $1/20'' = 1.27$ mm), camera pixel size is the physical size of a pixel (6.45μm for the CCD in the pixelfly qe), and object pixels is the number of pixels the object takes (here: 165.4 camera pixels, obtained by measuring the distance over multiple gratings and dividing by the appropriate number). The magnification is found to be 0.83. The reason for the discrepancy between the measured magnification and the expected magnification is not known. In the case of a 300:100 lens system, the magnification was found to be 0.37, also different from the expected value. Measured values are used when processing data.

3.4.5 Post-processing of images

Each pixel counts towards the atom number calculation. Consequently, in order to obtain a realistic atom number, parts of the images are cut, especially if they contain distortions. For images in the glass cell with glass cell boundaries visible, these boundaries are cut away. Similarly, in the case of images in the MOT (with or without moving coils), coils are cut away.

To take into account any offset in the background, masks are used. Masks define an area of interest where no atoms are present. This region should be zero, as it should be the same in both atoms and no-atoms images. Due to fluctuations in beam intensity, this may not be the case. The optical density (OD) of this user-defined region is averaged, and the average value is then subtracted from the OD in the entire image. It is this cut and offset-corrected optical density that is used to estimate the atom number.

Depending on the situation, two types of masks are used: one defines a (small) region and uses the mean value within that region as the background OD value. The other type of mask defines an exclusion zone, where no atoms should be present, and uses the mean value of the exclusion zone as the background OD. The images of a 5 ms TOF time MOT cloud and corresponding line cut-through of the OD at different stages in the post-processing are shown in Figure 3.10. The corresponding atom numbers at each stage are shown in Table 3.1. Both types of masks yield atom numbers that are within errors of each other, and that without corrections, the slightly negative background dominates the atom number calculation, rendering it negative.

Raw image	Cut Image	Small Mask	Exclusion Mask
$-6.44\ 10^8 \pm 2.58\ 10^7$	$-1.63\ 10^8 \pm 5.01\ 10^6$	$2.17\ 10^8 \pm 1.10\ 10^7$	$2.34\ 10^8 \pm 1.24\ 10^7$

Table 3.1: Atom number at different post processing stages. The atom number stated corresponds to the images shown in Figure 3.10, and the error is the standard deviation obtained from processing 5 images in each set.

For images taken in the glass cell, a phenomenon of fringes, due to interference within the glass cell, has
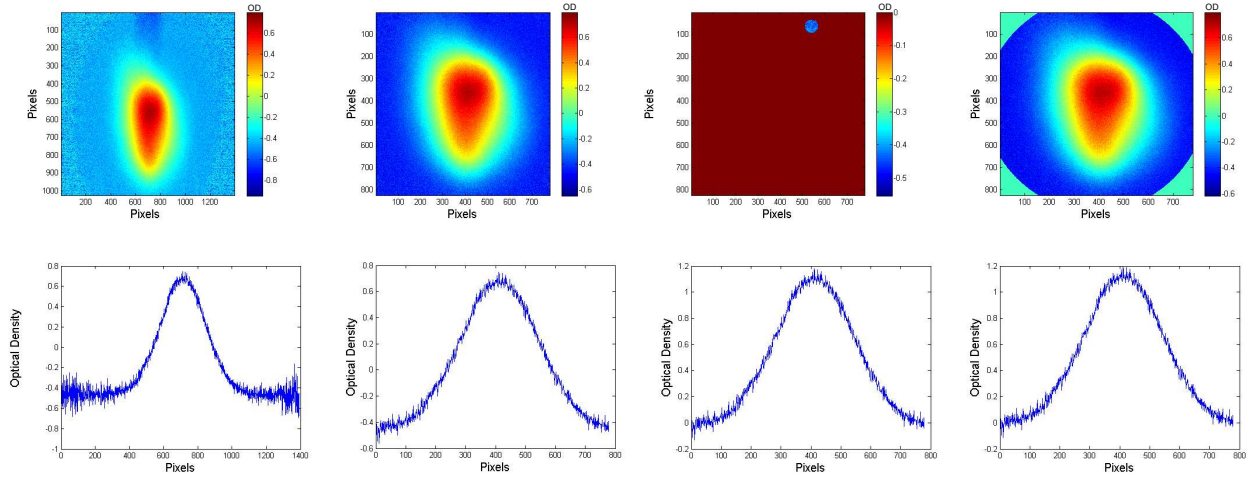
Figure 3.10: Stages of image post-processing: Top: image of the atoms with the mask used; bottom linecut of the atom optical density at each stage. From left to right: original image; cutting the image to minimise background; image of the small mask and linecut of the atom optical density with that mask applied; and exclusion area mask, with linecut of the atom optical density with that mask applied. In the case of the small mask technique, the average optical density of the small blue area outside the mask (shown in red) is used to establish the background optical density. For the exclusion mask technique, the mean value of the optical density behind the light blue area is taken as the background optical density. From the linecuts, it can be seen that both mask techniques correct for the negative background. The corresponding atom numbers are given in Table 3.1.

been observed. This interference renders summing of pixels to estimate atom number unreliable, as regions of the atomic cloud will artificially appear denser or less dense than they truly are depending on the position of a peak or trough in the interference pattern.

In order to eliminate this potential source of error, a defringing algorithm is used [78] [79]. The algorithm remembers a user-defined bank of no-atoms images. As each atoms image is processed, a linear combination is made to the best matching no-atoms image from the bank. This process is done on the glass cell images before any cutting or other post-processing occurs. An image, both non-processed and defringe-processed is shown in Figure 3.11. A limitation of this algorithm is that the atom cloud has to be smaller than the size of the detection beam, otherwise the atoms image and no-atoms image look too similar for a reliable linear reconstruction to be achieved.

3.5   Computer control

In order to run even a simple cold atoms experiment, timings between various experimental elements, such as shutters, coils, or AOMs need to be synchronised. A schematic representation of a typical experimental
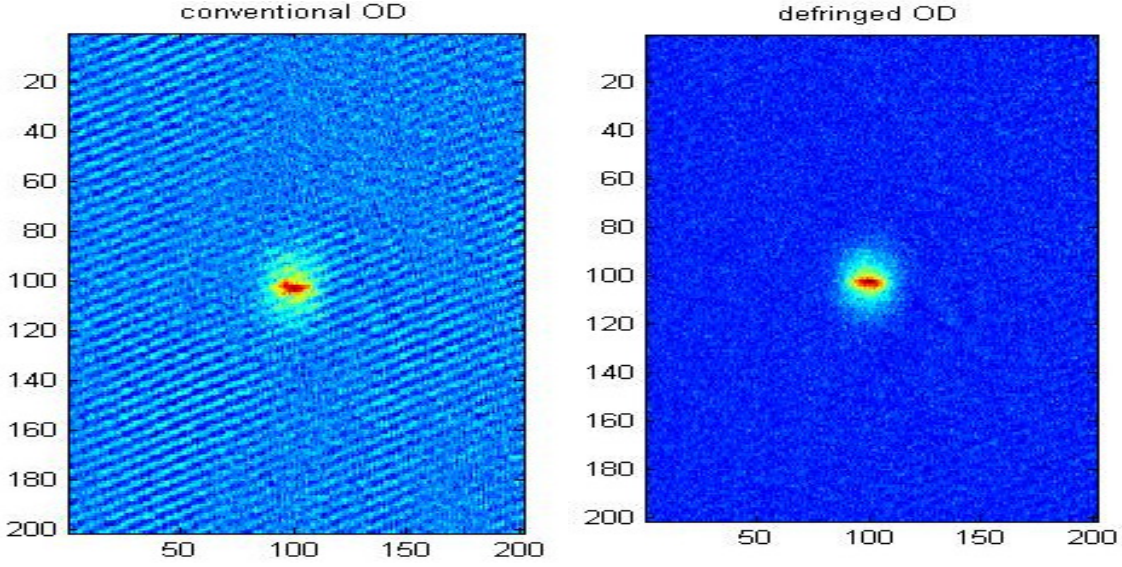
Figure 3.11: The effect of the defringing algorithm: on the left, the image before the algorithm is applied, and on the right, the image after the algorithm is applied. It can be noted that the lines in the background are significantly decreased, and the small atoms cloud is sharper.

sequence is shown in Figure 3.12, along with an indication of the duration of each phase of the sequence.

3.5.1   LabVIEW program

Full details of the computer control can be found in Reference [71], and only a brief overview will be given here. The computer control is primarily built using the National Instruments' LabVIEW PXI infrastructure, allowing both digital and analogue controls. Field-programmable gate arrays (FPGAs) are used as they allow for fast processing of the commands. The system has a 25 ns clock cycle. In addition to the LabVIEW
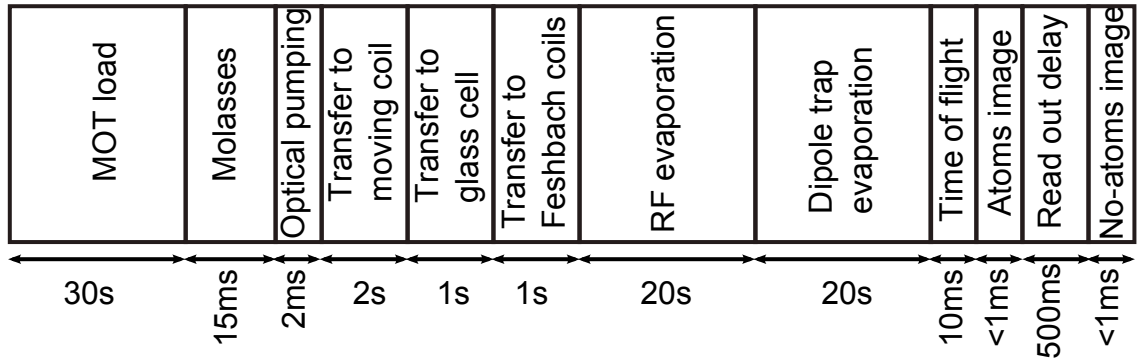
Figure 3.12: Schematic diagram showing a typical experimental sequence, with order of magnitude numbers indicating the duration of each phase. Time runs from left to right.

Element	Computer controlled	Manually set
2D light	Shutter on/off	Cooling and repumping AOMs, power of the beam
Pushing beam	Shutter on/off, AOM detuning, power	
3D cooling light	VCO detuning, power, AOM detuning, shutter on/off	
3D repumping light	Power, shutter on/off	AOM
MOT coils	IGBT on/off, current	
Optical pumping MOT detection beam	AOM detuning, power, shutter on/off	
Moving coils	IGBT on/off, current, position	
Feshbach coils	IGBT on/off, current	
RF evaporation	Frequencies, amplitude, sweep time	Physical position
Dipole trap	On/off, power	Number of amplifiers on
GC detection light	VCO, AOM, shutter on/off, power	
Camera	Triggering	

Table 3.2: Experimental elements and how they are controlled.

system, the computer control also interacts with IGBTs (Insulated Gate Bipolar Transistors), allowing fast switching of the coils, and a DDS (direct digital synthesiser) box, allowing control of the RF evaporation. A list of the experimental parameters and whether they are computer controlled or manually set is given in Table 3.2.

3.5.2 The camera program

The camera is computer controlled and triggered in the LabVIEW sequence [80]. For every measurement, the camera takes two images: the atoms image and the background (no-atoms) image. The time delay between these two images has to be greater than the readout time of the camera, which is of 200 ms [80]. For reliable

post-processing of the images, the light intensity needs to be the same in both images. Because of the heating time of the AOM which controls the imaging light[1], an additional 500 ms are added after the camera readout time to allow the AOM to be warmed again for the no-atoms image.

3.6   Conclusion

This chapter has introduced the BEC apparatus used in this experiment. The vacuum system has been described, and the quality of the vacuum characterised. The laser system and MOT optics have been described, as well as the magnetic coils and dipole trap. The imaging method of absorption imaging has been introduced, along with the corresponding horizontal optical set-up. The chapter has also described the working principle of the computer control and the camera program.

---

[1]The intensity of the light depends partly on the temperature of the AOM.

CHAPTER 4

COILS

Coils are an integral part of any cold atoms experiment, with their principal role being to trap and transport neutral atoms. After introducing the basic properties of magnetic coils, this chapter will focus on the redesign of two sets of coils. The first set of coils to be addressed are the moving coils, where new technology will be adapted. Simulations of the magnetic gradient for this new design will be presented, as well as the final design and fabrication of this set of coils. The Feshbach coils redesign focuses primarily on the failing electrical connectors, and attention is given to material choices. The fabrication process of the Feshbach coils is also described. Both sets of coils are also characterised.

4.1   Basics of coils

The strength of the field for one coil is given by the Biot–Savart law

$$\vec{B} = \int \frac{\mu_0}{4\pi} \frac{I d\vec{\ell} \times \hat{a}}{a^2}, \tag{4.1}$$

where B is the magnetic field, μ_0 is the permeability of free space, I is the current going through the coil, a is the radius of the coil, as illustrated in Figure 4.1. In the case of a circular geometry, the magnetic field along the central axis is [81]:

$$B = \frac{\mu_0 I a^2}{2(a^2 + x^2)^{3/2}}, \tag{4.2}$$

where x the distance along the x-axis from the coil. Figure 4.1 illustrates some of the terms for clarity. In the case of two coils in an anti-Helmholtz configuration, Equation 4.2 becomes [82]

$$B = \frac{\mu_0 I a^2}{(a^2 + x^2)^{3/2}}, \tag{4.3}$$
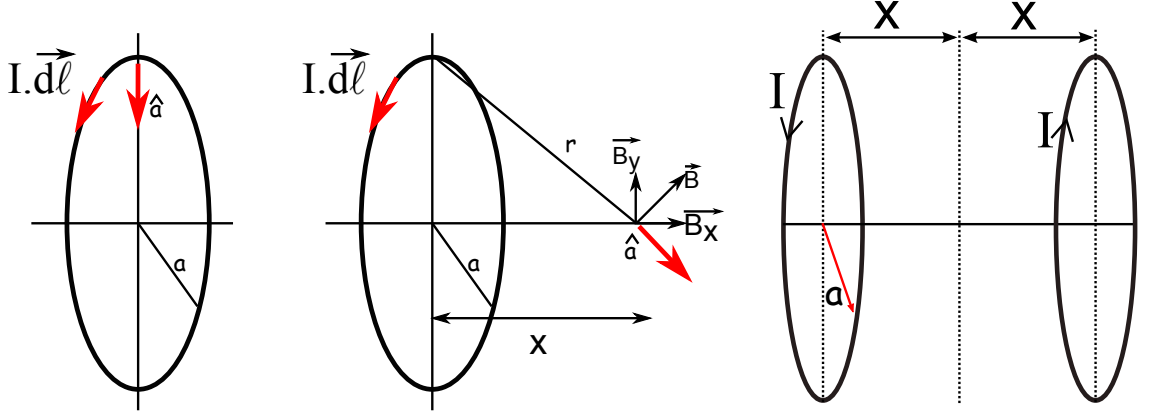
Figure 4.1: Schematic representation and definition of the coil variables. From left to right, Biot–Savart law (Equation 4.1); Biot–Savart law for a circular geometry, giving the field along the x-axis (Equation 4.2); and coils in the anti-Helmholtz configuration (Equation 4.3).

where the factor of two accounts for the presence of both coils, and x is the half-separation of the coils.

Differentiating Equation 4.3 with respect to x, the direction where the atoms will be trapped, yields the gradient of the magnetic field:

$$\frac{\partial B}{\partial x} = b = -3\frac{\mu_0 I a^2}{2}\frac{2x}{(a^2 + x^2)^{5/2}} \tag{4.4}$$

4.2 New design moving coils

This section will justify the need for a redesign, using a different type of coil technology. Simulations for power-optimised coils are presented before the final design, fabrication and testing of the coils are described and discussed.

4.2.1 The need for a redesign

The previous moving coils [66] are made to be as compact as possible, using kapton insulated copper tape in direct contact with the coolant inside a casing composed of two parts which are glued together. The design featured a slit to prevent eddy currents [66], which weakened the structural strength of the casing leading to bending. This bending led to a weakening of the main glued seal. In addition to leaking from the main seal, parts of the material used to lift the coil inside the casing, thus creating a flow channel along the face of the coil, have become detached and have blocked the cooling system. Images of the decommissioned coil are shown in Appendix A.
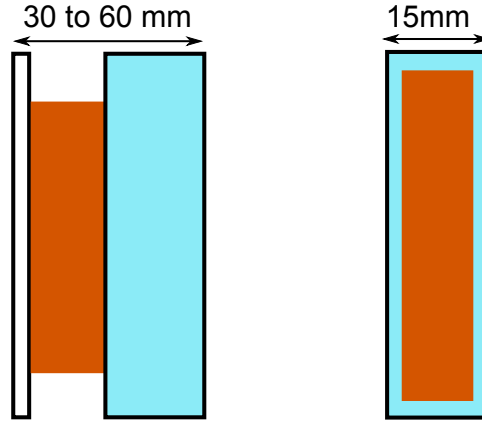
Figure 4.2: Comparison of two different coil technologies. On the left hand side, the indirect cooling coil, where the copper (orange) is in indirect contact with the coolant (blue). On the right hand side, the conventional coil technology developed for the experiment, where the copper (orange) is in direct contact with the coolant (blue) and both are enclosed in a casing.

4.2.2 Adapting technologies

As the outermost coils on the experimental system, the moving coils have the flexibility to be broader than any other coils, which means that a less spatially constrained technology, such as that developed by the Clock group at the University of Birmingham [83], can be adapted. The two types of coil technology are schematically illustrated in Figure 4.2. Unlike the prototype technology developed for this experiment which sees the copper being cooled by direct contact with the coolant, the technology developed by the Clock group relies on indirect cooling of the coils. The coolant is contained in a separate cavity and is in thermal contact with the coil via the thin, thermally conducting, wall of the cavity. The difference in the cooling method has ramifications for the fabrication of the coil. In the case of the prototype technology, the casing is closed once the copper coil is placed inside, and therefore a sealing method which does not damage the internal components (such as a low temperature curing glue) must be used. In the case of the indirect cooling coil, the casing is fully manufactured before the copper coil is wound in situ. More aggressive methods of sealing the coolant containing cavity, such as welding, can be used, thereby eliminating the source of leaking. By using the Clock group technology, the need for glue, which has been shown to weaken in the presence of the coolant, is removed.

4.2.3 Design considerations

Whilst the general structure of the new moving coil is known from the onset, the detailed design must take into consideration the desired performance requirements. The role of the moving coils is to transport the

atoms from the 3D MOT chamber to the glass cell, via the 16 mm diameter differential pumping stage. The size of the differential pumping stage sets an upper limit on the size of atom cloud which can pass through it. At a given temperature, the size of the cloud depends on the magnetic gradient. The design magnetic gradient for the new coils is of 160 G/cm[1] at 100 A, leaving ample head room to use the coils at lower currents and still pass the atoms through the stage, see Equation B.6.

From Equation 4.2, the half-separation and the radius of the coils are key parameters which affect the coil performance. The half separation is given by physical constraints of the experiment, illustrated in Figure 4.3. The distance between the centre of the glass cell and the outside of the Feshbach coils is 42 mm. From previous experience, the minimal thickness of the outer section of brass should be no less than 4 mm otherwise manufacturing issues can occur. Copper tape is used as its geometry maximises the cross-sectional area of the copper when winding [66]. The copper tape used is 14 mm wide, 0.25 mm thick with 0.023 mm insulating kapton wrapped around the copper[2]. Adding on a 2 mm safety margin yields a half separation of 55 mm.
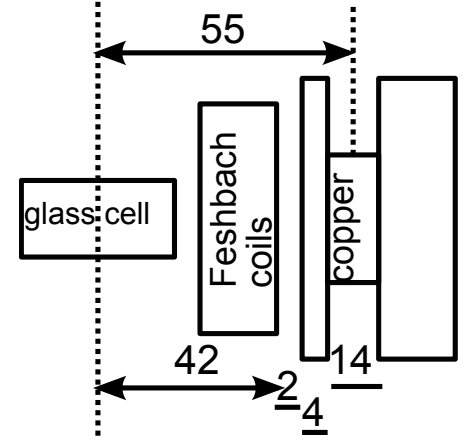
Figure 4.3: Schematic illustration of the half-separation of the moving coils. All distances are in mm.

4.2.4   Simulations

The design of the coils can be optimised either for minimum power or for minimum current. Power optimisation is chosen because it leads to less heating of the coil. In this section, two approaches to simulating the optimised power design will be presented. Both approaches rely on the Biot–Savart law, but the first, more simplistic method assumes a single winding, whereas the second approach takes into account the effect of multiple windings.

Single winding approach

This approach approximates the coil as being a single winding. The power, P, is given by

---

[1]Equivalently 1.6 T/m.
[2]HP04 tape from High Precision Foils Ltd.

$$P = IV = RI^2 = \frac{\rho L}{\sigma} I^2 = \frac{2\pi \rho a}{wh} I^2, \tag{4.5}$$

where I is the current passing through the material, V is the applied voltage, R is the resistance, ρ is the resistivity of the material of the coil (here: copper[1]), L is the length of the copper, σ is the cross-sectional area of the copper, w is the width of the copper, and h is the height of the copper. Rearranging Equation 4.4 for current, and substituting into Equation 4.5 yields

$$P = \frac{2\pi \rho}{wh} \left(\frac{1}{3\mu_0 x} \right)^2 (b)^2 \frac{(a^2 + x^2)^5}{a^4} a. \tag{4.6}$$

Differentiating Equation 4.6 with respect to the radius, a, and minimising yields:

$$\frac{\partial P}{\partial a} = 0 \leftrightarrow 0 = \frac{10a^2(a^2 + x^2)^4 - 3(a^2 + x^2)^5}{a^4}. \tag{4.7}$$

Solving Equation 4.7 for a yields the power optimised ratio of the radius, a, to the half-separation, x:

$$\frac{a}{x} = \sqrt{\frac{3}{7}}. \tag{4.8}$$

Substituting the value of $x = 55$ mm into Equation 4.8 yields a coil radius of 36 mm. The calculations above assume a single loop of copper with all the current going through it. In a system where there are many turns, this radius would be approximated with the midway point (i.e. as many windings above as below). In a more realistic scenario, there will be multiple windings, with each winding having a different radius, and hence a slightly different contribution to the magnetic field.

Multiple windings approach

The total gradient, b_T, for N turns is given by the sum of the gradient, b_i, due to each winding a_i, per Equation 4.4

$$b_T = \sum_{i=1}^{N} b_i = \sum_{i=1}^{N} \frac{3\mu_0 I a_i^2 x}{(a_i^2 + x^2)^{5/2}}. \tag{4.9}$$

Similar to the single winding approach, rearranging Equation 4.9 for current yields

$$I = \frac{b_T}{\sum_{i=1}^{N} \frac{3\mu_0 a_i^2 x}{(a_i^2 + x^2)^{5/2}}}. \tag{4.10}$$

---

[1] $\rho = 1.7 \cdot 10^{-8} \Omega$.m [84]

Introducing the α parameter, defined as $\alpha = a/2x$, i.e. the ratio of the radius to the full separation, and substituting into Equation 4.10 gives

$$I = \frac{b_T}{\sum_{i=1}^{N} \frac{12\mu_0\alpha^2}{x^2(4\alpha^2+1)^{5/2}}}.$$
(4.11)

The relationship between the radius of one turn and the next is given by

$$a_2 = a_1 + T,$$
(4.12)

where T is the thickness of the copper strip (and any adhesive).

As with the first case, the design will be optimised for power. As stated in Equation 4.5, power depends linearly on the resistance R of the wire, and is given by

$$P = \frac{\rho}{\sigma} L I^2,$$
(4.13)

where L is the total length of the copper, ρ is the resistivity of the copper, and σ is the cross sectional area of the copper. Substituting in for the total length of the copper, with n the turn number, and N the total number of turns, gives

$$P = \frac{\rho}{\sigma} \left(2\pi \left(Na_{IN} + \sum_{n=1}^{N} (n-1)T \right) \right) I^2,$$
(4.14)

where a_{IN} is the innermost radius. Re-expressing Equation 4.14 in terms of the α_{IN} parameter ($\alpha_{IN} = a_{IN}/2x$), yields:

$$P = \frac{\rho}{\sigma} \left(2x2\pi \left(N\alpha_{IN} + \sum_{n=1}^{N} (n-1)\frac{T}{2x} \right) \right) I^2.$$
(4.15)

Substituting Equation 4.11, re-expressed in terms of α_{IN}, for I into Equation 4.15 and rearranging yields

$$P = \frac{2\pi\rho 2x b_T^2}{\sigma} \frac{N\alpha_{IN} + \sum_{n=1}^{N}(n-1)\frac{T}{2x}}{\left[\sum_{n=1}^{N} \frac{12\mu_0\left(\alpha_{IN}+(n-1)\frac{T}{2x}\right)^2}{\left[4\left(\alpha_{IN}+\frac{(n-1)T}{2x}\right)^2+1\right]^{5/2} x^2} \right]^2}$$
(4.16)

Simulating the above equation as a function of α_{in} with values of N=100, and half separation of 55 mm and an increase in thickness (T) of 0.323 mm[1] yields the graph shown in Figure 4.4.

---

[1] Copper thickness of 0.25 mm, kapton thickness of 0.023 mm, and an assumed glue thickness of 0.05 mm.
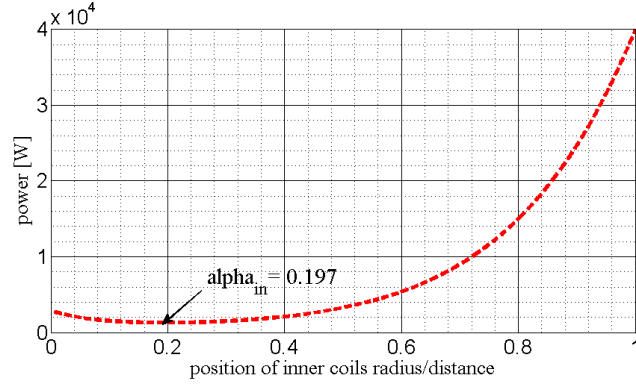
Figure 4.4: Simulated power consumption for the new moving coils as a function of inner-radius to separation ratio, α_{IN}. The ratio at which the power consumption is minimised is highlighted.

As can be seen from Figure 4.4, the optimal α_{IN} is 0.197, which gives a power optimised inner radius of 21.67 mm, for a half separation of $x = 55$ mm.

Comparison of the two approaches

In order to compare the radii given by the two approaches, a thickness equivalent to half the number of turns[1]. Doing so gives a 'middle radius' of 37.82 mm, compared to the 36 mm given by the simplistic approach. The results show that both approaches do give similar results, but that the presence of windings does affect the gradient slightly.

4.2.5   Final design and fabrication of the moving coils

Having established the simulation constraints of the coils, a final design was made. The housing has an inner diameter, and therefore optical access, of 35 mm, with a 4 mm thick central arch for the coils to be wound around, yielding an inner diameter of 43 mm. The cooling channel is designed to encourage turbulent flow of the coolant, as turbulent flow is better for heat dissipation than laminar flow [66]. The presence of a slit avoids eddy currents, but should not weaken the structure of the coil as the thickness of the body material is greater than in the previous design [66].

In order to avoid damaging the copper on the slit whilst winding, the coil is made in three parts held together by a system of screws: the cooling body, the central arch, and the lid, as shown in Figure 4.5. The winding of the coils is also shown in Figure 4.5. A coil with N=98 turns was made. In order to increase the thermal contact between the copper and the coolant cavity, thermal pads were added between the copper and the

---

[1]50×0.323 mm

41
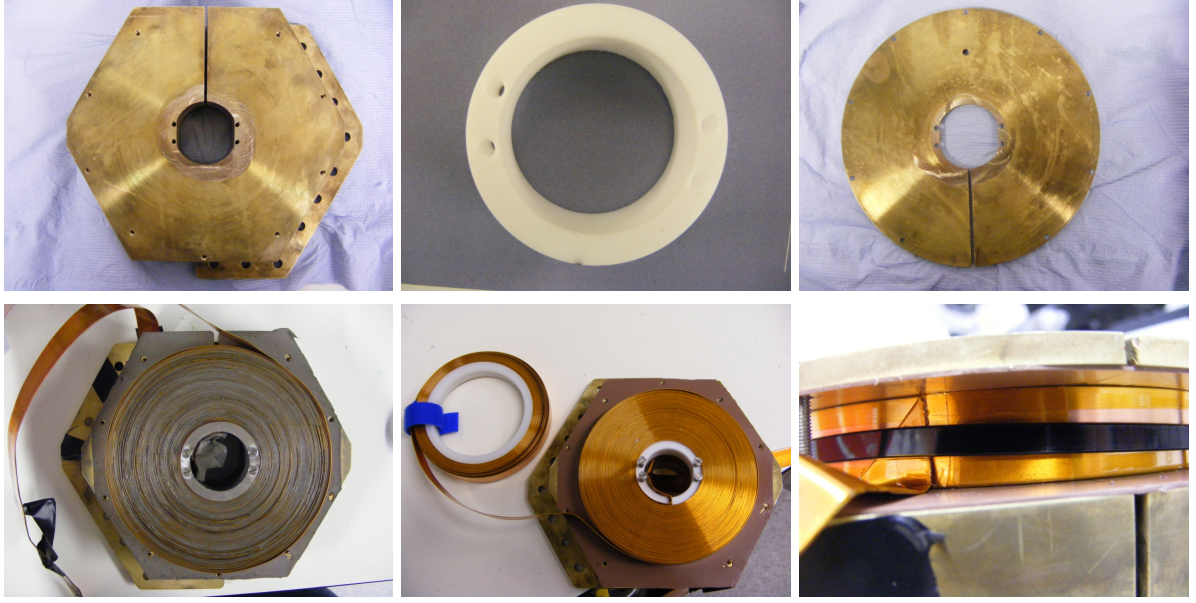
Figure 4.5: New-design moving coils and winding of the coils. From left to right, top to bottom: main body containing the coolant channel; 4 mm thick central arch; lid of the body; winding of the coil with heat conducting paste on the copper; winding of the coil without heat conducting paste; and coil securing mechanism. Each coil has N=98 turns.

brass[1]. For one coil, heat conducting paste[2] was spread on the copper. This resulted in an uneven coil, so additional 2 mm thick nylon sheets were inserted between the lid and the coil to increase thermal contact. Thermal paste was not used on the second coil, which resulted in an evenly wound coil.

4.2.6 Testing and in situ characterisation

In order to test the cooling of the coils, different currents were passed through the water cooled coils until the temperature of the coil had stabilised. The temperatures of the brass casing and the copper were monitored with thermocouples. The thermocouple measuring the copper temperature was placed inside the slit, as per Figure 4.6 in direct contact with the copper. The thermocouple measuring the brass housing temperature was placed on the back of the coil, in contact with the coolant cavity, and found that the water temperature was stable at (14 ± 1) °C.

The results of the copper temperature measurements are shown in Figure 4.7. For currents below 20 A, no significant heating (more than 1 °C) of the coils was recorded, hence the data is not shown for clarity. In the cases of higher currents ($\geq$20 A), the temperature rise occurs in the first five minutes, after which time

---

[1]T Global H482-150-0.5A Gap filler 0.5 mm sheet.
[2]Arctic silver thermal paste.
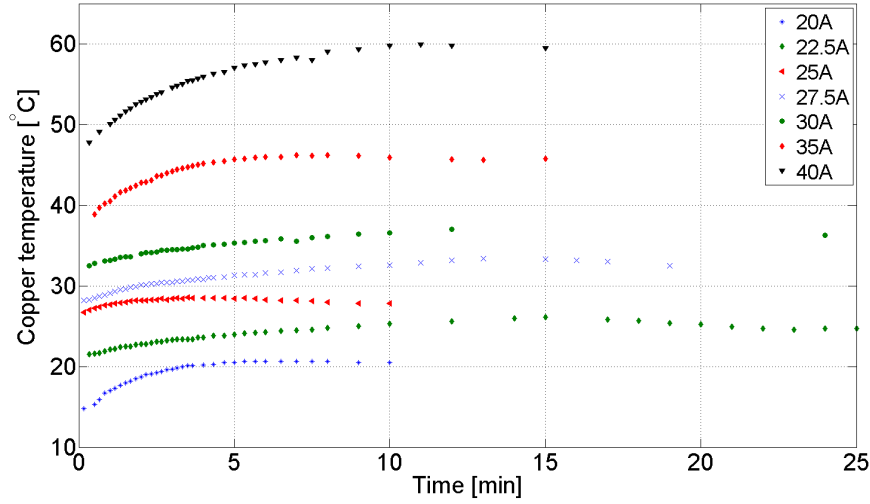
Figure 4.7: Testing of a moving coil: Temperature of the copper recorded as different currents are passed through the coil. A maximum copper temperature of 60 °C is recorded at 40 A.

the temperature of the coil stabilises. The time over which the temperature of the copper rises is significantly longer than the ≈5 seconds that the coils are on for. With an experimental sequence on the order of one minute, the coils will have time to cool between each experimental sequence.

The new-design moving coils were implemented on the experiment after the old moving coils were decommissioned. During the construction of the moving coils, the additional thickness due to the thermal sheet, and in the case of one of the coils, the extra nylon sheets to ensure contact, means that the coils performance will have deviated from the simulated model (Section 4.2.4). Indeed, rather than having the planned half separation distance of 55 mm, the coils required a separation distance of 126 mm (half-separation of 63 mm), in order to clear the experiment suitably. This discrepancy can be partly explained by the originally unaccounted 5 mm of nylon and conducting tape (per coil). Conservative positioning of the coil could account for an additional 2-4 mm in the half-separation.

Figure 4.6: Figure showing the placement of the thermocouple measuring the temperature of the copper coil.

When in place at this new separation, the gradient measured was of 1.4 G/cm/A, lower than the 1.6 G/cm/A of the design. This lower gradient still fully meets the minimum requirements, namely to transport the entire atom cloud through the differential pumping stage. With reference to equation B.6, the coils will need to

43

Property	Old coils	New coils
Number of turns	93	98
full separation [mm]	107.5	126
Inner Diameter (casing) [mm]	82	35
Gradient [G/cm/A]	1.5	1.4

Table 4.1: Comparison of the properties of the two moving coils.

run at $\approx$70 A, rather than $\approx$60 A with the design gradient.

Table 4.1 compares key properties of the old and new moving coils, from which the main noticeable difference is the optical access provided by the coil. The new coils provide a significantly reduced optical access: the access is sufficient to pass a $1''$ beam through it, but not enough to have the dipole trap on with the moving coils still in position at the glass cell. The presence of the smaller optical access reduces the field of view and adds a second to the experimental sequence as the moving coils will have to be moved back to the MOT whilst the atoms are held in the Feshbach coils before the dipole trap can be switched on. The reduced optical access does not affect the 3D MOT or the alignment of the optical pumping beam.

4.3 Feshbach redesign

This section will focus on the redesign of the body of the Feshbach coils. The need for a redesign will be explained, and the redesign choices will be justified. The coil making and body glueing processes will be described. Testing of the coils will also be discussed.

4.3.1 The need for a redesign

The original Feshbach coils were decommissioned after repeated failures at the electrical connectors, leading to coolant leaks. The connectors, shown in Figure 4.8, feature three different materials glued together: copper, PEEK and titanium, which all have different coefficients of thermal expansion. With the sudden switching the coils are subjected to, the glue at the connectors is repeatedly stretched with each cycle, especially since the connectors are immersed in glue and therefore not in full contact with the coolant. The glue is already known to weaken when in contact with the aromatic coolant, leading to leaks.

The orientation of the connectors in the original coil design can also be a contributing factor to the leaking. With the widest parts of the connector on the outside of the casing, once the glue is weakened the internal pressure on the connector will push the connector further out, thereby accelerating the time until the failure.

Figure 4.8: The previous Feshbach connectors. From left to right, outer casing view, inner casing view, and schematic side view. The casing is made of titanium, PEEK is used to insulate the copper connector.

Property	Resintech 111	Supreme 10HTND-3
Cure time	2h @23°C 10min @ 60°C	60-75 min @250°F
Viscosity	5Pa*s	non-flowing paste
Temperature range	−55 to 85 °C	4K to +400°F
Shear Strength (Al to Al)	20MPa	>3600 psi (25MPa)
Tensile Strength	40MPa	>7000psi (51MPa)

Table 4.2: Properties of the RT111 [85, 86] and the Supreme 10HTND-3 [87] adhesives.

4.3.2   Solution and redesign

In the redesign, both the glue at the connectors and their orientation were modified. Material choices for the connectors were reconsidered. Additionally, modifications to the way the coil is held inside the casing were made.

The glue at the connectors has to be electrically insulating, resistant to high (≈ 50 °C) temperatures, and the aromatic coolant yet liquid enough to be delicately spread. The Supreme 10HTND-3 adhesive[1] is found to have suitable properties, especially in the temperature operation range and the tensile and shear strength, given in Table 4.2. For comparison, the table also lists the properties of the RT111[2] adhesive, previously used at the electrical connectors and still used for sealing the body.

Because of the large discrepency between the coefficients of thermal expansion (CTE) of the connector materials, given in Table 4.3, the material choice was reconsidered. The titanium of the casing and the copper of the electrical connector have similar CTEs, but the PEEK is significantly different. The PEEK was therefore replaced by another insulating material, Macor, a machinable glass ceramic. By having a material which has a more similar CTE, the glue should come under less strain as the connectors expand and contract through each cycle.

---

[1]Master Bond Inc.
[2]Resintech Limited.

Material	Coefficient of thermal expansion [μm/m.°C]
Copper	16.4 @ 20-100°C [84]
Titanium	8.9 @ 20-100°C [88]
Macor	12.6 [89]
PEEK-450G	47 [90]

Table 4.3: Table showing the coefficients of thermal expansion (in the range of 0–100 °C) of the different materials present in the Feshbach coil.
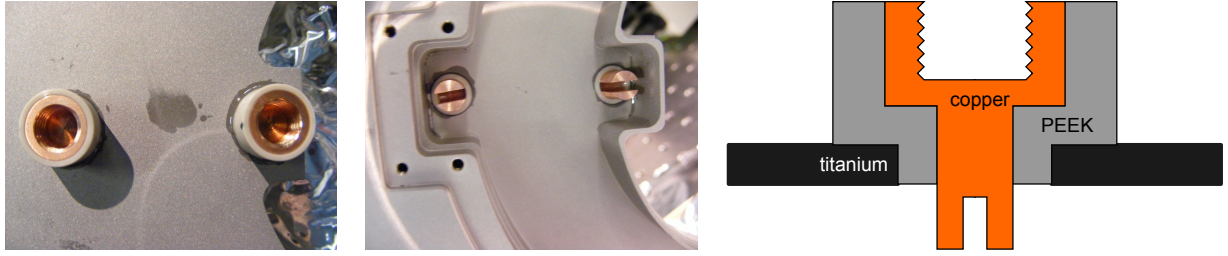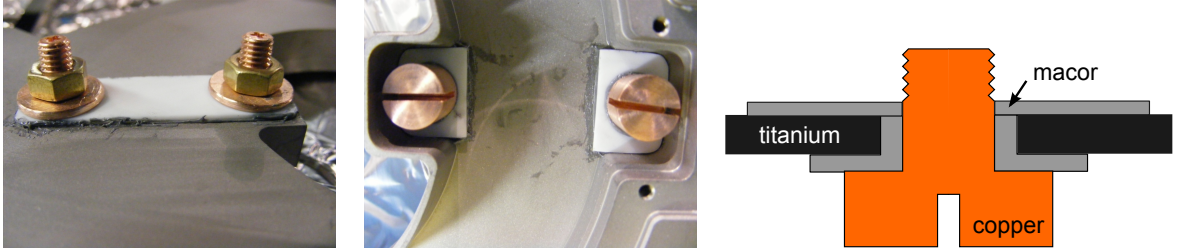

Figure 4.9: The new Feshbach connectors. From left to right: outer casing view, inner casing view, and schematic side view. The casing is made of titanium and Macor is used to insulate the copper connector.

As shown in Figure 4.9, the orientation of the connectors was inverted, with the larger part of the connector inside the casing. With this new orientation, if the glue at the connectors weakens, the coolant flow on the connectors should act as a way of tightening the seal, rather than loosening it as in the previous design. In order to electrically connect the coil whilst remaining electrically isolated from the casing, a Macor plate, placed on the outside of the casing, was added.

In the original design of the coil [66], the coolant flow is preferentially directed onto the face of the coil. In order to create a flow channel on the face of the coil, and to electrically isolate it from the casing, the coil is placed on two 1 mm thick spacers with flow channels in them. To preferentially direct the flow onto the faces, the side channel is filled with glue, with rubber placed at the bottom of the side channel to avoid the glue going onto the bottom face of the coil and prevent cooling. The glue also ensures that the coil does not move within the casing. In this method, the connectors are encased in glue, which limits the dissipation of heat, which contributes to the leaking of the coils at the connectors. In addition, some of the rubber has become loose in other coils, and has blocked part of the coolant circuit.

In order to address these problems, a new method of holding the coil in the casing was devised. The two methods of holding the coil are shown in Figure 4.10. The number of spacers was increased from two to four on each face of the coil, and the spacers are designed with arms, which ensure that the coil cannot move in the casing. The spacer placed between the two coolant entry or exit points does not feature any flow channels

46
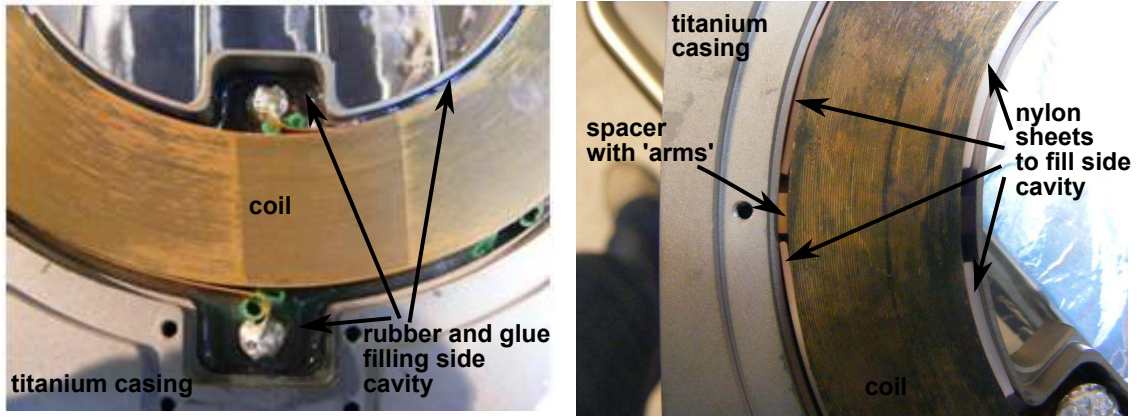
Figure 4.10: Comparison of the two methods used to block the side flow channel. (left) the previous method where rubber and glue are used (see text for details) and (right) the new method, where nylon sheets are inserted into the side channel.

on it, in order to direct the coolant flow around the coil. The spacer material has to be electrically insulating and finely machinable. PEEK was chosen, as Macor is too brittle to be this finely manufactured. Glue is not used to block the side channels, but nylon sheets can be slipped into the side channel. In order to ensure proper holding of the coil, the pieces have to be coil specific and can only be made once the coil has been made.

Modifications to the original coil bodies to accommodate the aforementioned changes were minimal, but still noteworthy. Firstly, the size of the connector cavity was increased slightly to allow for sufficient glueing surface area. Secondly, in order to not interfere with the 100° optical access needed at the glass cell for the dipole trap, and potential extensions such as optical lattices, the inner radius of the casing, and therefore also of the coil, was increased by 1 mm. Side by side renderings of the previous and new Feshbach bodies are shown in Figure 4.11, and a list of different distances is shown in Table 4.4, with an illustration of what the distances correspond to shown in Figure 4.12. The outer dimensions of the casing, as well as its thickness were unmodified.

By modifying the dimensions of the copper coil which can fit inside the casing, the magnetic gradient is modified. The calculated gradient for the new coils is 2.35 G/cm/A compared to 2.34 G/cm/A [66], which is not significantly different.

greater number of spacers

longer spacers, with 'arms' to hold the coil

spacer with no flow channels to direct coolant around coil

different connectors

greater surface area for glue

2mm increase in inner diameter

glue to block side flow channel

nylon sheets to block side flow channel

longer cavity
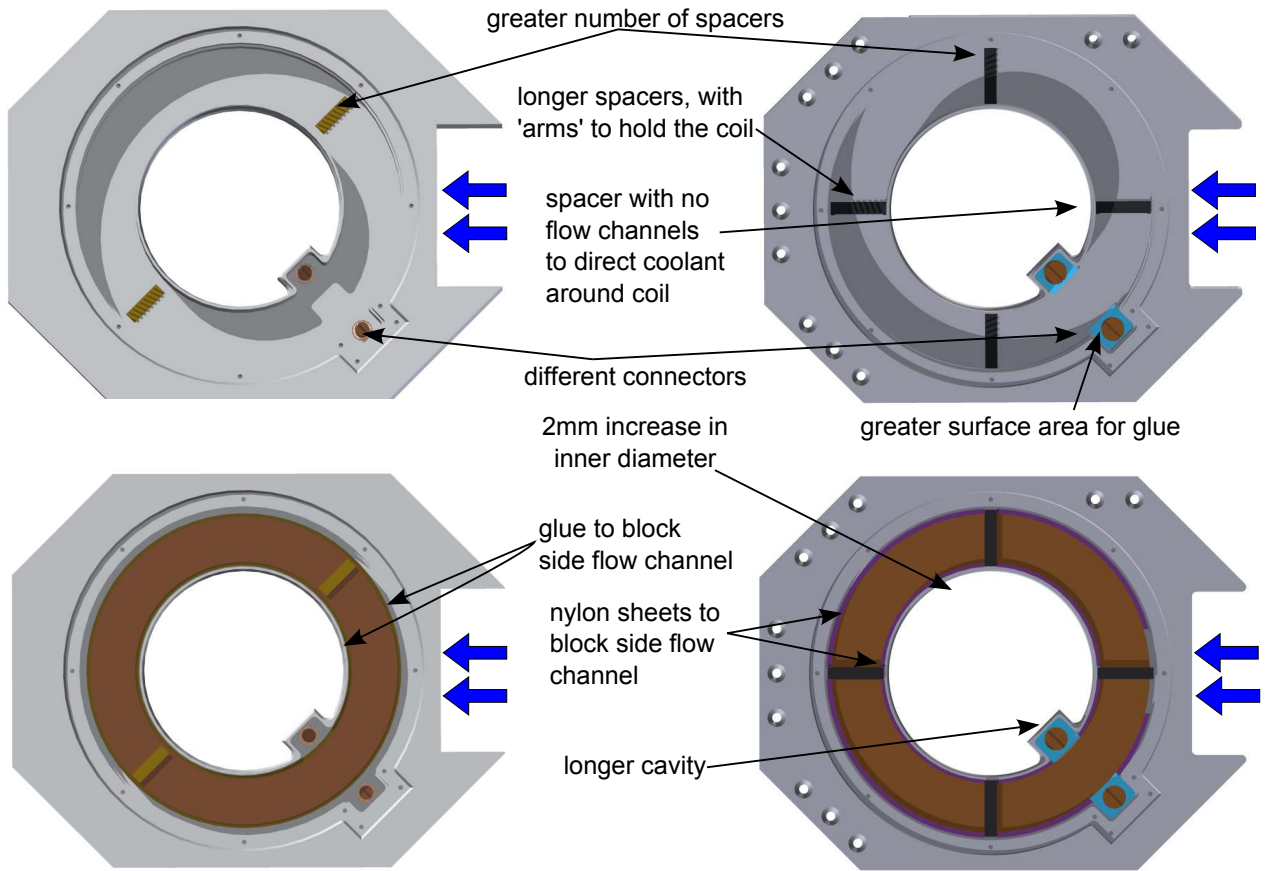
Figure 4.11: Comparison of the previous and new Feshbach coils. The previous coils are shown on the left and the new ones on the right. The blue arrows indicate the coolant entry/exit points. The outer dimensions of the coils remain unchanged between the previous and new design.

Figure 4.12: Dimensions of the Feshbach body referred to in Table 4.4.
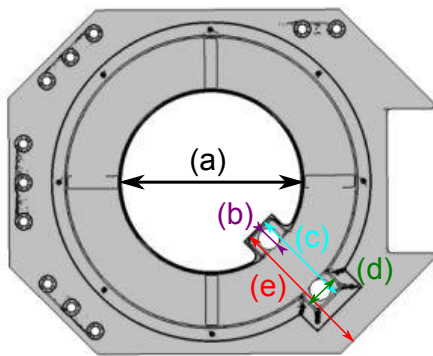
Dimension	Previous Body [mm]	New Body [mm]
(a) Inner radius	43	44
(b) connector hole diameter	9	10
(c) connector cavity length	44.55	47.56
(d) connector cavity width	16	16
(e) outside inner cavity edge to opposite coil edge	72	73

Table 4.4: The dimensions of the different Feshbach cooling bodies. The outer side of the body remains the same for it to fit into the experiment.
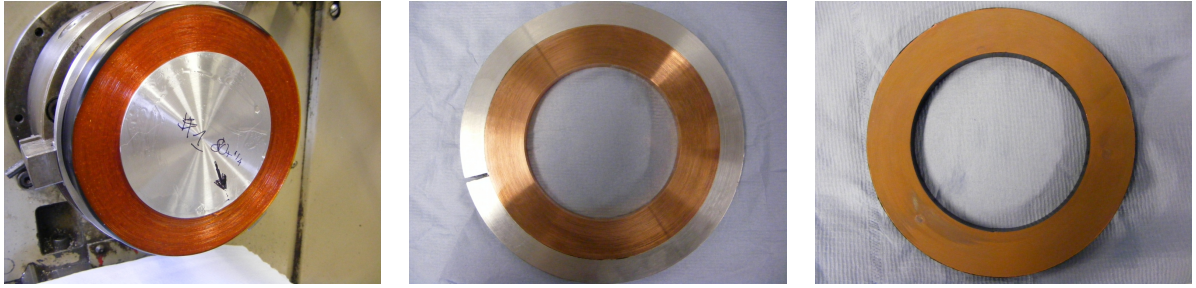
Figure 4.13: The different stages of Feshbach coil making, illustrated on different coils. From left to right: the coil after winding; the coil after milling; and the coil after etching in a ferric chloride hexahydrate solution.

4.3.3 Fabrication of the new Feshbach coils

Making the coils

The process used for winding the Feshbach coils is the same as was previously used [66], and is illustrated in Figure 4.13. Kapton backed copper strip[1] is wound solidly around an aluminium wheel and glued together using RT151[2] adhesive between each turn. The coil is then cured for 2 hours at 60 °C and left overnight. To clear the face from glue and to expose the copper to the coolant and to ensure flatness of the coil for good cooling, the coil is then milled down. Because of the presence of the glue, no machining coolant can be used. The faces of the coil are fully cleared of glue, and the coil is milled down until it is 11 mm thick.

After the milling, the coils are etched in ferric chloride hexahydrate to ensure that any potential small shorts between windings caused by the milling are etched away. The number of turns is measured, using a current clamp. According to this measurement, both coils had 79 turns at this stage of the fabrication process. The coils are referred to as 'left' and 'right' further on.

Making of the spacers

The coil specific spacers are made at this point. Firstly, the number of turns in each coil is reduced in order to allow sufficient ($\approx$2 mm) clearance inside the cavity. The distance between the wall of the cavity and the coil is then measured for each coil, and the spacers are made accordingly.

As shown in Table 4.5, the two coils have different dimensions, despite both having 72 turns. This can be readily explained small differences in tension in the strip or in glue thickness whilst winding.

---

[1]From Alpha-Core, 0.500″ by 0.010″ copper backed with 0.625″ by 0.001″ kapton.
[2]Resintech Limited.

Coil	Inner Diameter [mm]	Outer Diameter [mm]	thickness [mm]
Right	95	139.4	11
Left	95	138.7	11

Table 4.5: Dimensions of the Feshbach coils. Both coils have n=72 turns.

Glueing of the Feshbach bodies

The steps of the glueing are shown in Figure 4.14.

As shown in Table 4.1, the Supreme 10HTND-3 glue cures at high temperature, consequently only pieces that can resist that temperature can therefore be present in casing at that time. Taking this into consideration, only the connectors can be glued using this glue. The inner connectors are positioned, followed by the copper screws, and the outer connector. These three pieces are clamped together by the washers and nuts to apply (equal) pressure on the Macor and cured as one item at 120°C for 2 hours. After this, the PEEK spacers and blockers are glued in place using the RT111 glue, and cured for 10 minutes at 65 °C. These steps are shown in Figure 4.14. The PEEK spacers are also glued into the lid (not shown).

The coil corresponding to the custom made spacers is then placed in the casing, with electrical contact made by bending the outer windings into the slits of the copper screws, and glueing them into position using an electrically conductive adhesive[1]. Having ensured that the coil is in electrical contact with the connectors, but not in electrical contact with the casing, the glue is then cured at 65 °C for 10 minutes. Flexible nylon sheets are then cut and placed along the inner and outer sides of the coil[2]. The lid is then placed in position and glued using the RT111 glue which is applied along the inner and outer rims of the body. Screws are also inserted for pressure and sealing purposes before curing at 65 °C for 10 minutes and an overnight curing in air.

4.3.4   Testing of the assembled Feshbach coils

Following their complete assembly, the coils are checked to see if they are leak tight before the temperature response of the coils is measured. This test is important as it allows safe experimental operation currents of the coils to be set. In constant current mode, different currents are passed through the cooled coils, and the voltage response of the coils is recorded. Each current is passed through the coil for 3 minutes with a 5 minute interval to allow the copper to be cooled between measurements. The change in voltage drop across the coil, and therefore the change in resistance, allows the change in temperature of the coil to be established,

---

[1]Circuit Works Silver 0.25oz Tube Epoxy Conductive Adhesive.
[2]In the case of the right coil, these were subsequently removed.
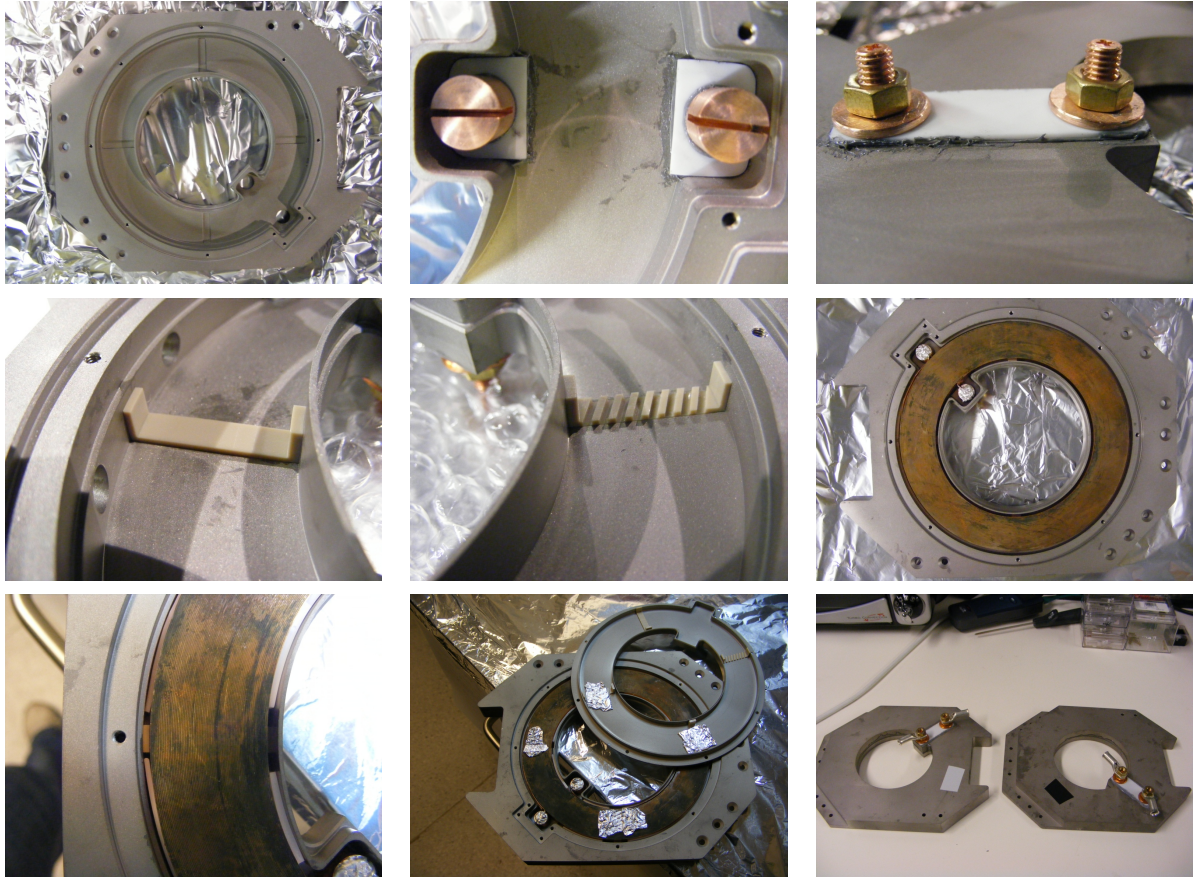
Figure 4.14: Steps in the Feshbach glueing. From left to right, top to bottom: the bare body; the connectors glued from the inside using the Supreme HTND-3 glue; the connectors on the outside of the casing, glued with the Supreme HTND-3 glue and cured for 2 hours at 160°C; the flow blocking spacer between the two entry/exit points of the coolant; a spacer, glued with RT111 glue; the coil inside the case with electrical contact with the connectors made by the use of electrically conducting glue; close up of the side channel and the nylon sheets; the main body and the lid before sealing with RT111 glue around the edges; and the end result.

per Equation 4.17

$$\Delta\rho = \alpha\Delta T\rho_0, \tag{4.17}$$

where $\Delta\rho$ is the change in resistance, α is the temperature coefficient of resistance of the material[1], ΔT is the change in temperature, and ρ_0 is the start resistance of the coil.

The test results for both coils are shown in Figure 4.15. In the case of the left coil (left in figure), a coolant flow of 13 l/min was recorded, and a maximum copper temperature of 45 °C is reached at a current of 90 A. In the case of the right coil, a stent, shown in Figure 4.16, had to be inserted into the casing in order to stop the outer winding of the coil from blocking the coolant flow. A flow rate of 7 l/min with the stent in place was achieved, and a maximum temperature of 46°C is attained at 70 A. This higher temperature at a lower voltage will limit the currents which can be passed through the coils during their operation.
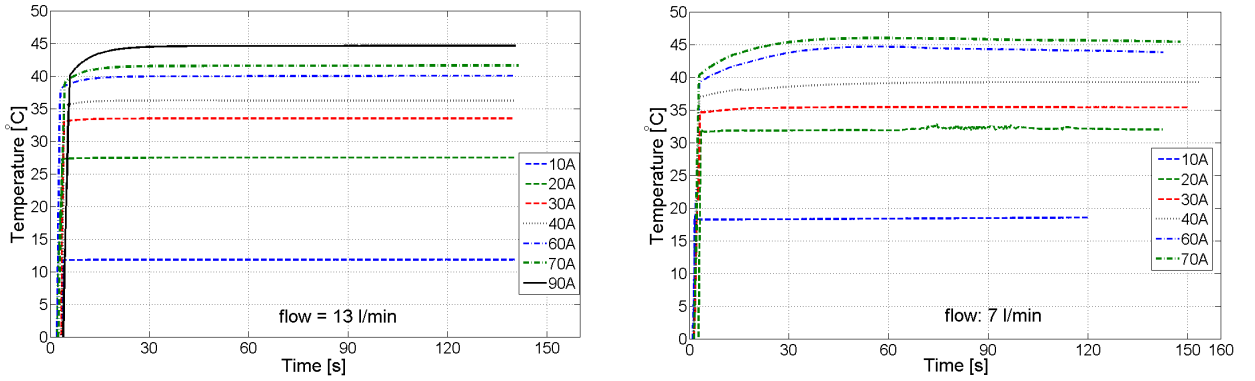
Figure 4.15: Testing of the Feshbach coils. (Left) left Feshbach coil shows that the copper temperature stabilises after 30 s and that the maximum temperature reached with a flow of 13 l/min is 45 °C at 90 A. (Right) stented right Feshbach coil shows that the copper temperature stabilises after 30 s and that the maximum temperature reached with a flow of 7 l/min is 46 °C at 70 A.

Given the difference in flow rate, the difference in temperature of 4 °C when a current of 70 A is passed through the coil can be accounted for by considering the cooling mechanism. In the case of convection, the rate of convective heat transfer, q, is given by Newton's law of cooling [92]

$$q = hA_S\Delta T, \tag{4.18}$$

where h is the convective heat transfer coefficient, A_S is the surface area which is being cooled, and ΔT is

---

[1] $0.0039°\text{C}^{-1}$ for copper [91].
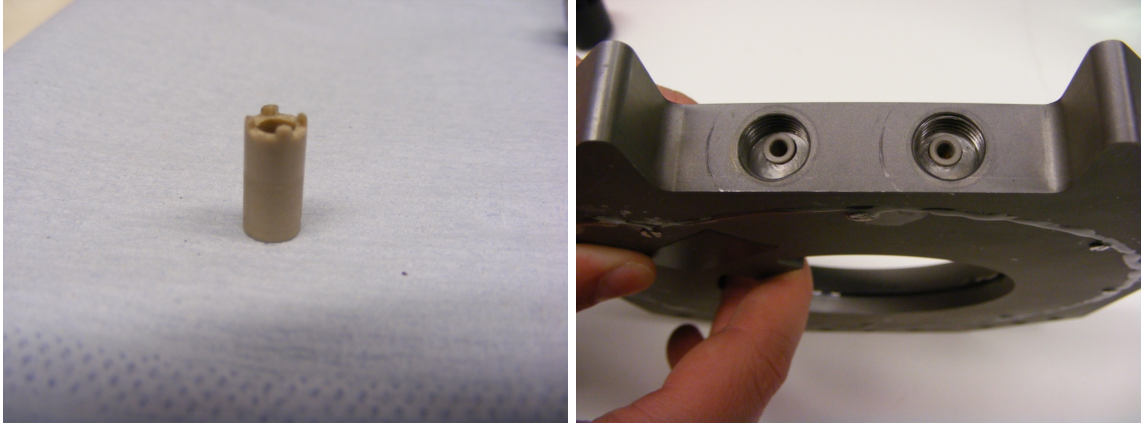
Figure 4.16: Feshbach stent (left) standing alone, the teeth are designed so that flow can still pass, but pressure is still applied, and (right) in situ, in the connector hole; the coolant connector (not shown) screws into the visible thread.

the temperature difference between the coolant and the cooper. The heat transfer coefficient is given by

$$h = \frac{kNu}{D_H},\tag{4.19}$$

where Nu is the dimensionless Nusselt number, k is the thermal conductivity, and D_H is the hydraulic diameter. In the case of a non-circular tube of width w, height l, and cross-sectional area A_c, the hydraulic diameter is given by [93]

$$D_H = \frac{4A_c}{2(w+l)}.\tag{4.20}$$

The Nusselt number is given by [92]

$$Nu = 0.023Re^{4/5}Pr^{0.4},\tag{4.21}$$

where Re is the dimensionless Reynolds number, which characterises the flow regime, and Pr is the Prandtl number, which is the ratio of momentum to thermal diffusivity, given by [92]

$$Pr = \frac{\mu c_p}{k},\tag{4.22}$$

where μ is the dynamic viscosity of the coolant, and c_p is the specific heat of the fluid.

The Reynolds number is given by [92]

$$Re = \frac{\rho Q D_H}{\mu A_c},\tag{4.23}$$

where Q is the fluid flow in the channel in m^3/s. The value of the Reynolds number determines if the flow

Density, ρ	Specific heat, c_p	k	Dynamic viscosity, μ
828 kg/m^3	1920 J.kg^{-1}.K^{-1}	0.140 W.K^{-1}.m^{-1}	8.1· 10^{-4} Pa.s

Table 4.6: Properties of the Paratherm CR coolant, after References [66, 94].
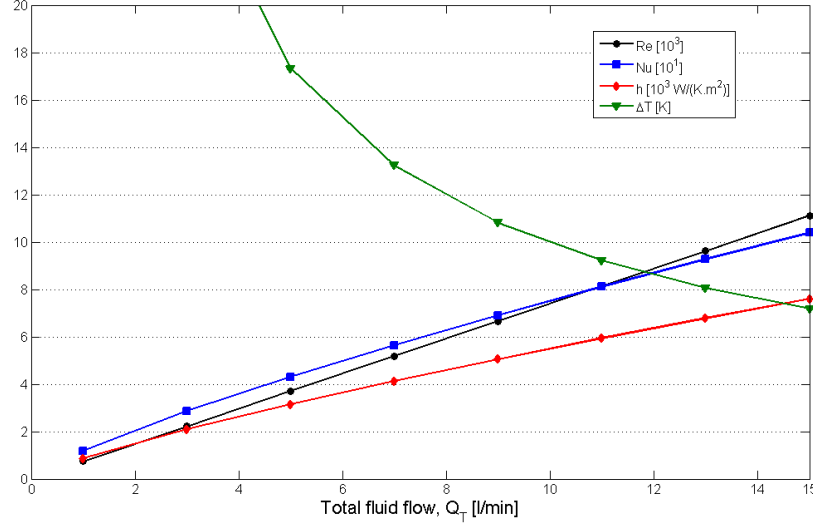
Figure 4.17: Reynolds number, Nusselt number, heat transfer and difference in temperature as a function of total fluid flow, Q_T.

is laminar ($Re \leq 2000$) or turbulent ($Re \geq 2000$).

The flow channel has a width w of 22 mm, a height l of 1 mm, and a cross-sectional area A_c of 22 mm^2. The coil has a surface area A_S of 0.008 m^2. The properties of the coolant[1] used are shown in Table 4.6.

The heat which needs to be dissipated is proportional to the total power, P_T, in the coils. At 70 A, with a voltage drop of 12.5 V across one coil, the power which needs to be dissipated per surface is $P_T/2$, which can be equated to the convective heat transfer, q, in Equation 4.18. The fluid flow on one surface, Q, in Equation 4.23 is half of the total fluid flow, Q_T. From the simulation, shown in Figure 4.17, it can be seen that, at a current of 70 A, the temperature difference between a total fluid flow of 13 l/min and of 7 l/min is of 5 °C, consistent with the difference observed in Figure 4.15.

Obviously, the temperature rise observed is not the $\approx$10 °C of Figure 4.17, as the heating of the coil and of the coolant as it absorbs the heat has to be considered. This is equal to [66]

$$\Delta T_{fluid} = \frac{P}{Q\rho c_p},\tag{4.24}$$

[1]Paratherm CR, Paratherm.

which gives 2.5 K for a total flow of 13 l/min, and 4.7 K for a total flow of 7 l/min. This leads to temperatures in the range of 40 °C, consistent with the values observed.

The testing of the Feshbach coils has shown that they are safe to use at the normal operating currents (55 A) used in the experiment.

4.4   Conclusion

In conclusion, this chapter has highlighted and explained the need for two sets of coils to be redesigned. The new moving coils adapted a different technology, and simulations of the gradient, based on the Biot–Savart law, have been done. Once implemented, the new moving coils show a slightly lower gradient than the previous set. The reduced optical access in the design means that some provisions, such as moving the coils back during the experimental cycle, have to be taken. The new Feshbach coils have been less extensively redesigned, with the focus being primarily on three aspects of the electrical connectors: orientation, materials, and glue. The new coils match the previous ones in terms of gradient, and although the coolant flow is limited and places an upper limit on the currents which are usable, this limit is above the standard experimental operation range. To date, after twelve months in operation, no leaks have occurred at the connectors.

SPATIAL LIGHT MODULATOR SET-UP FOR PHASE IMPRINTING AND VERTICAL IMAGING

This chapter offers a brief review of spatial light modulators (SLMs) before presenting the SLM used in the experiment. The main aim of this chapter is to design, construct and characterise an optical set-up capable of achieving resolution on the order of micrometers for phase imprinting. In order to achieve such resolution, microscope objectives and tube lenses will be used. They will first be characterised, and a test set-up will be presented to determine the possible resolution. Based on the constraints found by the test set-up, a set-up for the experiment will be designed.

5.1 Review of spatial light modulators

Light is a useful way to manipulate atoms, and is regularly used in Doppler cooling, and dipole trapping. For applications, such as the study of vortices or solitons, it can be beneficial to pattern the light.

Patterns can be produced by lithographically etched masks [95], but these masks present the disadvantage that they have to be manufactured, and if any changes are needed, a new mask has to be made.

Spatial light modulators (SLMs), arrays of phase retardation plates of mirrors, allow pixel by pixel manipulation of the light, and can be dynamically changed by simple reprogramming of the image displayed by the SLM.

There are two types of SLMs: phase modulators and amplitude modulators. Phase modulation SLMs rely on arrays of phase retardation plates, with the change in phase being linked to the voltage applied across each plate. The retardation plates are generally based on liquid crystal technology, such as nematic liquid crystals or liquid crystals on silicon (LCoS). Amplitude modulation SLMs rely on arrays of mirrors to manipulate the light. Amplitude modulation SLMs are significantly faster than phase modulation SLMs, with speeds up to

1 kHz [95].

Liquid crystal phase modulation SLMs have been used to produce optical tweezers [96, 97, 98, 99]. They have also been used to demonstrate the possibility of manipulating gates for quantum computation [100, 101], and for cold atom guidance [102]. A ferroelectric light crystal SLM has been used to manipulate a Bose–Einstein condensate [103], although it was limited to binary phase retardation. Recently, a phase amplitude SLM was used to manipulate Rydberg atoms [104].

Phase modulation SLMs can be used for amplitude modulation with the use of polarising optics, as demonstrated in Reference [23], where a LCoS-based SLM was used to create solitons in a BEC.

This experiment uses an amplitude modulation SLM because of its speed and versatility.

5.2 The spatial light modulator

5.2.1 Specifications

The spatial light modulator (SLM) used in this project is a digital micro mirror device (DMD) which is part of the Texas Instruments' D4100 developer's kit [105]. The SLM features 1920x1080 mirrors with a pitch of 10.8 μm and a fill factor of 92.5%. The mirrors tilt with an angle of 12°, and are based on complementary metal-oxide-semiconductor (CMOS) technology. As illustrated in Figure 5.1, the best way of illuminating the SLM is therefore to have light incident at 24° from the normal of the SLM. The use of CMOS technology, and the fact that the mirrors have a lock, means that the SLM mirrors remain stable for any required time span. The SLM is rated for 23,148 frames/second, or an image every 40 μs, which is faster than the correlation time of a BEC. The coatings on the mirrors allow green (532 nm) and near infra-red (780 nm) light to be reflected.

5.2.2 SLM control code

The SLM boards feature two Xilinx Virtex-5 FPGAs for communication and control of the device. The first of these two devices, the DDC4100 chip, features no user programmability. Along with two DAD2400 drivers, it controls the DMD and allows the mirrors to change to an on, off or idle state [105]. The second FPGA device allows the user to communicate and control the board. It is part of the ALP-4.1 application programming interface (API) from ViALUX, the main function of which is to translate user input into a FPGA compatible format. The boards have a refresh rate of 10,700 Hz, which is less than the refresh speed of the SLM mirrors. In order to establish effective communication between the user and the SLM, a command
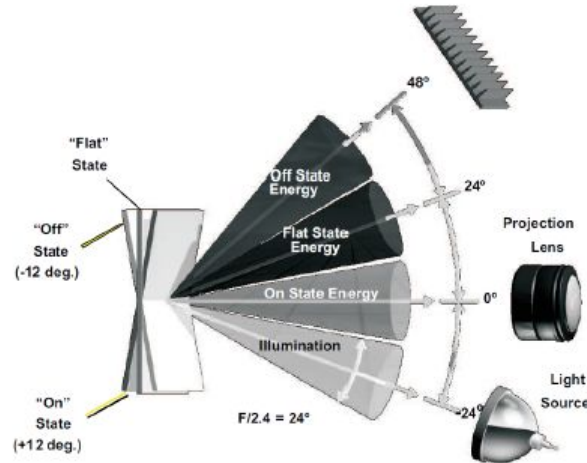
Figure 5.1: Schematic illustration of the illumination angles required for the SLM. From Reference [106].
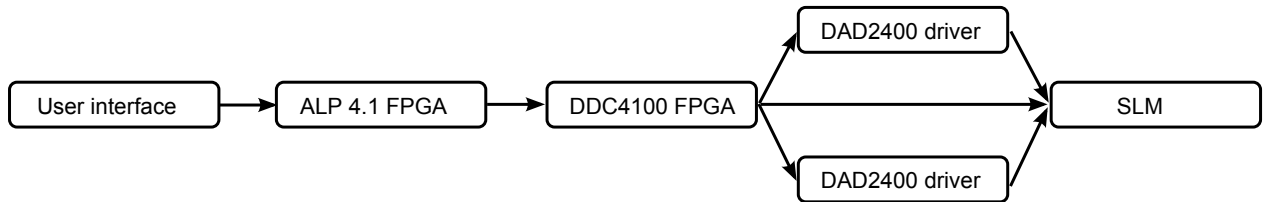
Figure 5.2: Logic diagram of the SLM control.

line argument code was developed [107]. Within the functions of the program, images and sequences can be sent to the SLM, which can be externally triggered. Within the external triggering, the ViALUX device has to communicate with the DDC4100 chip, which adds a delay to the processing speed. The SLM is therefore practically limited to a refresh time of 108 μs per image (equivalent to a refresh rate of 9,250 Hz) [107]. This time scale is of the same order as the correlation time of a BEC. The SLM requires the file format to be a RGB bitmap file composed of 1080×1920 pixels.

5.2.3 Diffraction pattern off of the SLM

Tests to verify the illumination angles necessary for the SLM were carried out, and found that for an input angle of 24°, the 'on pixels' were reflected at 0°, and the 'off pixels' at −48°, as per the specifications [106], irrespective of collimated or divergent light. A test inputting light at 0° found that on light was at 24°, and off light at −24°, consistent with expectations. It was however noted that the pattern off the SLM appeared diffracted, as shown in Figure 5.3.
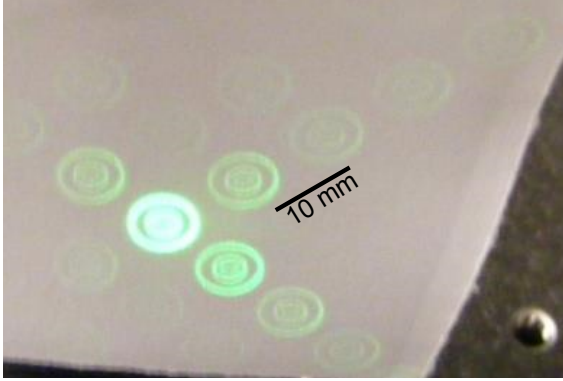
Figure 5.3: Photograph of the pattern observed coming off of the SLM using collimated light.
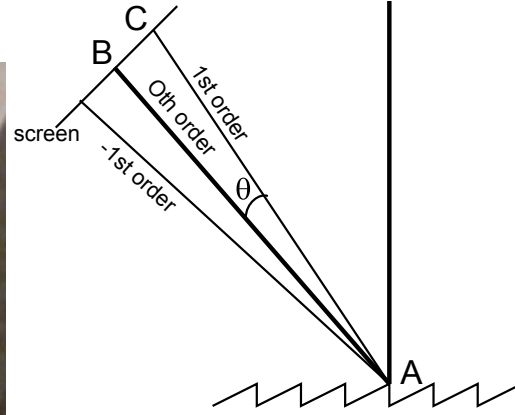
Figure 5.4: Schematic representation of the conventions used to discuss the diffraction pattern. The light is incident at 90° to the SLM, but the mirrors are tilted at 12°, leading to an exit pattern at 24°.

To verify that the pattern is a diffraction pattern, the position of the circles was marked on a screen[1]. The centre of the circles was found to form a square lattice, with a lattice constant of ≈10 mm. The diffraction law states that:

$$d\sin\theta = m\lambda, \tag{5.1}$$

where d is the separation of the 'diffractors' (the mirrors in this case), θ is the angle of the incident light, n is the order number, m is the diffraction order, and λ is the wavelength of the light. Substituting in $d=$ 10.8 μm, $m = 1$, and $\lambda=$ 532 nm yields an angle θ of 2.8°. Using the convention shown in Figure 5.4 with $\theta = 2.8°$, and a distance AB of 182 mm, yields a distance BC of 9 mm, which is close to the 10 mm spacing observed, indicating that the pattern is indeed a diffraction pattern. The presence of a diffraction pattern will result in a loss of power, as some of the light reflected off of the SLM will be lost to higher orders which will not pass through the physical aperture of the imprint system discussed below.

5.3 Characterisation of the vertical optics

In order to use the SLM for manipulating the 2D BEC, the SLM image needs to be demagnified onto the BEC via an vertical illumination system. A detection system capable of resolving the magnified image needs to be designed [80]. In order to obtain the necessary resolution, on the order of micrometres, microscope objectives and corresponding tube lenses will be used to build a vertical illumination set-up, as the BEC is

---

[1]Placed 182 mm away from the SLM.
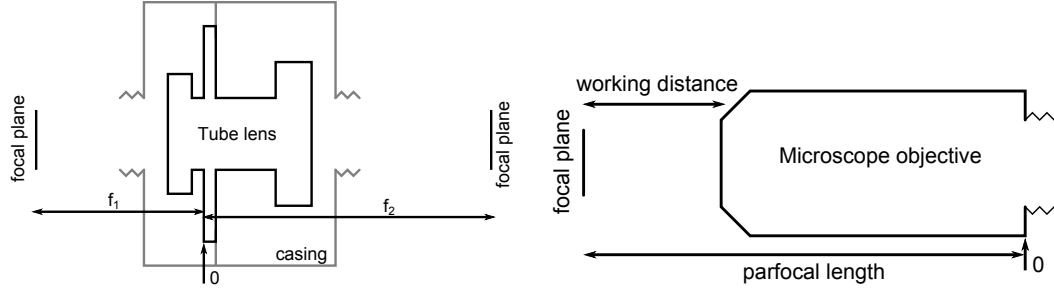
Figure 5.5: (left) Schematic representation of the tube lens (left) and the microscope objective. The tube lens (black) is shown inside its holder (grey). (right) Schematic representation of the microscope objective, illustrating the focus plane, the working distance, and the parfocal length. In both cases the '0' indicates the reference point used in measurements.

designed to be 2D in the horizontal plane.

This section introduces the necessary terminology, characterises the tube lens and microscope objectives, and tests the resolution of the illumination system. It also characterises the effects of having beamsplitters in the beam path, as they will be necessary to combine the light from the SLM, which will be used to manipulate the condensate, and the light from the imaging system, which is used to probe the condensate.

5.3.1 Terminology

The term 'tube lens' refers to the f = 200 mm tube lens[1], shown schematically in Figure 5.5.

The microscope objectives available are the M-plan APO x5, x10, and the G-Plan APO x20 and x50 objectives[2]. The G-plan APO objectives feature a correction to account for transmission through glass of thickness 3.5 mm [108]. The objectives' properties are collated in Table 5.1. The working distance is the distance between the top of the objective, and the location where it focuses. The parfocal length is the distance between the back of the objective and the focal point of the objective. Both of these are shown in Figure 5.5. The depth of field is the range along the optical access where the image is optimally focused [109]. Resolution is defined as per the Rayleigh criterion which states that two points can be resolved if the distance between them is greater than R, which is given by [81]

$$R = 1.22\frac{\lambda}{2NA},$$

(5.2)

where λ is the wavelength of the light, and NA is the numerical aperture of the objective.

---

[1]MT-1, Mitutoyo.
[2]All from Mitutoyo.

Microscope	Numerical Aperture	Resolution [μm]	Magnified Resolution [μm]	Focal Length [mm]	Parfocal Length [mm]	Working Distance [mm]	Length [mm]	Depth of Field [μm]
M x5	0.14	2.3	11.5	40	95	34	61	14
M x10	0.28	1.2	12	20	95	33.5	61.5	3.5
G x20	0.28	1.2	24	10	96.16	30.6	65.59	3.5
G x50	0.5	0.65	32.5	4	96.16	15.08	81.11	1.1

Table 5.1: Properties of the available M-plan and G-plan APO objectives: the Numerical aperture (NA), the resolution (as per the Rayleigh criterion), the magnified resolution, the focal length, the parfocal length, the working distance, the physical length of the microscope and the depth of field. The wavelength is taken as being 532 nm. All numbers other than the wavelength specific resolution and magnified resolution are taken from Reference [108].

5.3.2 Characterising the optical elements

Characterisation of the tube lens

The tube lens was characterised by verifying the focal points of the lens.

Collimated light was put through the tube lens, and the focal point was determined by looking at the position of the shadow of a razor blade placed in the beam on a screen, as illustrated in Figure 5.6. The tube lens was then flipped and the test was repeated. Depending on the orientation of the tube lens, different focal lengths (160 mm and 240 mm) were found. A nomenclature of 'normal' and 'inverted' orientation of the tube lens, illustrated in Figure 5.7, is used. In the normal orientation, collimated input light[1] is focused at a distance of 160 mm, whereas in the inverted orientation, the focus is at 240 mm.

Characterisation of the microscope objective

The microscope objective displayed the expected features. If the light on the tube lens is divergent, resulting in collimated light between the tube lens and the microscope objective, then the distance between the tube lens and the microscope objective is not critical. However, if the light on the tube lens is collimated, resulting in converging light between the tube lens and the microscope objective, the distance between the tube lens and the microscope is critical. This distance should correspond to the focal length of the tube lens, if the light out of the microscope objective is to be collimated. Because of the sensitivity of the distance, the microscope objective is placed on a x-y translation stage for the remainder of the tests.
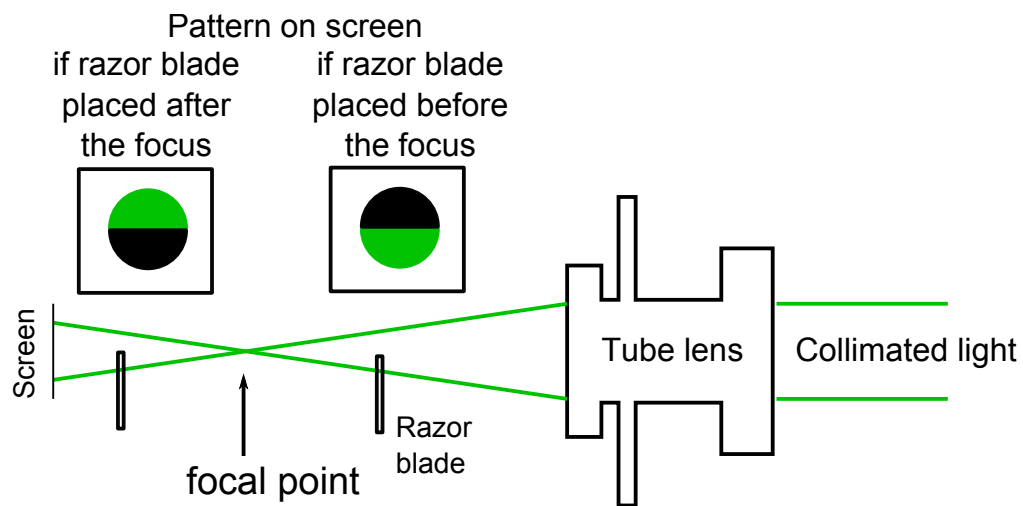
---

[1]with 532 nm light

Figure 5.6: Schematic representation of the set-up used to establish the position of the focal lengths of the tube lens. The test was carried out using both orientations of the tube lens, not shown.
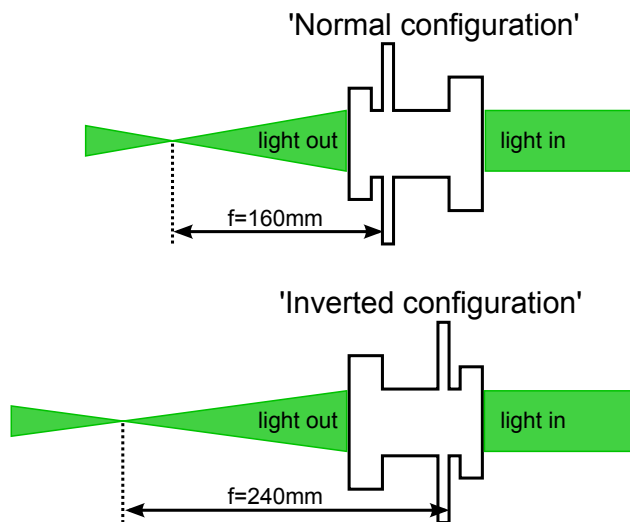

Figure 5.7: Tube lens orientation convention: above the 'normal' configuration, and below the 'inverted' configuration.
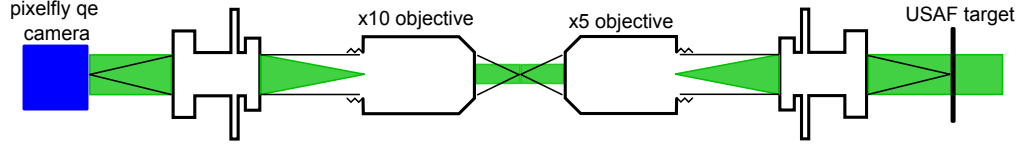
Figure 5.8: Schematic representation of the full test set-up. The USAF target is on an x-y-z translation stage, the illumination light is collimated. The image of the USAF target is at the focal point of the first microscope objective. The illumination light is shown in green, and the path of the information-carrying light is shown with black lines.

5.3.3 Characterisation of the optical set-up

In order to phase imprint onto the BEC, the pattern from the SLM needs to be demagnified. This is done using the tube lens and the microscope objective. Previous work[65, 110], aimed at creating a set-up to generate disordered potentials, characterised a set-up with two glass corrected G-plan APO x50 microscope, found a resolution of 1.1 μm. Due to the presence of the glass correction, any tilt between the glass cell and the objectives significantly affected the resolution. As soliton generation requires less resolution than for a disordered potential, a set-up using non glass corrected microscopes is characterised using a target in this chapter.

Positioning of the optical elements

Placing a camera at the focus of the microscope objective yielded pixel limited results. Consequently, the vertical detection optics [80], which consist of a microscope objective, a tube lens and a camera[1], were added to the set-up.

The detection microscope objective, also on a translation stage, was placed such that the focal planes of both the detection and 'illumination' microscope objectives overlap. This was verified by ensuring that the light coming out of the second objective is collimated when divergent light is used.

As already discussed in Section 3.4, in the case of imaging, the atoms are considered to be a point source, thereby the light carrying the information is divergent as it reaches the microscope objective. Assuming that the atoms are in the focal plane of the microscope objective, the light will therefore be collimated between the objective and the tube lens, meaning that this distance can be shorter or longer than the focal distance of the tube lens. After the tube lens, the light will be convergent, therefore the position of the camera matters. In the vertical detection, the microscope objective to tube lens distance is 112.52 mm and the tube lens to camera distance is 240 mm [80].

---

[1]Pixelfly qe, PCO.

Effects of optical objects in the beam path

The final set-up will be used for imprinting patterns on the BEC and for imaging the BEC. Due to the difference in frequencies[1] and powers[2] needed for imaging and imprinting, two different beams are required. These beams need to be combined in such a way as to not negatively impact the accuracy of the pattern. As the SLM is too slow, with a refresh rate of 108 μs compared to typical literature imprint times ≈ 40 μs [23], the beams have to be combined by the use of a beamsplitter.

The aim of the characterisation of the set-up is therefore two-fold: firstly, to quantify the resolution of the system, and secondly, to measure the effects of any beamsplitters on the resolution. Based on the characteristics of the microscope objectives given in Table 5.1, the resolution is expected to be on the order of 1–10μm. The beamsplitters, a $1''$ cube polarising beamsplitter and a thin $2''$ round polarising beamsplitter, were individually placed between the USAF target[3] and the tube lens, and between the tube lens and the microscope objective. The presence of optical elements in the beam path is expected to significantly affect the resolution quality. However, by correcting for the displacement due to beam reflection inside the optical elements, a near-optimal resolution is expected to be regained.

In order to carry out these experiments, the set-up shown in Figure 5.8 was used. The logic of the test is shown in Figure 5.9. The 532 nm light was collimated and placed at a distance from the first tube lens. The USAF target was placed on an x-y-z translation stage[4] near the focal point of the first tube lens and focused. The optical object is placed in the beam path, the image taken, and then the position of the USAF target is adjusted, mainly along the x direction, until the image is focused. The objects are placed either between the USAF target and the tube lens or between the tube lens and the microscope objective, as these are the two places where the beams can be combined.

The resolution of the system is determined by the smallest group and element of the USAF target resolved in the image, as per the protocol described in Appendix C. The results are shown in Table 5.2 for the normal configuration of the tube lens, and in Table 5.3 for the inverted orientation of the tube lens. The distances the target had to be moved by are given in Table 5.4.

The results show that, if the optical object is placed between the tube lens and the objective, both the $1''$ cube and the $2''$ round beamsplitters allow the original resolution to be attained with no movement of the USAF target necessary. In the case of the optical object being placed between the target and the tube lens, only the $1''$ cube PBS allows the original resolution to be attained.

---

[1]On resonance for imaging, at least 6 GHz detuning for imprinting.
[2]mW for imprinting [42] and μW for imaging due to the saturation parameter.
[3]1951 USAF $2'' \times 2''$ target,Edmund Optics.
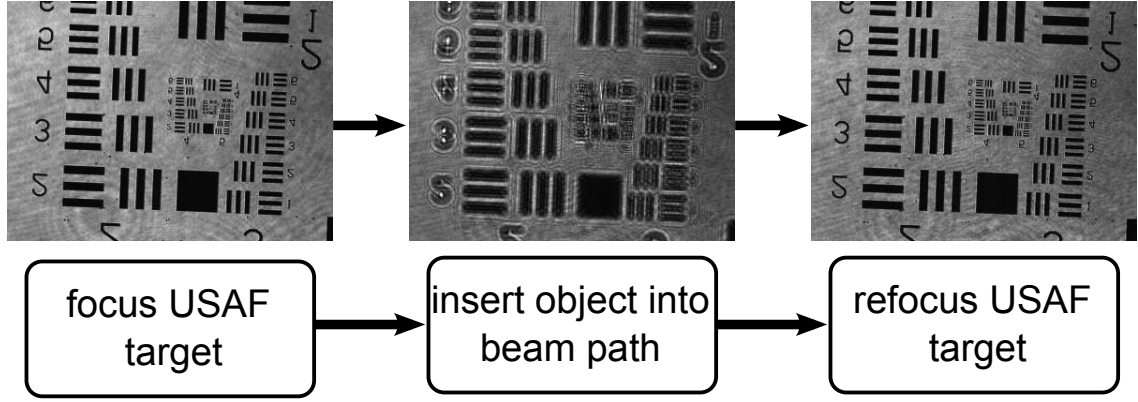[4]Thorlabs PT3, $1''$ travel.

Figure 5.9: Logic diagram of the full test: the reference image is taken, the object is placed, and the USAF target is repositioned for the best possible image. Contrast is lost by the addition of the optical element.

The smallest group and element lines resolved on the USAF target are 15.6 μm apart. With the x5 microscope objective focusing the image of the target onto the focal plane, this corresponds to a resolution of 3.1 μm, above the 2.3 μm expected, see Table 5.1. This discrepancy can potentially be explained by contrast limitations on the images [111].

With reference to Table 5.4, the fact that no adjustment to the position of the target is necessary when the beamsplitters are placed between the tube lens and the objective is fully explained by the fact that the information-carrying light is collimated between the two, and hence the image quality is not affected. The amount of adjustment necessary when the object is placed between the USAF target and the tube lens is different for the two beamsplitters. As expected, the thicker beamsplitter requires more movement than the thinner one, and the adjustment difference is the same for each object in both configurations. The 14 mm correction for the 1″ cube beamsplitter is consistent with expectations based on Snell's law, which gives a displacement of ≈12.8 mm, see Appendix D. The offset is of 4 mm for the 2″ round beamsplitter. The resolution is significantly better with the 1″ cube beamsplitter, matching the original resolution, than with the 2″ round beamsplitter, where the resolution is significantly affected.

In conclusion, by using a USAF target, it has been shown that the group and element of the USAF target with a 15.6 μm separation, corresponding to a 3 μm resolution, can be resolved by the set-up. This distance is on the order of healing lengths, which have typical values in the range of ≈1 μm. The addition of a 1″ cube or 2″ round beamsplitter between the tube lens and the objective does not adversely affect the imaging quality, as the information-carrying light is collimated at that point. If the optical element is placed between the USAF target and the tube lens, the target has to be moved along the optical axis in order to correct for beam displacement induced by the optical element. This is a displacement of 14 mm in the case of the 1″

65
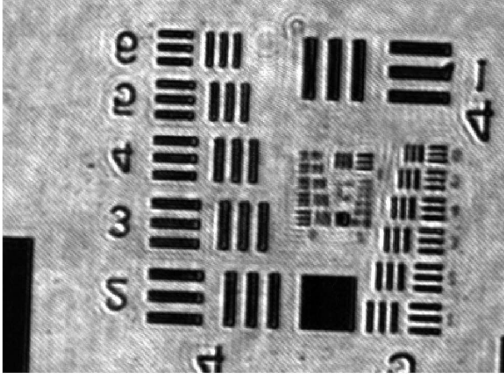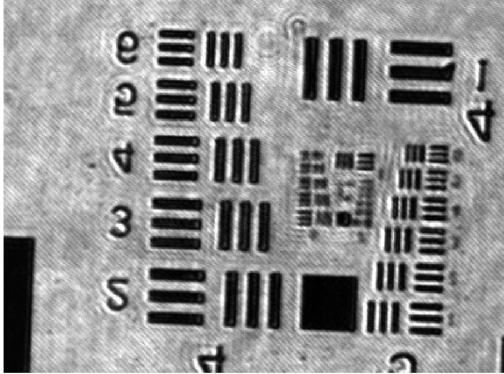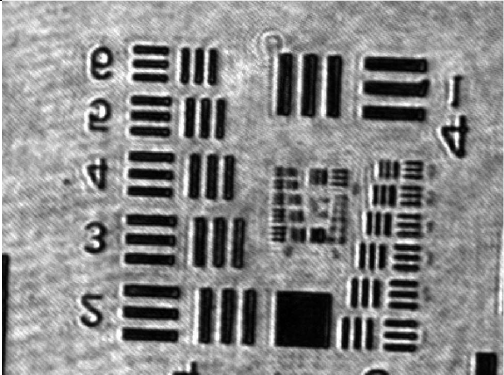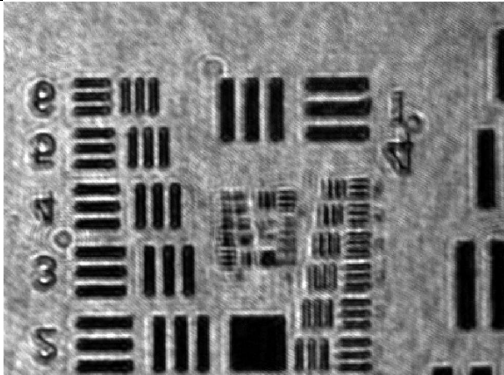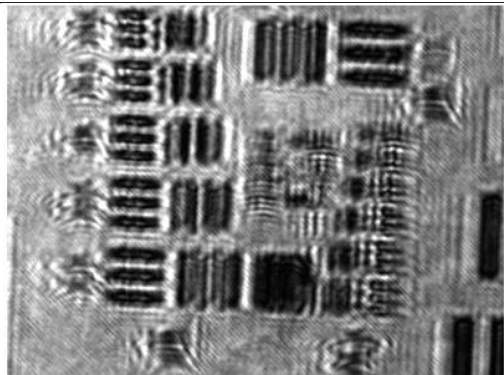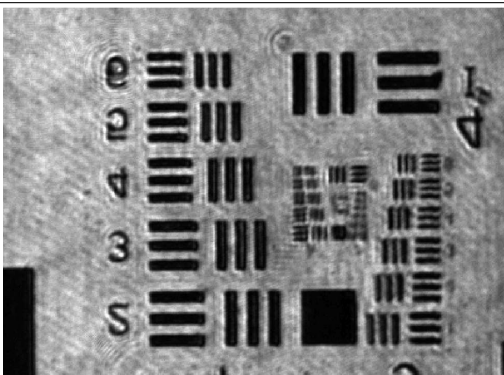
Normal configuration		
Object	Between the target and the tube lens	Between the tube lens and the objective
None	64 lp/mm = 15.6 μm	64 lp/mm = 15.6 μm
1″ cube PBS	64 lp/mm = 15.6 μm	64 lp/mm = 15.6 μm
2″ round PBS	16 lp/mm = 62.5 μm	64 lp/mm = 15.6 μm

Table 5.2: The best adjusted images and resolved USAF group elements for different objects placed in the beam path. The objects are located either between the target and the tube lens or between the tube lens and the objective. These images are post-processed using a contrast enhancement function, and only show the region of interest in determining the resolution of the system. The tube lens is in the normal configuration. Table 5.3 shows similar results for the inverted configuration. Table 5.4 shows by how much the target had to be moved.
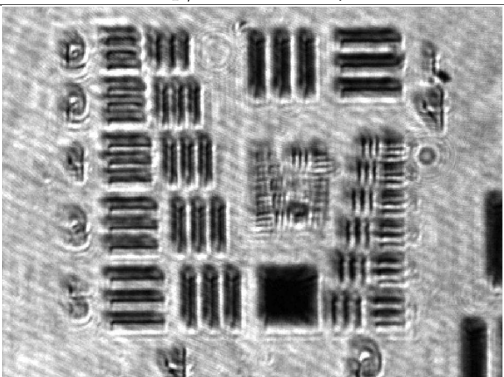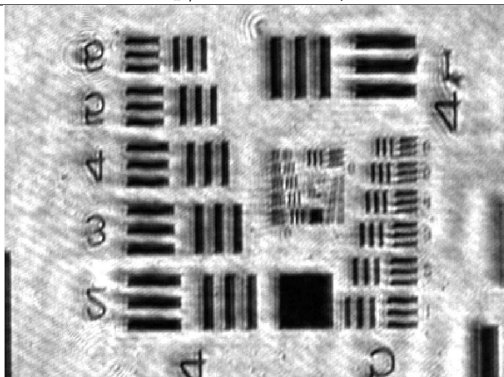
Inverted configuration		
Object	Between the target and the tube lens	Between the tube lens and the objective
None	64 lp/mm = 15.6 μm	64 lp/mm = 15.6 μm
1″ cube PBS	64 lp/mm = 15.6 μm	64 lp/mm = 15.6 μm
2″ round PBS	57 lp/mm = 17.5 μm	64 lp/mm = 15.6 μm

Table 5.3: The best adjusted images and corresponding resolved USAF group and elements for different objects placed in the beam path. The objects are positioned either between the target and the tube lens or between the tube lens and the objective. These images are post-processed using a contrast enhancement function, and only show the region of interest in determining the resolution of the system. The tube lens is in the inverted configuration. Table 5.2 shows similar results for the normal tube lens configuration. Table 5.4 shows by how much the target had to be moved.

Configuration	Object	Placement of the object	
		Target-tube lens	Tube lens-objective
Normal	None	238 mm	238 mm
	1″ cube PBS	252 mm	238 mm
	2″ round PBS	242 mm	238 mm
Inverted	None	160 mm	160 mm
	1″ cube PBS	174 mm	160 mm
	2″ round PBS	163 mm	160 mm

Table 5.4: Table summarising the results of the optics testing. When the object is placed between the tube lens and the objective, no adjustments in the x-plane are needed. If the object is placed between the target and the tube lens, corrections need to be applied. For the 1″ cube beamsplitter, the correction restores a good quality image, which is not the case for the 2″ round beamsplitter (c.f. Tables 5.2 and 5.3).
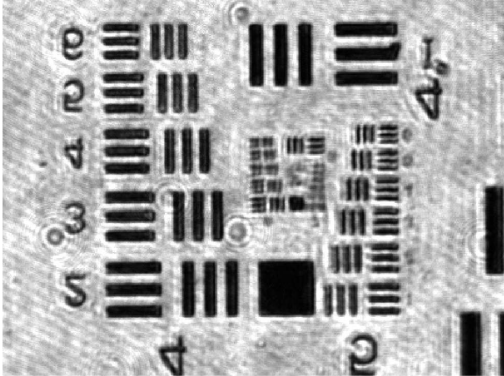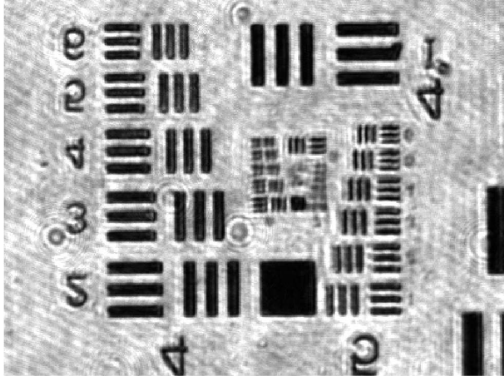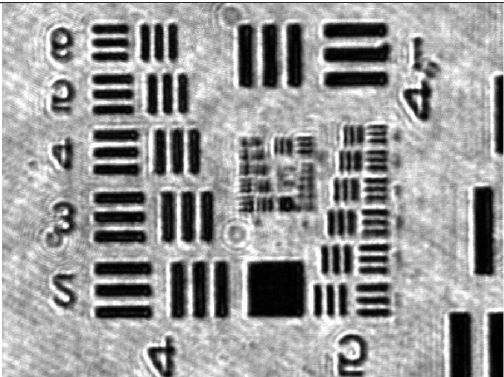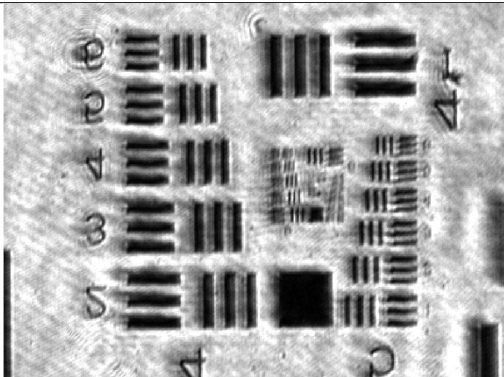
cube beamsplitter for both orientations of the tube lens, and of 4 mm in the case of the round beamsplitter. Only the 1″ cube beamsplitter allows the original resolution to be attained.

5.4   Design of the vertical illumination

The vertical illumination system can be seen as having two parts, the illumination optics, and the SLM optics. The illumination optics demagnify the image on the SLM onto the atom plane, and provide collimated light for the detection system. The characterisation presented in Section 5.3.3 imposes conditions on the design. The SLM optics are the optical elements necessary to control the light which impinges on the SLM.

5.4.1   Design of the vertical illumination system

The vertical detection has to be mobile in the vertical direction in order to follow the BEC as it undergoes time-of-flight measurements, meaning a vertical translational movement of up to 11 mm in the glass cell (see Section 3.1). The illumination, which will also be used to perturb the BEC, needs to be mobile in the x, y, and z directions so that the perturbation can be focused on the trapped atomic cloud.

Whilst some groups have elected to pass their imprint beam through the detection optics [42], it was decided that this experiment is to have the detection and imprint/illumination systems uncoupled, with one on either side of the glass cell. A comparative schematic of both types of set-ups is shown in Figure 5.10. The chosen set-up allows different TOF times of the cloud to be studied whilst maintaining the certainty that the imprint is focused on the atomic plane. The chosen set-up also has the significant advantage that the imprint can be accurately placed and characterised by the detection system.

Due to spatial constraints, optics for the vertical detection were placed above the glass cell, and the
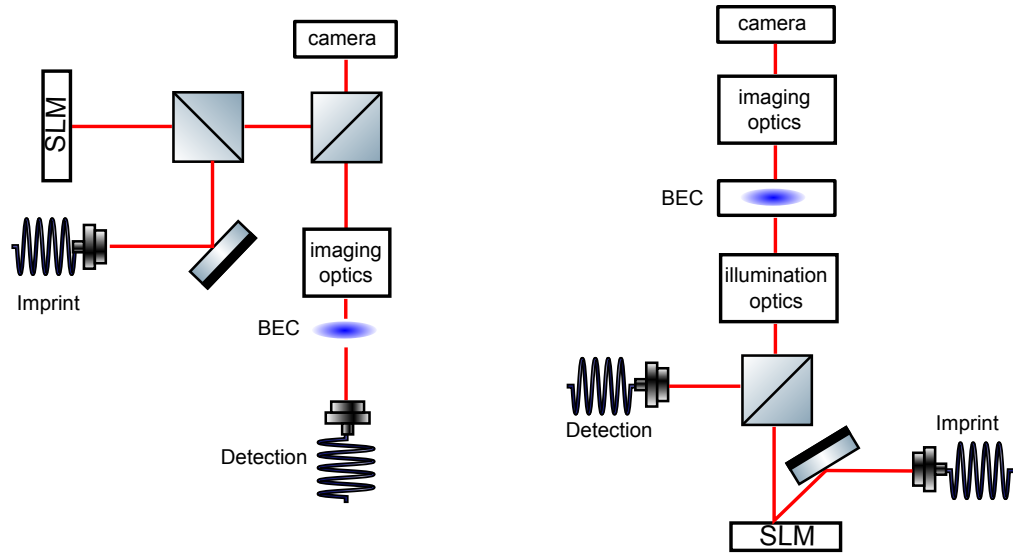
Figure 5.10: Schematic comparing (left) an experimental set-up where the imprint light is passed through the imaging optics and (right) the chosen experimental set-up where the imprint light is passed through it's own optical system. Left hand image after Reference [42].

vertical illumination beneath it. As the illumination system has to act as both an imprint system (imprinting the image of a pattern from the SLM onto the atom cloud) and a collimated detection light source, the optics have to obey a 4-f configuration for both conditions to be met, especially since Section 5.3.2 highlighted the importance of the tube lens- microscope objective distance.

The spatial constraints on the vertical illumination, illustrated in Figure 5.11, are mainly due to the presence of the coils. Because of the need for mobility in all three planes, an xyz translation stage is also required. The x and y translation stages[1] have a total travel of 6 mm, and the vertical translation stage[2] has a total travel of 12 mm. Due to these constraints, the distance between the tube lens and the microscope is set to be 160 mm, which also eases constraints on the optical set-up between the SLM and the tube lens.

Robustness of the illumination set-up is also of importance. The tube lens to microscope distance is therefore fixed by the use of lens tubes, with some in-built flexibility added by the use of variable length lens tubes. A schematic of the final design of the vertical illumination holder is shown in Figure 5.12. A 1″ polarising beamsplitter cube is used to combine the imprint light and the detection light, and is placed between the SLM and the tube lens.

---

[1]KT65-STA, Owis
[2]Owis HV60-12-MS, Owis
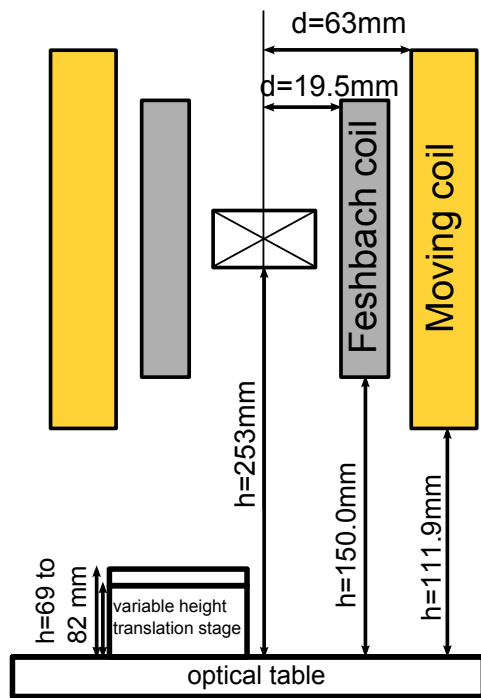
Figure 5.11: Under illumination constraints: the height of the moving coils is the greatest constraint.
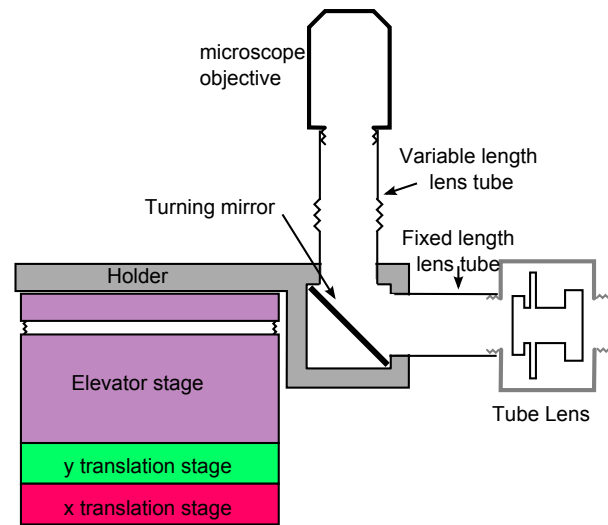
Figure 5.12: Schematic illustration of the under-illumination holder design. The system is robust yet flexible due to the presence of variable length lens tubes. The heights are such that the tube lens fits under the moving coils.

5.4.2 Set-up of the SLM optics

The vertical illumination system is positioned on the experiment, and the SLM optics are designed and shown in Figure 5.13. In order to fully cover the SLM, a telescope, composed of two lenses, expands the beam. The beam can be directed by the guiding mirror, whose primary aim is to ensure that the light impinges on the SLM at the required 24°, and the two mirrors located between the two lenses.

Whilst the SLM is fast, with a refresh rate of 108 μs, it is too slow compared to literature values used for phase imprinting, which are on the order of 40 μs [42]. Consequently, an AOM and shutter are also incorporated into the SLM optics to allow faster switching of the imprint light. To avoid near-resonance stray light from the AOM interfering with the production of the condensate, the AOM is positioned away from the main experiment and the light from the AOM is fibre-coupled to the main table.

The light source is a SolSTiS laser[1], which features wavelengths which can be tuned over a large range. The light from the laser is fibre-coupled to the AOM. The imaging light, from the main laser system, is incorporated via a 1″ PBS.

The coupling efficiency from the laser to the AOM is ≈40%, the efficiency of the transmission into the first order mode of the AOM is ≈80%, and the coupling from the AOM to the main table is ≈70%.

5.4.3 Alignment of the set-up

For phase imprinting, an SLM image focused on the atom plane is required, and full advantage of the separate detection and illumination systems is taken to qualify the imprint. The position of the atom plane must first be established, which can only be done by the vertical detection system imaging a 0 ms ToF BEC.

Once the location of the atom plane has been found, light is shone on the SLM, and the translation stage is primarily moved in the y direction, with some small adjustments on the x direction until the chosen SLM pattern is centred. The stage is then moved in the z direction until the pattern is focused, see Figure 5.14. Maximal illumination is ensured by directing the imprint beam via the three mirrors available.

5.5 Conclusion

In this chapter, a working illumination set-up, based on a SLM, tube lens and microscope objective has been successfully designed and tested, and shown to have a contrast limited resolution of 3 μm with 532 nm light.

---

[1]Msquared Limited.
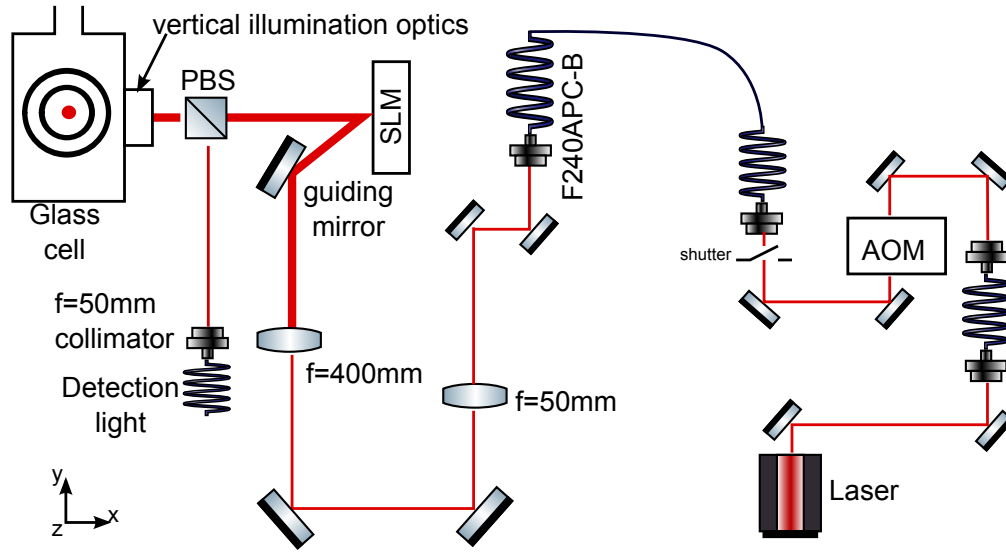
Figure 5.13: Top view of the complete SLM illumination set-up. Light from a variable wavelength laser is fibre-coupled to an AOM. The first order light is fibre-coupled to the main experiment, where the light is collimated. A telescope composed of two lenses (f=50 mm and f=400 mm) expands the beam with two adjustment mirrors in between. A guiding mirror ensures that the light impinges on the SLM at the correct angle. The light from the SLM then goes through a 1″ PBS cube before being focused on the atom cloud by the use of the tube lens microscope system described in Section 5.4.1. The detection light is incorporated into the system at the beamsplitter.
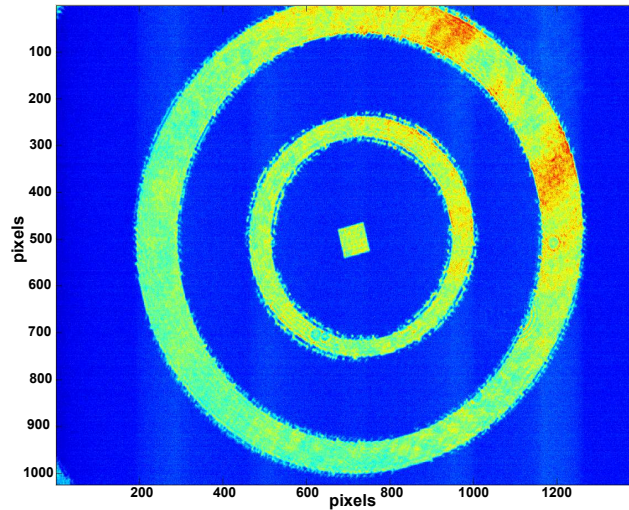
Figure 5.14: Image of the fully focused SLM imprint on the 0ms TOF atomic plane. Blue indicates a low pixel intensity, and red a high one.

CHAPTER 6

TOWARDS SOLITONS IN A BEC

This chapter discusses the number of atoms at different points in the experimental sequence, focusing on the optimisation of the 2D and 3D MOTs for number of atoms. The route to a BEC is presented, and the condensate obtained is characterised. A model to estimate the phase which is imprinted on the condensate for different powers and detunings is presented. Finally, the first results of a 2D soliton are presented, and the soliton is preliminarily characterised.

6.1 Characterisation of the experimental system

In order to reach a BEC, the number of atoms caught in the 2D and 3D MOTs is optimised. Losses incurred at different experimental stages are quantified, and the stability of the system is discussed.

6.1.1 Atom number optimised MOTs

With the 2D MOT, pushing beam, and 3D MOT optimally aligned, the power in the 2D MOT beams and in the 3D MOT beams are individually changed to find the optimum power settings. This is done by loading a single-phase 3D MOT for 10 s in order to characterise the number of atoms. Ten images are taken at each power, the number of atoms is calculated as described in Section 3.4 and averaged. The error is taken as being the standard deviation.

As shown in Figure 6.1, the number of atoms in the 3D MOT increases with the power in the 2D MOT, up to the limit of 16 mW of cooling light in each beam. After this point, the 2D MOT is saturated and no advantage is gained by increasing the power. For the loading of the 3D MOT, the results (Figure 6.2) show that the 3D MOT saturates above powers of 7 mW of cooling power per axial beam. The optimised power of 7 mW is very marked in the case of non-optimised pushing beam power. Even with the pushing beam power
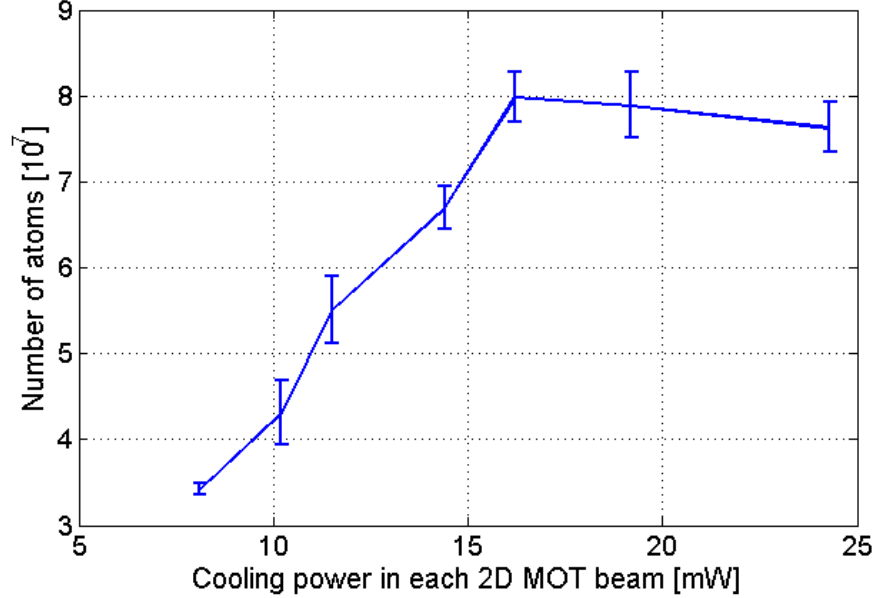
Figure 6.1: Atom number in the 3D MOT as a function of 2D cooling power. It can be seen that up to 16 mW per beam, the greater the power, the bigger the MOT. After this point, the MOT shows saturation. The error bars are the standard deviation of the number of atoms.

optimised for each 3D cooling power, powers above 7 mW do not allow an increase in the number of atoms caught in the trap.

From the results presented in this section, parameters for optimal loading of the MOTs are obtained, and indicate that low powers are preferred.

6.1.2 Stability of the system

The stability of the system is an important aspect of any BEC experiment. As each measurement is destructive, it is vital to have reproducibility from one data point to the next. The stability of the system is therefore characterised at each key point, namely, after MOT loading, after transfer to the moving coils, after transfer to the Feshbach coils, and after the RF evaporation and capture in the dipole trap held at 10 W. In each case, the experiment was left running for one hour, with the lasers being locked just before the start of the experimental run. If the lasers went out of lock, they were relocked.

The stability data for all the aforementioned stages is shown in Figure 6.3, with the error bars being the standard deviation of the measurements. For the 3D MOT loading, transfer into the moving coils, and RF evaporation in the Feshbach coils, the stability of the system is good, with all numbers of atoms being
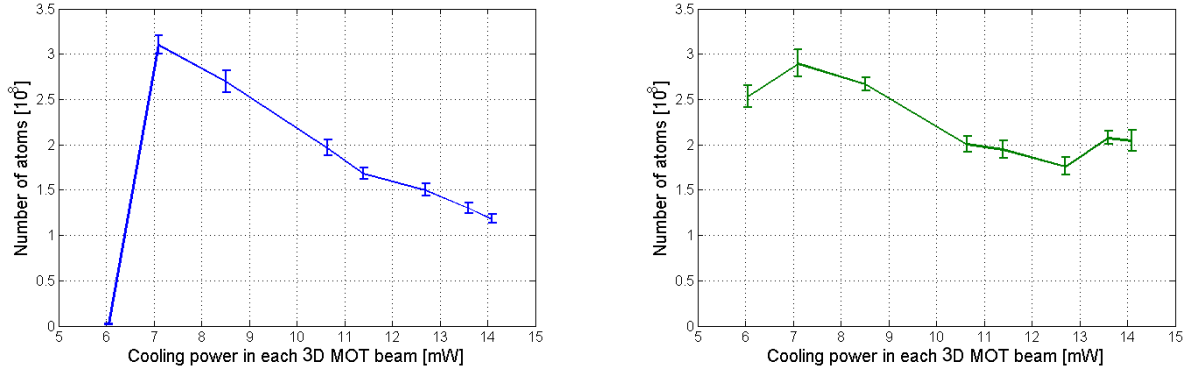
Figure 6.2: Number of atoms in the 3D MOT as a function of 3D cooling power; (left) for a constant pushing beam power, and (right) for an optimised pushing beam power at each cooling power.

consistent with each other. When the atoms numbers are examined together with their uncertainties, they follow the normal distribution around the mean. In the case of the dipole trap, stability is less consistent, with fluctuations on the order of 60% being observed. In the case of the dipole trap, it can be noted that the laser came out of lock (picture numbers 38–42 in Figure 6.3). In order for the laser to come out of lock, fluctuations before that point are expected, which is consistent with the fluctuations observed in picture numbers 28 to 37. Once the laser was relocked stability is again within 10%.

It can therefore be concluded that the system is generally stable, and produces numbers of atoms with fluctuations on the order of 10%. The system does occasionally fluctuate by more than the 10% margin, but this can be remedied by re-locking the lasers, meaning that stability of the system should be monitored throughout an experimental run.

6.1.3   Atom losses

Throughout the experimental cycle, the atoms undergo a number of stages, with transfer between coils, for example. The atom number, calculated as per the process described in Section 3.4.2, at different stages in the experimental protocol is shown in Figure 6.4. The transfer to the magnetic trap results in a loss of 33% compared to the number of atoms originally trapped in the 3D MOT. The transport to the glass cell, with a moving coil current of 83 A, is another source of atom loss, with only 50% of the atoms caught in the magnetic trap making it to the glass cell. This is due to atoms being lost by contact with the differential pumping stage, even though the current in the coils is sufficiently high. The transport to the glass cell therefore acts as a pre-evaporation stage. The transfer to the Feshbach coil is efficient, with 81% of the
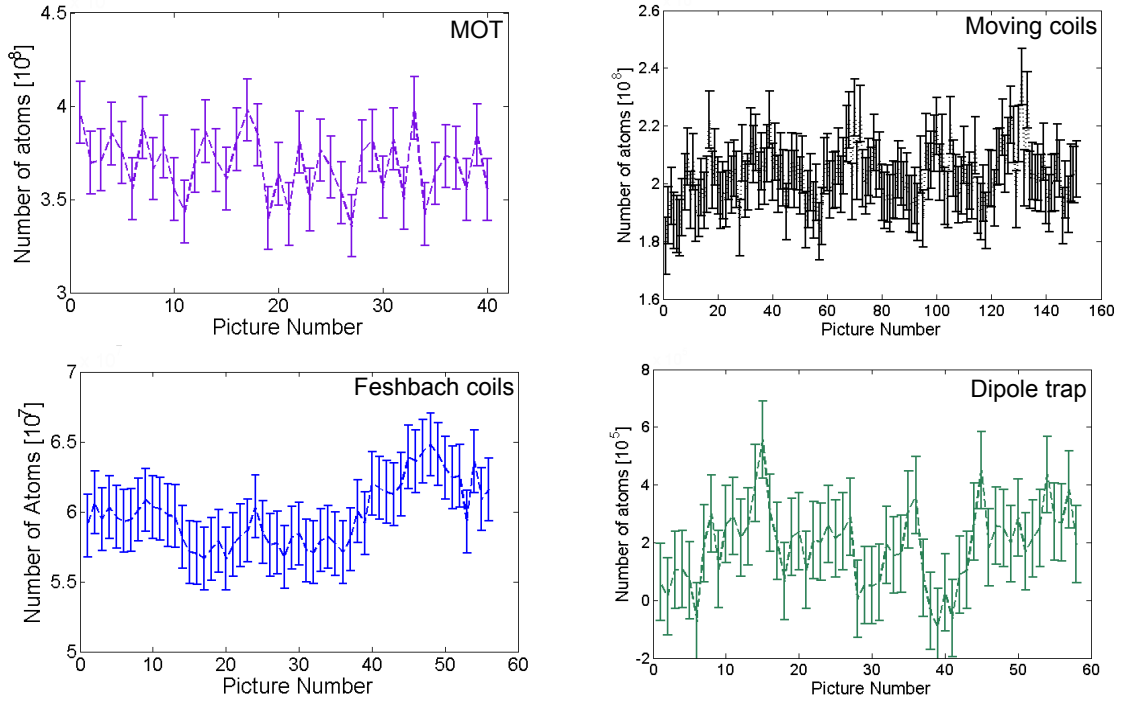
Figure 6.3: Stability of the system at different stages: (top left) after MOT load, (top right) after transfer to the moving coils (images in the MOT), (bottom left) after transfer to the Feshbach coils and RF evaporation, and (bottom right) after transfer to the 10 W dipole trap. Error bars are one standard deviation of the data.
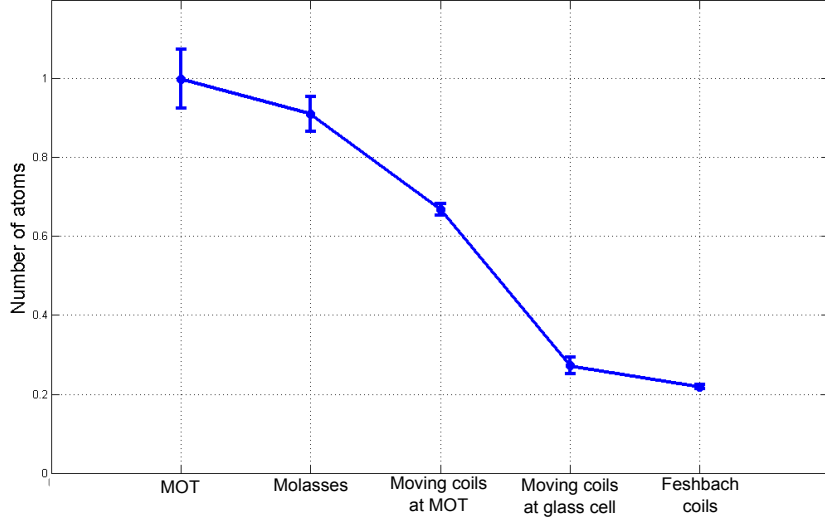
Figure 6.4: Normalised atom number at different stages in the experimental process. There are $(4.3\pm0.3)\cdot$ 10^8 atoms in the 3D MOT.

atoms being transferred.

The presence of losses due to transport reinforces the importance of having atom number optimised MOTs.

6.1.4 Atom temperature at different stages

The number of atoms is not the only relevant aspect of the experiment: the temperature of the atoms is also of importance for obtaining Bose–Einstein condensates. The temperature of the atoms can be experimentally measured by the expansion of the cloud at different TOF times.

When considering the temperature of the cloud, two factors are important: the original shape of the cloud, given by a Gaussian distribution (in the limit of ignoring the effect of the shape of the trap), and the velocity distribution, which is a Boltzmann distribution. A Gaussian distribution is given by

$$G(r_0) = \frac{1}{\sqrt{2\pi}\sigma_0}e^{-\left(\frac{r_0^2}{2\sigma_0^2}\right)},\tag{6.1}$$

where σ_0 is the standard deviation. The Boltzmann distribution is

$$F(v) = \sqrt{\frac{m}{2\pi k_B T}}e^{-\frac{mv^2}{2k_B T}},\tag{6.2}$$

where v is the velocity of the atom, m is the mass of one atom, k_B is Boltzmann's constant, and T is the temperature. The distribution of the atom cloud is therefore given by a convolution of equations 6.1 and 6.2

$$P(r_0, v) = \frac{1}{\sqrt{2\pi}\sigma_0} e^{-(\frac{r_0^2}{2\sigma_0^2})} \sqrt{\frac{m}{2\pi k_B T}} e^{-\frac{mv^2}{2k_B T}}. \tag{6.3}$$

which re-expressed in terms of momentum yields

$$P(r_0, p) \propto e^{-(\frac{r_0^2}{2\sigma_0^2})} e^{-\frac{p^2}{2mk_B T}}. \tag{6.4}$$

With long TOF times, the distribution becomes purely spatial. After a time t, the atoms have moved from their original position r_0 with the momentum p to their new position $r = r_0 + \frac{pt}{m}$. The spatial distribution is then given by

$$\begin{aligned} P(r, t) &\propto \int\int P(r_0, p)\delta(r - r_0 - \frac{pt}{m})drdp \\ &\propto \exp\left(-\frac{mr^2}{2m\sigma_0^2 + 2k_B T t^2}\right) = \exp\left(-\frac{r^2}{2\sigma_{TOF}^2}\right). \end{aligned} \tag{6.5}$$

From Equation 6.5, it can be seen that the standard deviation of the distribution at a given TOF time, σ_{TOF}, can be related to the original standard deviation of the cloud, σ_0, and the temperature, T, of the atoms by

$$\sigma_{ToF}^2 = \sigma_0^2 + \frac{k_B T t^2}{m}. \tag{6.6}$$

The temperature of the atoms at different stages in the experimental protocol, calculated as per above, is shown in Figure 6.5. The atoms are hottest in the MOT (at 2.8 mK), are cooled in the molasses phase to 53 μK. The magnetic trapping induces heating, with the temperature reaching 750 μK). The atoms in the magnetic trap are cooler in the glass cell (240μK), due to contact with the edges of the differential pumping stage. The transfer to the Feshbach coils induces minimal heating (244μK).

6.2 A typical BEC sequence

Up to this point in the chapter, the atom losses and the reproducibility of the number of atoms making it to the glass cell have been characterised. After the transfer to the Feshbach coils, evaporative cooling [6, 112] is undertaken in the Feshbach coils, with the dipole trap at full power to catch the atoms. After the evaporative
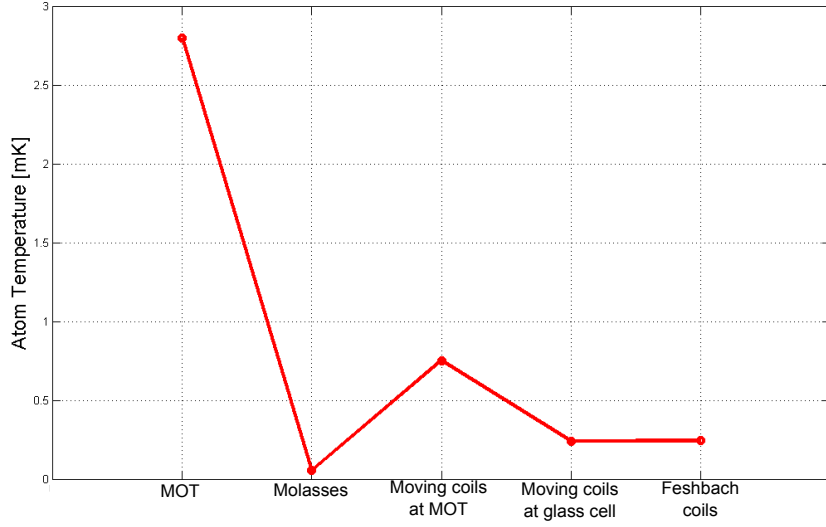
Figure 6.5: Atom temperatures at different stages in the experimental process.

cooling in the Feshbach coils, further evaporative cooling in the dipole trap is undertaken, by lowering the power of the 1550 nm light.

The experimental sequence used to obtain the BEC is shown in Appendix E. The dipole trap is lowered to a voltage of 0.04 V, which, from Figure 3.7, corresponds to a power of 0.04 W. This leads to trapping frequencies of $\omega_x = 2\pi \cdot 5.8$ Hz, $\omega_y = 2\pi \cdot 19.1$ Hz and $\omega_z = 2\pi \cdot 269.4$ Hz. These yield oscillator lengths[1] of $\ell_x = 4.47 \cdot 10^{-6}$ m, $\ell_y = 2.46 \cdot 10^{-6}$ m and $\ell_z = 0.66 \cdot 10^{-6}$ m.

6.2.1 Characterising the BEC

One of the signatures of a BEC is a non-thermal expansion of the cloud, with faster expansions in the more confined direction of the condensate, as schematically illustrated in Figure 6.6.

For a cigar shaped BEC with trapping frequencies $\omega_x = \omega_y = \omega_p$ and ω_z having a ratio $\lambda = \omega_z/\omega_p \ll 1$, the expansion of a BEC is given by [38, 113, 114, 115]

$$r_p(\tau) = \sqrt{1 + \tau^2}, \tag{6.7}$$

$$r_z(\tau) = 1 + \lambda^2 \left[\tau \arctan(\tau) - \ln(\sqrt{1 + \tau^2}) \right], \tag{6.8}$$

---

[1] $\ell_j = \sqrt{\frac{\hbar}{m\omega_j}}$
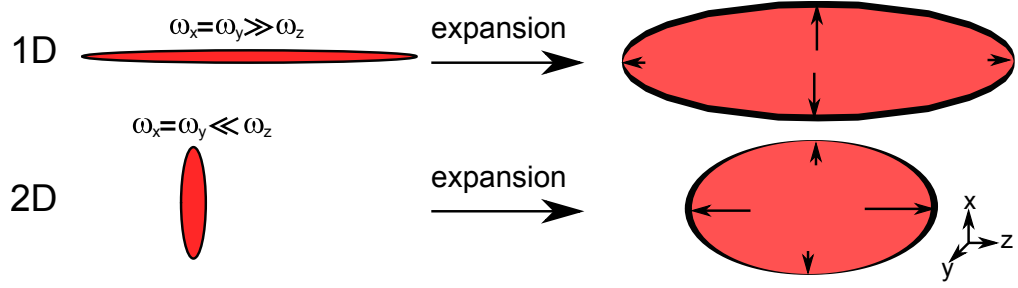
Figure 6.6: Schematic representation of the expansion of a 1D and 2D BEC. Expansion in y is equal to the expansion in x, and is not shown for clarity.

where $\tau = \omega_p t$, r_p is the radial half size of the BEC, and r_z is the axial half-size of the BEC. Consequently, the BEC expands rapidly in the radial direction. In the case of a 2D BEC, the ratio $\lambda \gg 1$ so the expansion is primarily axial [116].

In this experiment, the signature expansion of a BEC results in an elongated cloud in the direction of gravity. The analysis is carried out by using a bimodal fit, one parameter assessing the thermal cloud, the other yielding information about the BEC. The temperature is taken as being the temperature of the thermal cloud, as per Equation 6.5. The analysis, shown in Figure 6.7, gives a BEC composed of 31000 atoms, and a temperature of 88 nK. This is consistent with the 2D critical temperature, of 85 nK (Equation 2.16), and above the 3D critical temperature of 48 nK (Equation 2.6).
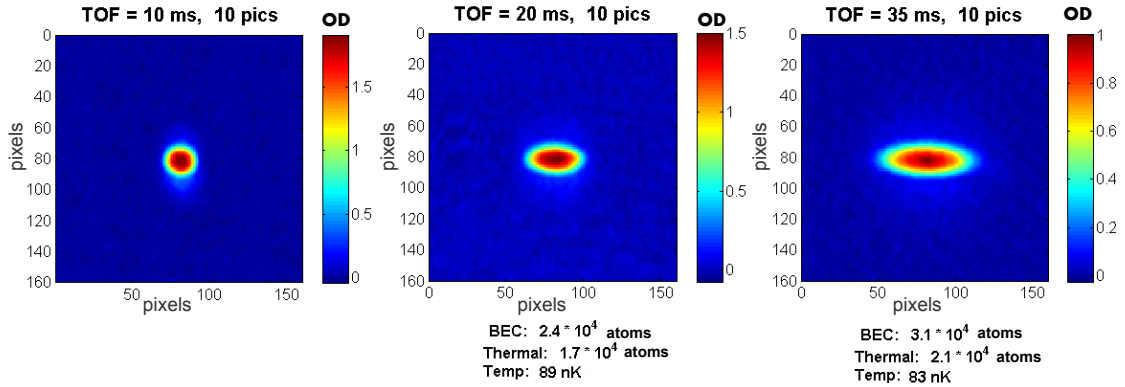
Figure 6.7: Typical BEC, showing a change in orientation as the fall progresses. Gravity is pointing to the right.

In order to further characterise the BEC, quantities such as the chemical potential and the healing length need to be calculated. From Equation 2.11, the 3D chemical potential of the BEC is $\mu_{3D} = 1.85 \cdot 10^{-31}$ J. Substituting into equation 2.14 leads to a 3D healing length of $\xi_{3D} = 4.54 \cdot 10^{-7}$ m, and a correlation time

Dimension	g	μ	n	c_s	ξ	τ
3D	$5.535 \cdot 10^{-51}$ J.m^{-3}	$1.85 \cdot 10^{-31}$ J	$3.34 \cdot 10^{19}$ m^{-3}	$1.13 \cdot 10^{-3}$ m/s	$4.54 \cdot 10^{-7}$ m	400 μs
2D	$3.34 \cdot 10^{-45}$ J.m^{-3}	$1.44 \cdot 10^{-31}$ J	$4.3 \cdot 10^{13}$ m^{-3}	$1.00 \cdot 10^{-3}$ m/s	$5.14 \cdot 10^{-7}$ m	510 μs

Table 6.1: Calculated properties of the BEC in 3D and in 2D.

of $\tau_{corr}^{3D} \approx 400$ μs.

As stated in Section 2.3.1, the criterion for being in the 2D regime is that $\mu_{2D} \ll \hbar\omega_\perp$, where $\omega_\perp$ is the most confining direction. In the trap used in this experiment, $\omega_\perp = \omega_z$. In this case, $\hbar\omega_\perp = 1.78 \cdot 10^{-31}$ J compared to the calculated μ_{2D} value of $1.44 \cdot 10^{-31}$ J (Equation 2.17). By comparing the two numbers, it can be seen that the BEC is just in the two-dimensional regime.

In order to ascertain the dynamics of the BEC, the oscillator length in the confining direction is compared to the (3D) s-wave scattering length, a, which is 5.77 nm. As $\ell_z > a$, the dynamics are 2D whereas the collisions are 3D [44]. With temperatures so close to the transition temperatures, the BEC will not be superfluid.

Having established that the BEC is in the 2D regime, the 2D properties are calculated. The length is $5.14 \cdot 10^{-7}$ m, which leads to a correlation time of $\tau_{corr}^{2D} \approx 510$ μs. Both the 2D and 3D properties of the BEC are collated in Table 6.1.

6.3   Soliton generation

This section introduces the parameters needed to generate a soliton. Firstly, using the theory presented in Section 2.5.2, detuning, power and imprint times for a π-phase imprint are calculated. Secondly, the step used to generate the soliton is characterised. Finally, the parameters used to generate the soliton are given.

6.3.1   Imprint time, detuning and power model

With reference to Section 2.5.2, the imprint light corresponds to a Gaussian beam of diameter[1] $d = 12$ mm. The power, the exposure time and the detuning can all be calculated to yield a π phase shift, which, in a repulsive BEC, corresponds to generating a black soliton. The model assumes no losses on the SLM, the tube lens or the x5 microscope objective, and that the intensity is constant over the area of the beam.

The imprint time, τ, is calculated for different beam powers and detunings. Using Equation 2.27 for the

[1]1.5 mm diameter out of collimator, 50:400 lenses gives a 12 mm beam diameter on the SLM.

duration of the pulse, and Equation 2.30 for the dipole potential, the imprint time, τ, is calculated as being

$$\frac{1}{\tau} = \frac{3\pi c^2 \Gamma}{2\Delta\omega_0^3} \frac{I}{\hbar\pi},$$ (6.9)

where c is the speed of light in vacuo, Γ is the decay constant for ^{87}Rb[1], Δ is the detuning, ω_0 is the frequency of resonant transition[2], and I is the intensity in the beam. The $\hbar\pi$ term allows for a phase imprint of π. In the case of a Gaussian beam, the central intensity, I_0 is related to the power by [117]

$$I_0 = \frac{2P_0}{\pi(D/2)^2},$$ (6.10)

where P_0 is the maximal power in the beam, and D is the diameter of the beam at the atoms.

The model assumes that the intensity is constant, which, as shown in Figure 6.8, is an approximation. If the intensity substituted in Equation 6.9 is taken as being the peak intensity (i.e. $2P_0/\pi(D/2)^2$), the model estimates the shortest amount of time necessary for a point of the condensate to have a phase shift of π. The results in this case are shown on the left in Figure 6.9. The exposure times are short, on the order of 5 μs. If the intensity substituted into Equation 6.9 is the $1/e^2$ intensity ($I = 13.5\% I_0$), then the simulation calculates the time necessary for large parts of the condensate to be exposed to a phase

Figure 6.8: The intensity profile assumed in the simulation (full line), and a more realistic Gaussian intensity profile (dashed line).

shift of π. However, some of the condensate will have been over-exposed, so the number is an overestimate of the time needed to imprint a phase of π on the condensate. The results in this case are shown on the right in Figure 6.9. The imprint times, on the order of 40 μs, are comparable to imprint times used in other experiments [23, 42]. As expected, the two cases display the same behaviour, but the exposure time necessary differs by a factor of 7 (1/0.135) between the two. Experimentally, for a given power and detuning, the simulation offers a range of values for the imprint time which will imprint a π phase shift on the condensate.

The parameters of power, detuning and imprint time can all be experimentally controlled. In order to imprint a soliton, the imprint time must be shorter than the response time of the BEC, namely the correlation time (Equation 2.15), otherwise the BEC will move during the imprint [42]. As stated in Section 5.4.2, the laser

---

[1]6.06·10^6 Hz [67].
[2]2π · 384 · 10^{12} Hz [67].
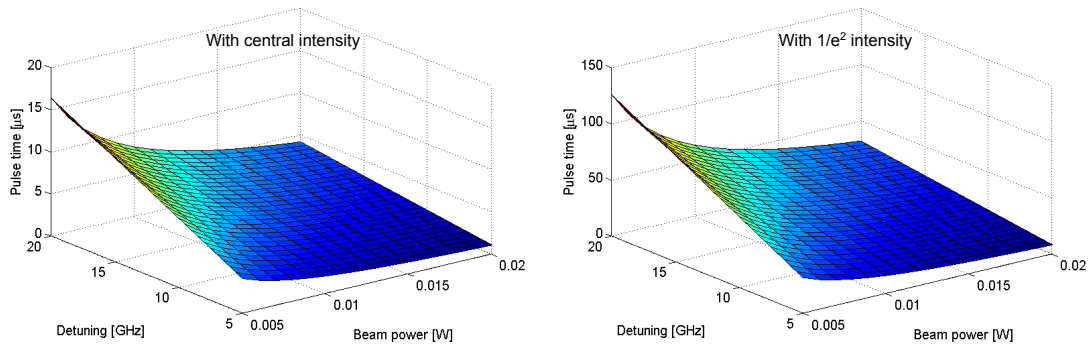
Figure 6.9: Power, detuning and exposure time simulations for imprinting a π phase shift on the BEC with a x5 microscope objective in the set-up. On the left, the intensity of the beam is taken as being the peak intensity. On the right, the intensity is taken as being the $1/e^2$ intensity, which is 7 times smaller than the peak intensity.

is a variable wavelength laser, with a maximum output power of 1.6 W.

As the correlation time of the BEC is of the order of 100 μs, the main experimental limiting factors are the beam power and the detuning.

6.3.2 Characterising the imprint step

In order to position the imprint on the BEC, full advantage of the optical set-up described in Section 5.4 is taken. The atom cloud is imaged with the vertical detection and its position marked. The imprint is then imaged and modified until the position is as required. The imprint is positioned centrally on the BEC, and perpendicular to the long axis of the condensate. The image file of the imprint, and the corresponding imprint are shown in Figure 6.10. The tilt in the image file is due to the fact that the SLM is tilted in its holder.

As can be seen by the line profile in Figure 6.10, the imprint occurs over 5 pixels. With a pixel being 6.45 μm, and an imaging magnification of x10, the step edge is 3.2 μm, which is 6 times the 2D healing length of the condensate.

6.3.3 Generating the solitons

The imprint is made with $\lambda = 780.2596$ nm light[1], corresponding to a 9 GHz red-detuning. The power at the laser is 160 mW, which, due to losses due to various couplings[2], corresponds to 39 mW on the table. This in

---

[1]SolsTiS laser, Msquared Ltd, the wavelength is measured with a wavelength meter.
[2]Fibre-coupling from the laser to the AOM (46%), efficiency of the 1st order of the AOM (82%), and fibre coupling from after the AOM to the main experiment(70%), see Section 5.4.
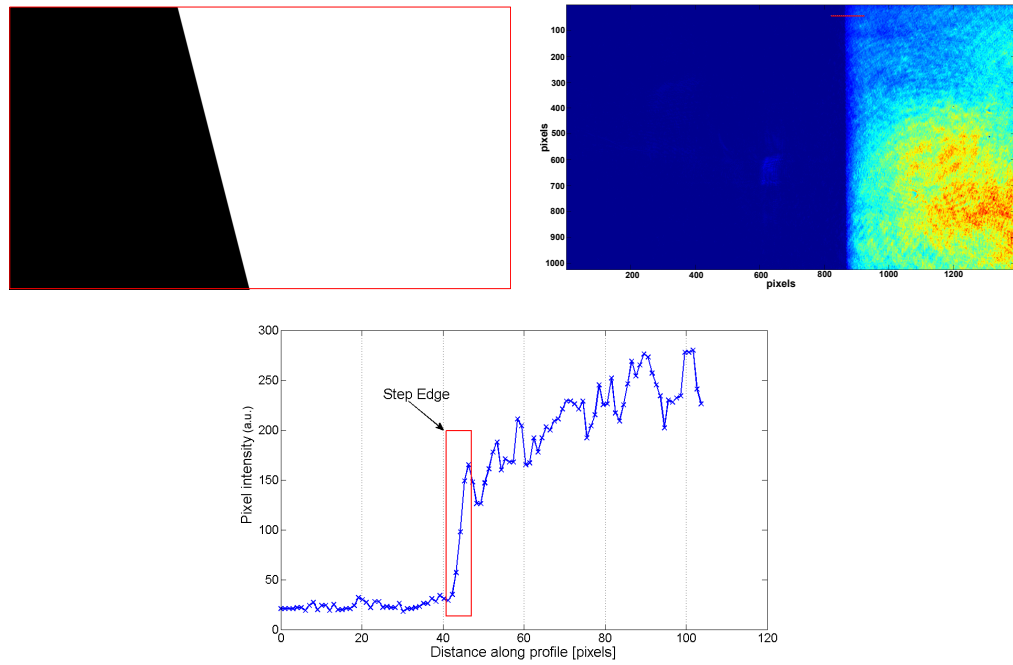
Figure 6.10: Phase imprint used: (left) image on the SLM (the red border is there to define the size of the imprint), (right) image as it appears on the atom plane, with blue being a low pixel value (low light intensity) and red being a high pixel value (high light intensity), and (bottom) line profile corresponding to the red line in the right-hand image.

turn corresponds to 13 mW measured between the x5 microscope objective and the glass cell.

The imprint is applied for a time $t = 50\ \mu$s, which is well below the correlation time. The BEC is left to evolve for a variable hold time in the trap, before being imaged with a 5 ms TOF time in order to increase the resolution of the system due to broadening of the BEC [1, 29, 51].

## 6.4 Characterising the soliton

In this section, the first recorded solitons in a 2D BEC are shown. Preliminary analysis of the soliton feature is presented.

With the imprint parameters described above, the data shown in Figure 6.11 is obtained. The figure shows the top view of the BEC and the optical density projected onto the axis at different evolution times. A sharp dip and a bright peak can clearly be seen at short holding times. The dip is associated with the soliton, and the peak with the sound wave. It can be seen that the dip moves to the left, whereas the peak moves to the right.

Velocity of the soliton

The velocity of the soliton is related to the depth of the soliton. Two preliminary methods of measuring the soliton velocity will now be presented. The first method will bound the values of the velocity, whereas the second method will measure the displacement of the soliton with respect to holding time and thereby infer its velocity. Caution must be taken with the data however, as the images are of a condensate after a 5 ms expansion, meaning that the measured displacements will be larger, due to the expansion. Substituting in a time of 5 ms and an $\omega_p = \sqrt{\omega_x \omega_y} = 2\pi \cdot 10.5$ Hz into Equation 6.7 yields a radial expansion of 5%.

Bounds of the soliton velocity can be established by looking at the depth of the soliton feature. As shown in Section 2.4.2, the closer the soliton velocity is to the speed of sound in the condensate, the shallower the feature. By comparing the depth of the soliton to different 'depth profiles', bounds can be established. Using the 0 ms hold data, one can see that the background parabola of the condensate is disturbed by the presence of the soliton dip and the density peak, see Figure 6.12. The peak of the parabola for an unperturbed condensate will be below the density peak, but above the secondary peak. By normalising to the density peak and overlapping depth profiles, an underestimate of the soliton velocity is made, as shown in Figure 6.12. By normalising to the secondary peak and overlapping depth profiles, an overestimate of the soliton velocity is obtained. By combining both values, a range for the soliton velocity can be established. The comparison
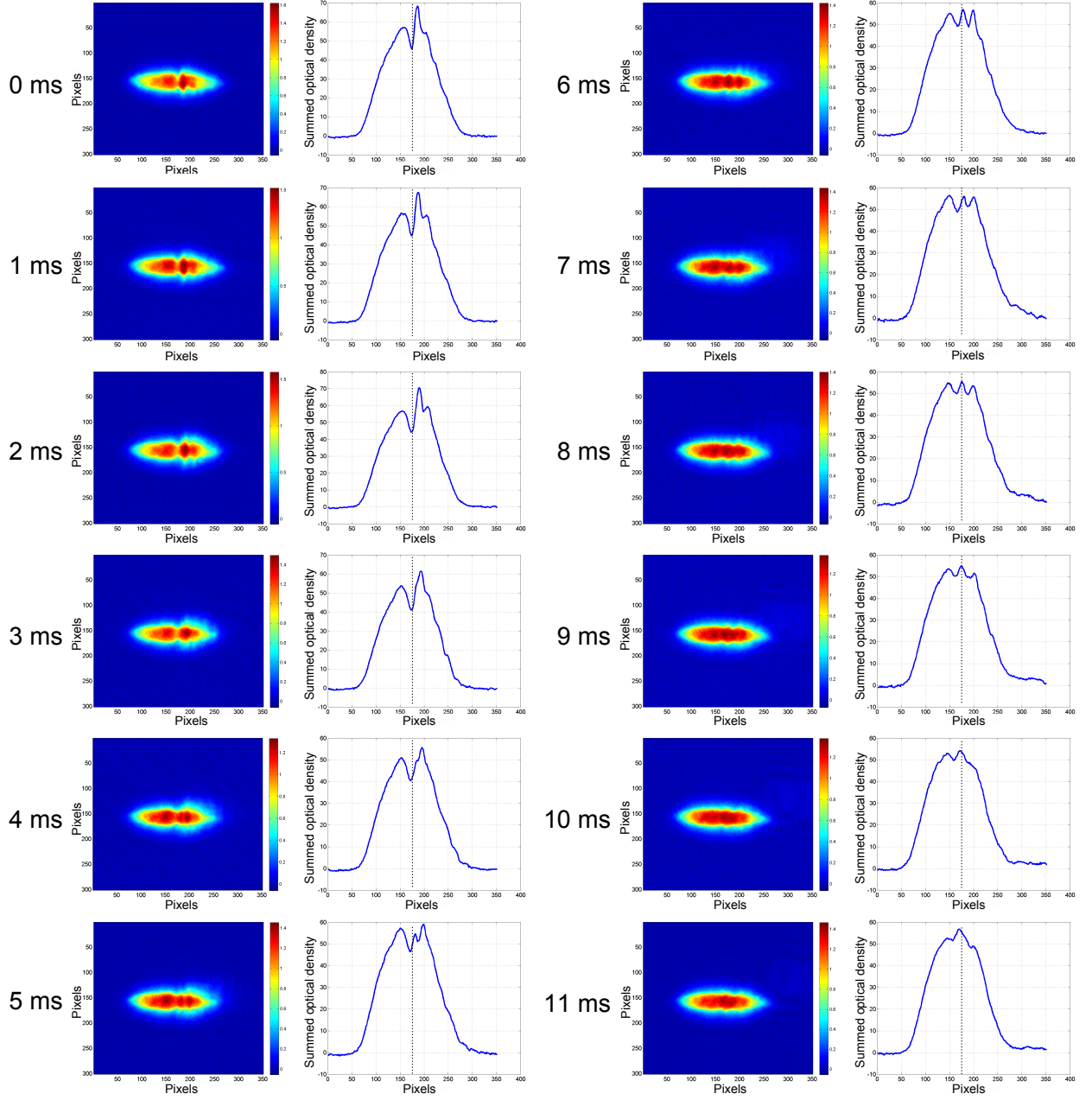
Figure 6.11: Figure showing the top view and projected optical density of the BEC with soliton-like features visible. The dashed line on the graph indicates the original position of the dip and guides the eye. It can be seen that the dip moves to the left, and less pronounced with time as the feature dissipates. The images are 300 by 350 pixels, which corresponds to 193.5 μm by 258 μm.
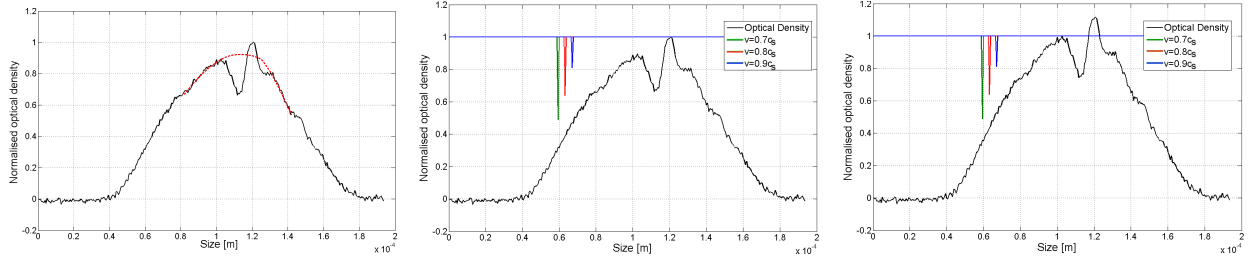
Figure 6.12: Determining boundaries of the soliton velocity. (left) Illustration of the principle that the unperturbed parabola height is between the left peak and the right peak, (middle) normalising the density to the density peak and superposing velocity profiles (for $v = 0.7c_s$ (green), $v = 0.8c_s$ (red) and $v = 0.9c_s$ (blue)) yielding a lower estimate on the soliton velocity and (right) normalising to the left peak and superposing the same velocity profiles, thereby yielding an upper estimate on the soliton velocity.

based on the lower peak yields an upper limit on the soliton velocity of $0.9c_s^{2D}$ [1], where c_s^{2D} is the speed of sound in the BEC. From the comparison normalised to the density peak, a lower limit on the soliton velocity of $0.8c_s^{2D}$ is obtained.

The velocity of the soliton can be determined from the data by recording the position of the soliton in time. The distance travelled[2] can then be calculated. The error in the determination of the position of the soliton is taken as being 0.5 pixels, yielding an error[3] on the distance of 0.7 pixels. The change in position of the soliton dip is plotted in Figure 6.13

Assuming a constant density, the velocity is estimated by fitting a function of the type $y = ax + b$, where b is allowed to vary between the values of the error only. The velocity of the soliton is given by the gradient, which from Figure 6.13 is 1.5 pixels/ms. This is converted[4] to the conventional unit of m/s and gives a soliton velocity of $(9.7 \pm 0.6) \cdot 10^{-4}$ m/s.

In order to establish the ratio of the soliton velocity to the 2D speed of sound, the value of the speed of sound given in Table 6.1 can not be used, as this is the non-expanded value of the velocity.

The expanded 2D speed of sound can be calculated by measuring the velocity of the density wave [23] (the bright peak). This velocity can be found by tracing the position of the top of the peak as a function of time by a process analogous to the one applied to determine the soliton velocity. The distance travelled by the peak as a function of time is shown in Figure 6.14, and the fit yields a gradient of (1.8 ± 0.1) pixels/ms, equivalent to $(11.6 \pm 0.6) \cdot 10^{-4}$ m/s. As expected, this value is larger than the non-expanded value of $10 \cdot 10^{-4}$ m/s presented in Table 6.1.

---

[1]Because the BEC is two-dimensional, the speed of sound needs to be dimensionally corrected, see Section 2.3.1.

[2]Assumed to be in a straight line.

[3]Standard error propagation for the type $z = x + y$: $\sigma(z) = \sqrt{\sigma(x)^2 + \sigma(y)^2}$.

[4]Conversion factor $f = \frac{100 \times gradient \times 6.45 \cdot 10^{-6}}{10}$, 10 being the magnification.

87
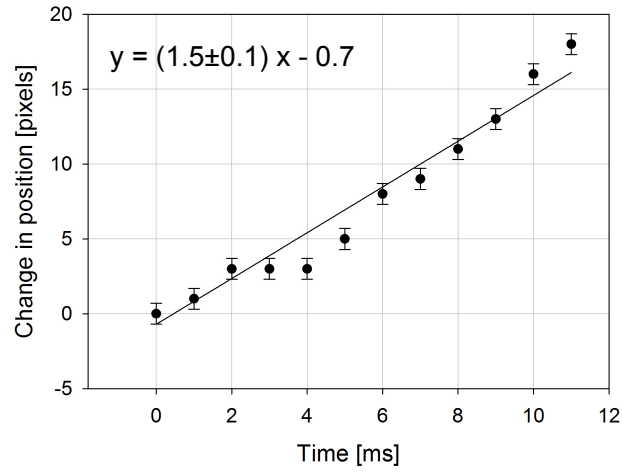
Figure 6.13: Graph showing the position of the soliton as a function of time. The fit shown yields a gradient of (1.5±0.1) pixels/ms.
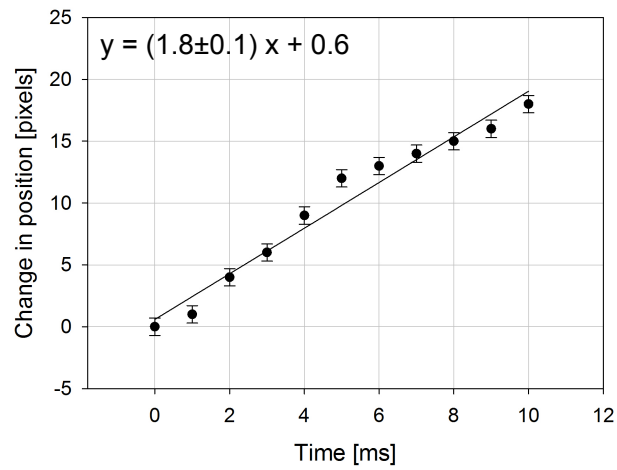
Figure 6.14: Graph showing the position of the density peak as a function of time. The fit shown yields a gradient of (1.8±0.1) pixels/ms.

Having established the value of both the speed of the soliton and the speed of sound in the expanded BEC, the fraction v/c_s can be calculated, and yields 0.83. This value is within the bounds determined previously.

Width of the soliton

Having established the ratio of the soliton velocity to the speed of sound in the condensate, the width of the soliton, in the limit of the width of the phase imprint being less than the healing length, is predicted (Equation 2.23) as being 0.9 μm, which is below the resolution of the system (Section 5.3.3).

From Figure 6.15, the (FWHM) width of the soliton is measured for different evolution times, with the results being shown in Table 6.2 and in graphical form in Figure 6.16. The width at 0 ms hold is found to be 5.2 μm. The width doubles over a 9 ms propagation. As the width of the step edge is larger than the healing length, the width of the soliton is larger than the theoretical prediction, as expected [118].
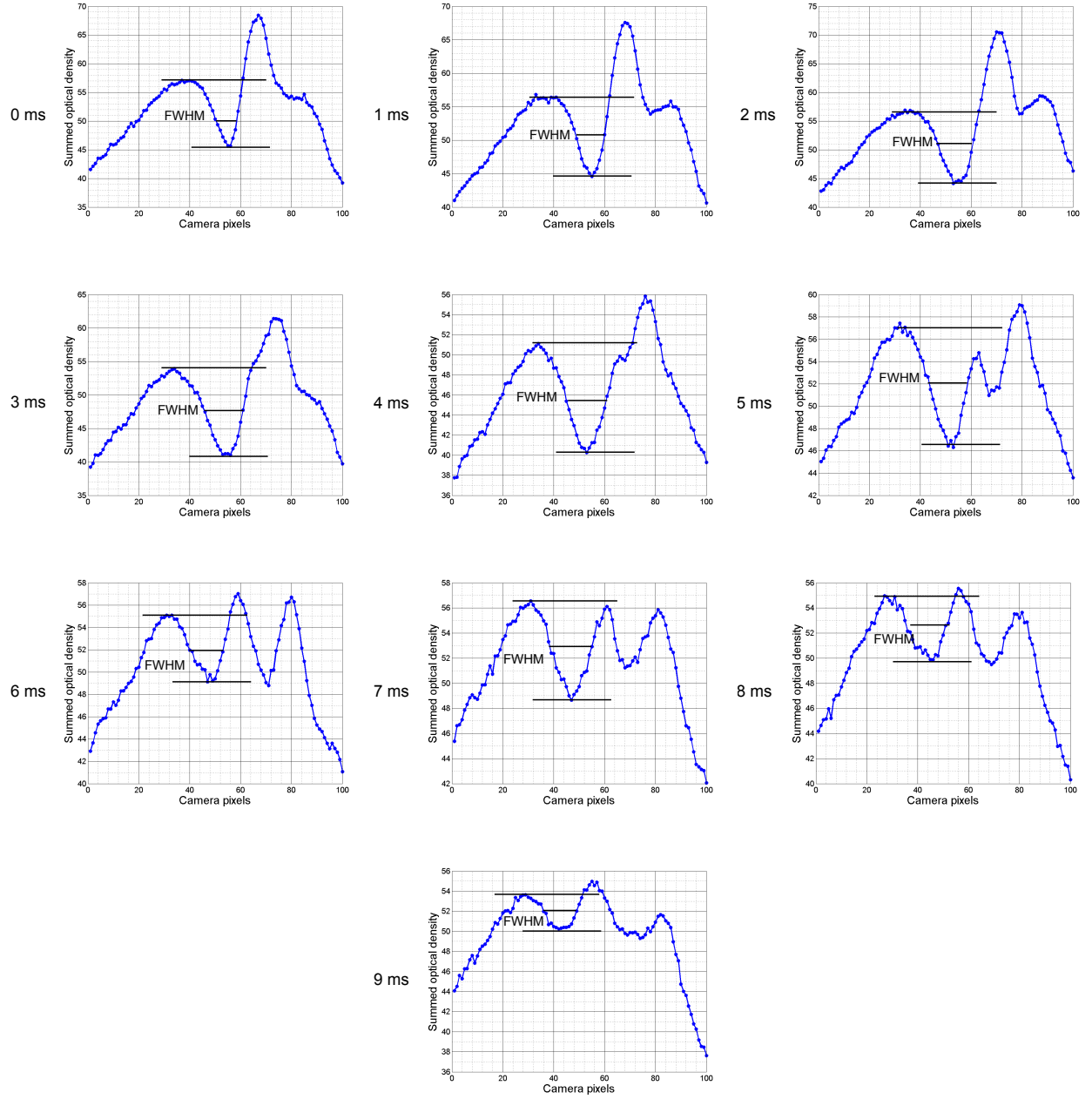
Figure 6.15: Data showing how the width of the soliton is measured for different hold times. The graphs show the summed optical density of the images. The x-axis covers 100 pixels, which corresponds to 64.5 μm.

time [ms]	width [pix]	error [pix]	width [μm]	error [μm]
0	8	1.4	5.2	0.9
1	12	1.4	7.7	0.9
2	13	1.4	8.4	0.9
3	15	1.4	9.7	0.9
4	15	1.4	9.7	0.9
5	16	1.4	10.3	0.9
6	14	1.4	9.0	0.9
7	17	1.4	11.0	0.9
8	17	1.4	11.0	0.9
9	14	1.4	9.0	0.9

Table 6.2: Table showing the width of the soliton for different evolution times. The soliton broadens with time.
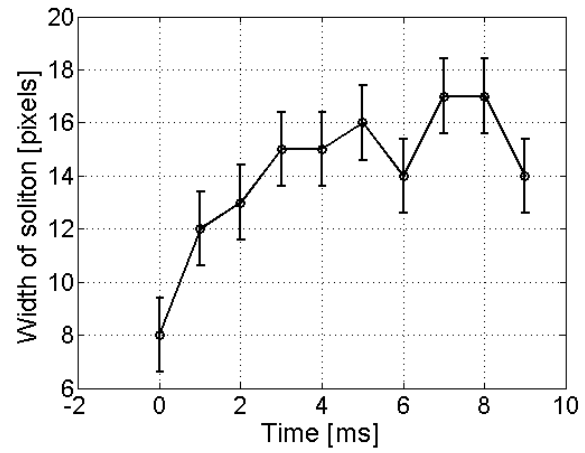
Figure 6.16: Graph showing the full width half maximum of the soliton at different evolution times. It can be noted that the soliton broadens.
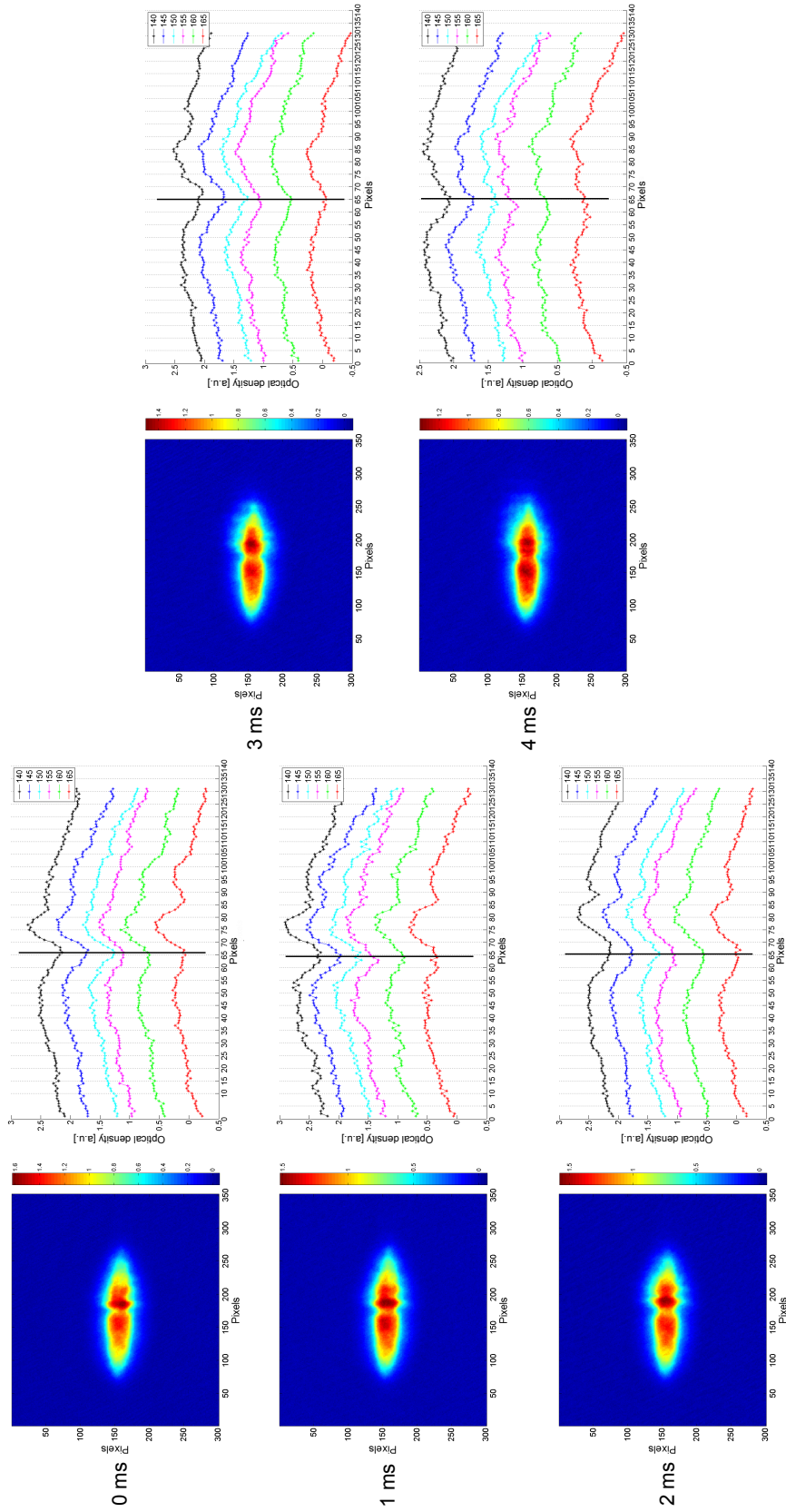
Figure 6.17: Line profiles of the BEC at different positions in the BEC for various evolution times. The black curves correspond to a cut along $y = 140$ pixels, the dark blue to $y = 145$ pixels, the light blue $y = 150$ pixels, the green to $y = 155$ pixels, the magenta to $y = 150$ pixels, and the red to $y = 165$ pixels, thereby spanning a significant portion of the width of the condensate. The profiles are offset for clarity. The vertical black line draws the eye to the lowest point of the light blue curve, to allow comparison of the position of the minima. For all the evolution times, the soliton dips fall within 2 pixels of each other, allowing no conclusion about the bending of the soliton to be drawn with the resolution available.

Curvature of the soliton

Owing to the non-uniform density in the plane the soliton is travelling in, bending of the soliton is expected. The velocity of the soliton depends on the density of the condensate. The condensate is not as dense at the edges as it is in the centre.

Line profiles are taken along the long axis (x) of the BEC, from one side to another. The cuts are taken at y = 140, 145, 150, 155, 160 and 165 pixels, thereby spanning the width of BEC. The line profiles around the soliton dip are shown in Figure 6.17. They are offset for clarity. As the line profiles span the width of the BEC, if bending is present, it is expected that on curves corresponding to the edges of the BEC the soliton dip will be further to the right than on curves corresponding to the central regions of the BEC. As shown on Figure 6.17, all soliton dips for a given evolution time are within 2 pixels of each other, leading to the conclusion that no bending can be seen with this resolution. The soliton dip blurs out at times greater than 5 ms, so no data is shown. From simulations [118], the bending is expected to be minimal in the first few milliseconds, becoming significant after hold times greater than 15 ms, which is longer than the current lifetime of the soliton.

6.5 Conclusion

In conclusion, the system is optimised for maximising the number of atoms in the MOT load and is sufficiently stable to produce a 2D BEC. With the use of the phase imprinting technique, an intensity dip which propagates is observed. From preliminary analysis, this feature displays the characteristics of a soliton, with a velocity of $0.83c_s^{2D}$ and a width of (5.2 ± 0.9) μm after a 5 ms time of flight. No bending is observed over the first 4 ms of propagation of the soliton with the resolution available. This is the first known observation of a soliton in a 2D BEC. Further analysis of the feature will lead to publications by the group.

CHAPTER 7

CONCLUSIONS

In the course of this thesis, progress has been made towards solitons in a two-dimensional condensate, and the first solitons have been observed. Technological improvements to the experimental system have been implemented.

Two sets of coils have been redesigned. For the first set of redesigned coils, a new technology has been adapted. With this technology, the potential for coolant leaks is significantly reduced as the coolant flows through a welded cavity. The new technology does result in physically thicker casings than the original technology developed for the experiment, so it cannot be used on other coils. Whilst the coil was developed for power-optimisation, the optical access has been limited. If future iterations of this set of coils is needed, a design offering more optical access should be considered.

In the redesign of the second set of coils, the focus has been on the material choice related to the electrical connectors, as this has been the failing point of the previous coils. The materials have been chosen to have coefficients of thermal expansion which are within close range of one another, in order to limit stretching of the glue due to heat induced thermal expansion and contraction of the materials which are bonded together. The adhesive bonding the electrical connectors has also been modified to a glue with more stretching. The coils have successfully been built and no failure at the electrical connectors have been observed in over one year of operation. In a future iteration of the coil design, methods of making the coils serviceable, such as the use of o-rings, rather than adhesives, to seal the casing could be considered.

With the aim of manipulating a 2D BEC, a high resolution optical imprint system has successfully been developed. The optical system demagnifies the image from a spatial light modulator and focuses the image onto the atomic plane of the condensate. The system is comprised of a tube lens and a microscope objective. The use of a spatial light modulator allows for flexibility in future uses of the system, as a myriad of patterns can be loaded onto the SLM. The characterisation of the system has shown that a resolution of 3 μm has been achieved. In order to increase the resolution of the system further, more powerful microscope objectives could be installed.

A 3D MOT which is optimised for the number of atoms has been used to create a 2D BEC in a dipole trap. The condensate features 31000 atoms and has a temperature of 88 nK. With trapping frequencies of $\omega_x = 2\pi \cdot 5.8$ Hz, $\omega_y = 2\pi \cdot 19.1$ Hz, $\omega_z = 2\pi \cdot 269.4$ Hz, the condensate is just in the two-dimensional regime.

The technique of phase imprinting has successfully been used to manipulate a condensate of ^{87}Rb, resulting in the creation of the first known soliton in a two-dimensional condensate. The soliton is currently short lived. The stability of the soliton could be increased by making the condensate more two-dimensional. Such improvements are currently under way.

With a system capable of manipulating a Bose–Einstein condensate, the experimental realisation of many different aspects of solitons or even vortices could be considered. Work towards understanding of soliton-soliton interactions could be done in the future with no additional requirements being placed on the experimental set-up. Experimental observations of the well known problem of how, or even if, solitons interact when crossing could be attempted, as the two-dimensional nature of the condensate could allow the study of solitons crossing at angles to each other, and not just head on.

APPENDIX A

DISMANTLED MOVING COILS

This appendix shows some images (Figure A.1) of the previous moving coils after their failure. The images of the inside of the coil allow unprecedented knowledge of the effects of long term exposure to the coolant to be gained. As stated in Section 4.2, the moving coils featured a slit to prevent eddy current, which led to a weakening of the structure of the casing, resulting in leaks from the main seal.

The first image shows the moving coil, with the glue on the main seal removed. The second image shows the opened moving coil, where displacement and tearing of the rubber is visible. The third image shows a close up of the rubber which has been torn away. This confirms that the rubber is not resistant to the hydrocarbon coolant used or to the flow rate, and importantly, the rubber piece which has been broken is the piece which directs the coolant flow around the coil. The fourth image shows that the glue (Resintech 111) used to fill the side cavity has also reacted to prolonged contact with the coolant. The glue has become brittle and can easily be torn. This glue was also used on the main seal of the coils.

Figure A.1: Opening of the old moving coils. (Top left) the coil with all the external glue removed, (top right) view of the internal body after opening, (bottom left) close-up of the damage to the rubber, and (bottom right) displaced brittle glue inside the cooling body.

APPENDIX B

CALCULATION OF THE SIZE OF THE CLOUD WHICH CAN PASS THROUGH THE DIFFERENTIAL PUMPING STAGE

An important aspect of the moving coil design is the ability of the coils to get the atom cloud through the differential pumping stage. This appendix offers the detailed calculations behind the numbers quoted in Chapter 4.

The velocity distribution of an atomic cloud is given by the Maxwell–Boltzmann distribution

$$f(v) = \sqrt{\left(\frac{m}{2\pi k_B T}\right)^3} 4\pi v^2 e^{-\frac{mv^2}{2k_B T}}, \tag{B.1}$$

where T is the temperature, which corresponds to the temperature of the cloud. The distribution, shown in Figure B.1 has a most probable velocity, v_p given by [37]

$$v_p = \sqrt{\frac{2k_B T}{m}}. \tag{B.2}$$

As illustrated in Figure B.1, 99.9% of the distribution fits within $3v_p$. In order to pass all of the cloud through the differential pumping stage, the atoms with this maximal velocity need to be considered.

The hottest atom velocity, v_M, is related to the most probable velocity, v_p, by $v_M = 3v_p$. The velocity of hottest atoms, v_M, can be related to a temperature, T_M, by a simple energetic argument, namely

$$\frac{3}{2}k_B T_M = \frac{1}{2}mv_M^2 \rightarrow v_M = \sqrt{\frac{3k_B T_M}{m}}. \tag{B.3}$$

The temperature of the hottest atoms is therefore given by $T_M = 6T_p$.
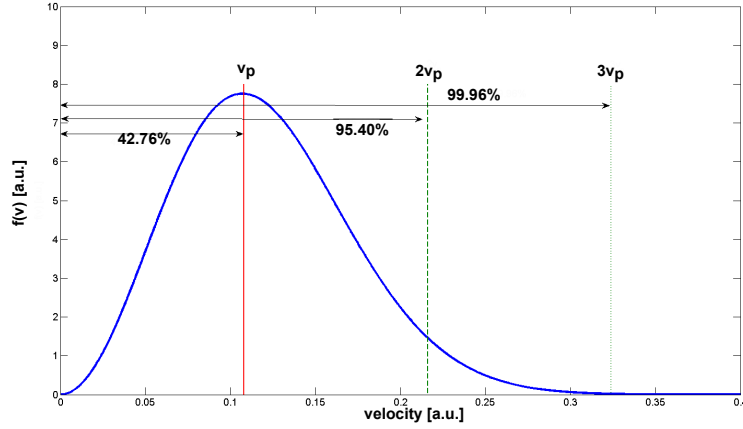
Figure B.1: The Maxwell–Boltzmann distribution

The energy due to the magnetic field can be equated to the temperature of the atoms

$$\frac{3}{2}k_B T_M = g_F m_F \mu_B B' I r, \tag{B.4}$$

where k_B is Boltzmann's constant, T_M is the maximal temperature of the cloud, g_F is the Lande g-factor of the F-state of the trapped atoms, m_F is the state of the atoms, μ_B is the Bohr magneton, B' is the magnetic gradient [in T.m^{-1}.A^{-1}], I is the current passing through the coils , and r is the radius that the atoms have to fit through. It has been assumes that the trap is a quadrupole trap. The state trapped in the experiment is the $|F = 2, m_f = 2 >$ state, with $g_F = 1/2$ [67].

Equation B.4 shows that, for a given current, the higher the gradient, the higher the temperature of the atoms can be to fit through a given radius. Conversely, is shows that for a given temperature, the radius of the cloud will be smaller with higher gradients. Rearranging Equation B.4 magnetic gradient at a given current yields

$$B'I = \frac{3}{2}\frac{k_B}{\mu_B}\frac{1}{r}T_M. \tag{B.5}$$

The gradient is given by the coils, and it therefore an experimental constant. The current can be fixed experimentally. Substituting in $r =$8 mm, and expressing T_M as a function of T_p yields

$$B'I = \frac{3}{2}\frac{k_B}{\mu_B}\frac{1}{r}6T_p = 279 \times 6T_p. \tag{B.6}$$

IV

The typical temperature of molasses is around 60μK, which yields a required magnetic field of 0.100 T. With a magnetic gradient of 0.0016 T.m^{-1}.A^{-1}, this corresponds to a current of 62 A. This statement does not take into account the warming which occurs during optical pumping and the trapping, so is a lower limit on the gradient estimate. With a power supply capable of delivering 100 A, the hottest atom cloud transportable through the differential pumping stage is $\approx$1 mK.

APPENDIX C

USAF TARGET AND DETERMINING THE RESOLUTION.

The USAF 1951 target used during the testing of the vertical illumination and detection system (see Section 5.3.3) is shown in Figure C.1. The target consists of groups, with six elements in each group. Each group and element number, corresponds to a given resolution. The resolution values, in line pair/mm [lp/mm] are given in Table C.1, for each group an element. The resolution can be converted into millimetres by taking the inverse of the line pair/mm value. The element is considered resolved if the lines can be clearly seen on the sensor, as schematically illustrated in Figure. Contrast may also affect the determined resolution, as shown in Figure
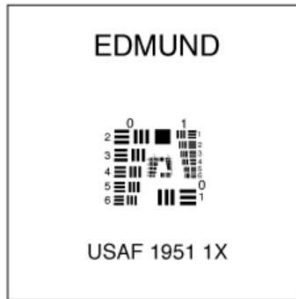
Element	Group							
	0	1	2	3	4	5	6	7
1	1.00	2.00	4.00	8.00	16.00	32.0	64	128.0
2	1.12	2.24	4.49	8.98	17.95	36.0	71.8	144.0
3	1.26	2.52	5.04	10.10	20.16	40.3	80.6	161.0
4	1.41	2.83	5.66	11.30	22.62	45.3	90.5	181
5	1.59	3.17	6.35	12.70	25.39	50.8	102.0	203.0
6	1.78	3.56	7.13	14.30	28.50	57.0	114.0	228.0

Figure C.1: USAF 1951 resolution target, from Reference [119].

Table C.1: Table showing the resolution (in lp/mm) of the USAF 1951 resolution target of each group and element. All values from Reference [119].
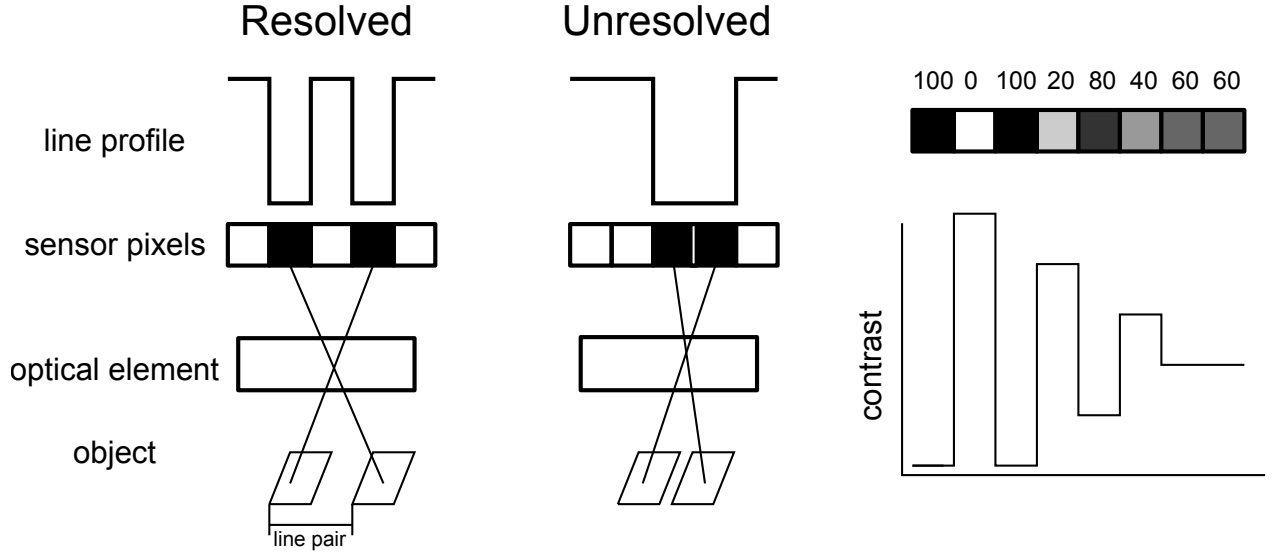
Figure C.2: Schematic representation of resolved and unresolved line pairs, and the effect of contrast on resolution. From left to right, a resolved line pair; an unresolved line pair; and an illustration of how the contrast can limit the resolution. After Reference [120].

C.1 Determining the resolution

The original image is post processed by firstly enhancing the contrast using the 'imadjust' function[1]. Line/square profiles are then taken of the target and compared. The example here, illustrates the process carried out on the focused image with the tube lens in the normal configuration with no optical elements in the beam path (see Section 5.3.3). The image is zoomed in for clarity, and the boxes show the different areas that were profiled[2]. As can be seen from the profiles shown in Figure C.4, the contrast decreases with the increase in resolution line pair. For Group 4 Element 6, the contrast is $\approx$90%, whereas for Group 5 Element 6, the contrast is reduced to 47% but a square function remains visible. Even with the low contrast (15%) of Group 6 Element 1, a square function can be seen. This is not the case for Group 6 Element 2. The resolution is therefore deemed to be Group 6 Element 1, which corresponds to 64 lp/mm, or 15.6 μm.

---

[1] J = imadjust(I) maps the intensity values in greyscale image I to new values in J such that 1% of data is saturated at low and high intensities of I. This increases the contrast of the output image J [121].

[2] using ImageJ or MATLAB.
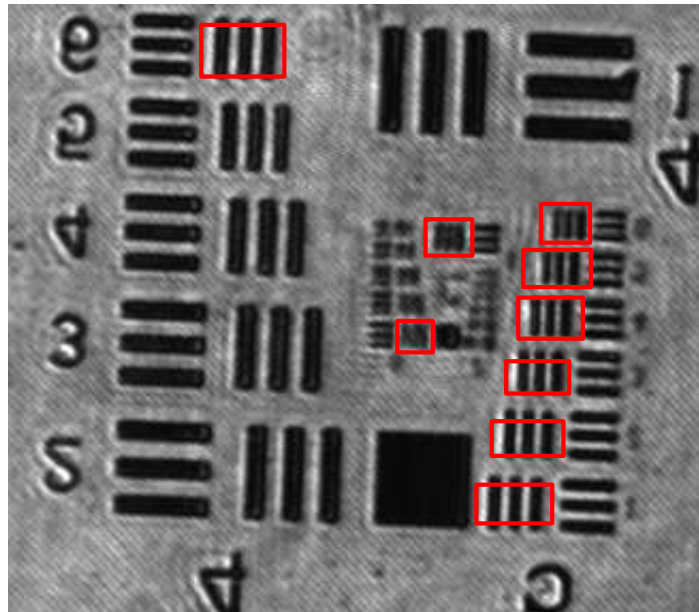
Figure C.3: Contrast adjusted and zoomed in of the image corresponding to the tube lens in the normal configuration with no optical elements in the beam path. The red boxes show the areas which were used to obtain the profiles shown in Figure C.4, with each being one of the resolution elements.
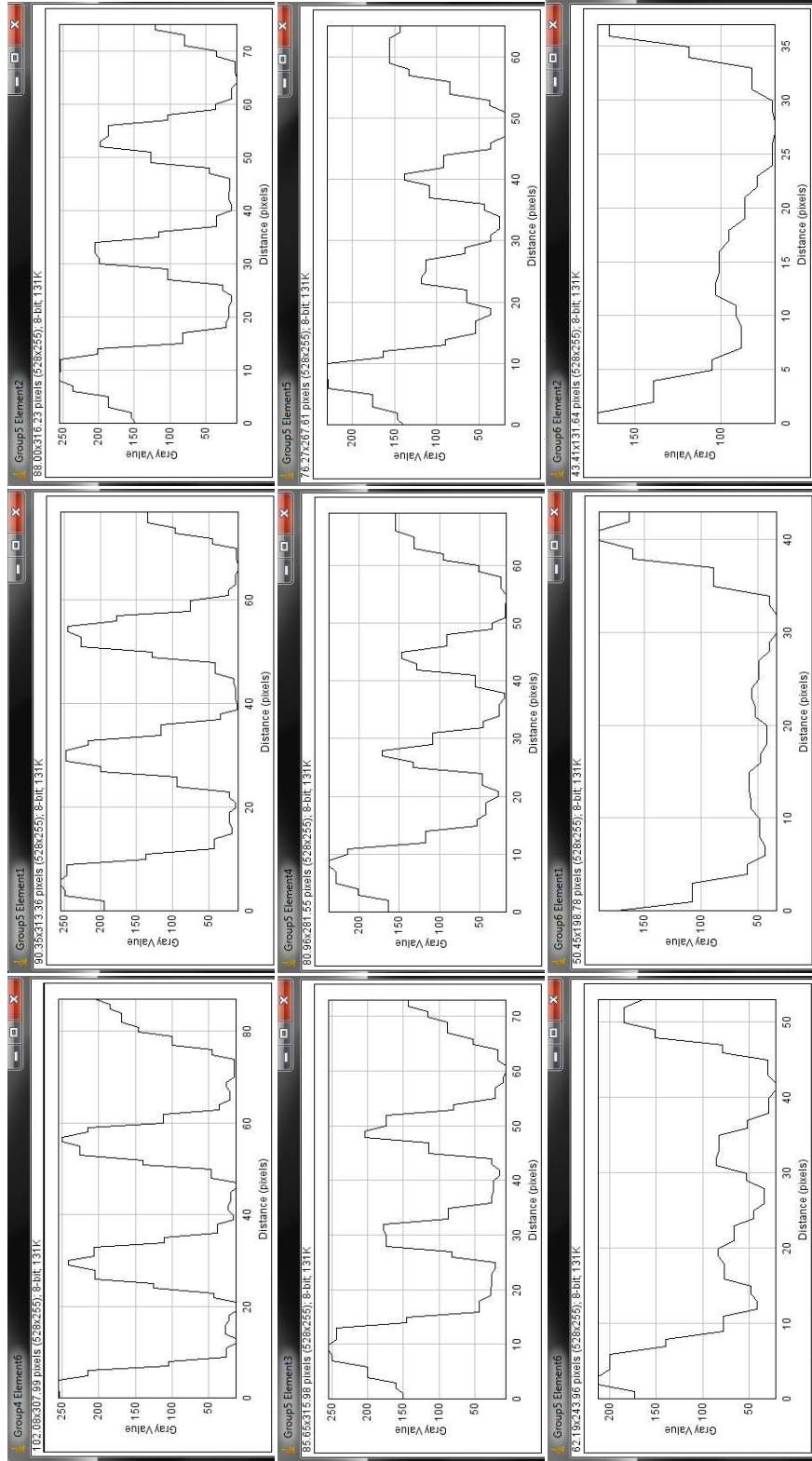
Figure C.4: Profiles corresponding to the regions shown in Figure C.3. From Left to Right, Top to Bottom, Group 4, Element 6 to Group 6 Element 2.

APPENDIX D

SNELL'S LAW AND THE DISPLACEMENT OF THE OBJECTS IN THE BEAM PATH

The numerical aperture of the tube lens is not given. Based on a $1''$ aperture of the tube lens, and the position of the focal planes at 240 mm and 160 mm, yield an half angle of $\theta = 3°$ and $\theta = 4.53°$ respectively, see Figure D.1.

The polarising beam splitter is made of glass, and therefore has an index of refraction in the range of 1.5. Using Snell's law,

$$\frac{\sin \phi_1}{\sin \phi_2} = \frac{n_2}{n_1}. \tag{D.1}$$

with the conventions illustrated in Figure D.2, gives $\phi_2 = 4.5°$ with $\phi_1 = 3°$ and $\phi_2 = 6.75°$ with $\phi_2 = 4.5°$ respectively. Because the light is entering glass from air, and exiting glass into air, the angle out of the polarising beam splitter will be the original input angle.

The difference in angle ϕ can be equated to a 'side offset', O, as illustrated in Figure D.3, equal to

$$O = L \arctan(\phi_2) - L \arctan(\phi_1), \tag{D.2}$$

where L is the length of the polarising beam splitter (25.4mm). The perpendicular offset, P, is given by (see Figure D.3)

$$P = O \cos(\phi_1). \tag{D.3}$$

In order to correct this offset, a distance of

$$x = \frac{P}{\sin \theta} \tag{D.4}$$
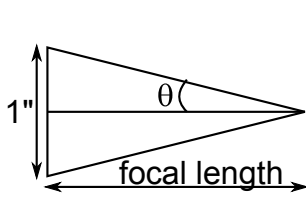
Figure D.1: Extrapolating the angle, θ of the tube lens
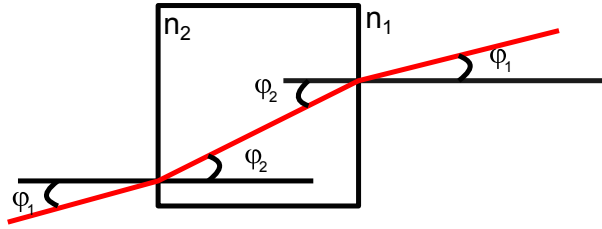
Figure D.2: Illustration of Snell's law, and the conventions used for the discussion
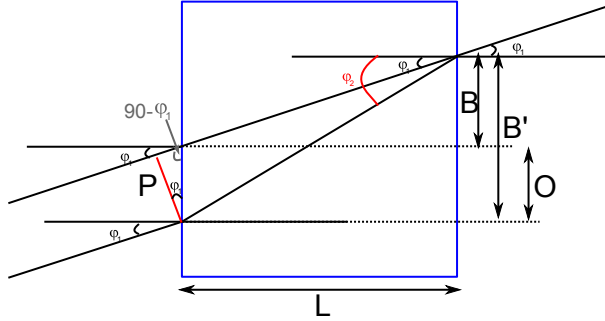
Figure D.3: Illustration of the offsets due to the polarising beam splitter, using the conventions used for the discussion.
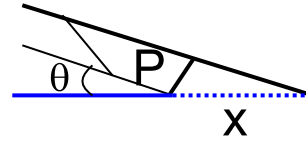
Figure D.4: Illustration of the correction along the optical axis, using the conventions used for the discussion.

needs to be travelled along the optical axis (Figure D.4). Substituting the values in leads to an offset of 12.74 mm for f=240 mm, and 12.79 mm for f=160 mm.

APPENDIX E

BEC EXPERIMENTAL SEQUENCE

The experimental sequence used to obtain the BEC in Chapter 6 is shown in Table E.1.

	time	3D cooling power [V]	3D repumping power [V]	3D AOM [MHz]	VCO [MHz]	pushing power [V]	pushing AOM [MHz]	MOT coils [A]	Moving coils [A]	Feshbach coils [A]	RF frequency [MHz]	DT value [V]
MOT 1	8s	0.6	10	80	245	2.2	77	10.2	—	—	—	—
MOT 2	22s	0.6	10	80	241	2.2	77	10.2	—	—	—	—
molasses	10 ms	0.65	5.5	80	220	—	—	—	—	—	—	—
optical pumping	1.99 ms	0.75	0	80	260	—	—	—	—	—	—	—
into MGT	1 s	—	—	—	—	—	—	—	40→83	—	—	—
transport	0.9 s	—	—	—	—	—	—	—	83	—	—	—
MGT to Fesh	1 s	—	—	—	—	—	—	—	83→0	0→55	—	—
mov Back	0.9s	—	—	—	—	—	—	—	0	55	—	—
RF evaporation 1	8 s	—	—	—	—	—	—	—	—	55	45→10	10
RF evaporation 2	4 s	—	—	—	—	—	—	—	—	55	10→3	10
transfer to DT 1	0.5 s	—	—	—	—	—	—	—	—	55→6	—	10
transfer to DT 2	0.5 s	—	—	—	—	—	—	—	—	6	—	10
DT evaporation 1	0.25 s	—	—	—	—	—	—	—	—	—	—	10→5
DT evaporation 2	1.5 s	—	—	—	—	—	—	—	—	—	—	5→1
DT evaporation 3	3 s	—	—	—	—	—	—	—	—	—	—	1→0.1
DT evaporation 4	3 s	—	—	—	—	—	—	—	—	—	—	0.1→0.04
DT hold	2 s	—	—	—	—	—	—	—	—	—	—	0.04

Table E.1: Experimental sequence used to obtain the BEC presented in Chapter 6.

LIST OF REFERENCES

[1] M. H. Anderson, J. R. Ensher, M. R. Matthews, C. E. Wieman, and E. A. Cornell. Observation of Bose–Einstein condensation in a dilute atomic vapor. *Science*, 269(5221):198–201, 1995.

[2] K. B. Davis, M. O. Mewes, M. R. Andrews, N. J. van Druten, D. S. Durfee, D. M. Kurn, and W. Ketterle. Bose–Einstein condensation in a gas of sodium atoms. *Phys. Rev. Lett.*, 75:3969–3973, Nov 1995.

[3] S. N. Bose. Plancks gesetz und lichtquantenhypothese. *Zeitschrift für Physik*, 26:178, 1924.

[4] A. Einstein. Quantentheorie des einatomigen idealen gases zweite abhandlung. *Sitzungsberichte der preussischen Akademie der Wissenschaften*, pages 3–10, 1925.

[5] A. L. Schawlow and C. H. Townes. Infrared and optical masers. *Physical Review*, 112:42–48, 1957.

[6] H. F. Hess. Evaporative cooling of magnetically trapped and compressed spin-polarized hydrogen. *Phys. Rev. B*, 34:3476–3479, Sep 1986.

[7] E. L. Raab, M. Prentiss, A. Cable, S. Chu, and D. E. Pritchard. Trapping of neutral sodium atoms with radiation pressure. *Phys. Rev. Lett.*, 59:2631–2634, Dec 1987.

[8] J. Walraven. Elements of quantum gases: Thermodynamic and collisional properties of trapped atomic gases, accessed 20/08/2014. `https://staff.fnwi.uva.nl/j.t.m.walraven/walraven/Publications_files/Elements-of-Quantum-Gases-I.pdff`.

[9] M. Greiner, C. A. Regal, and D. S. Jin. Emergence of a molecular Bose–Einstain condensate from a fermi gas. *Nature*, 426:537–540, Dec 2003.

[10] S. Inouye, M. R. Andrews, J. Stenger, H.-J. Miesner, D. M. Stamper-Kurn, and W. Ketterle. Observation of Feshbach resonances in a Bose–Einstein condensate. *Nature*, 39226:151, Mar 1998.

[11] I. Bloch. Ultracold quantum gases in optical lattices. *Nature Physics*, 1:23–30, Oct 2005.

[12] J. F. Sherson, C. Weitenberg, M. Endres, M. Cheneau, I. Bloch, and S. Kuhr. Single-atom-resolved fluorescence imaging of an atomic Mott insulator. *Nature*, 467:68–73, Sep 2010.

[13] W. S. Bakr, J. I Gillen, A. Peng, S. Fölling, and M. Greiner. A quantum gas microscope for detecting single atoms in a Hubbard-regime optical lattice. *Nature*, 462:74–77, Nov 2009.

[14] Z. Hadzibabic, P. Krüger, M. Cheneau, M. Batterlier, and J. Dalibard. Berzinskii–kosterlitz–thouless crossover in a trapped atomic gas. *Nature*, 441:1118, Jun 2006.

[15] A. Görlitz, J. M. Vogels, A. E. Leanhardt, C. Raman, T. L. Gustavson, J. R. Abo-Shaeer, A. P. Chikkatur, S. Gupta, S. Inouye, T. Rosenband, and W. Ketterle. Realization of Bose–Einstein condensates in lower dimensions. *Phys. Rev. Lett.*, 87:130402, Sep 2001.

[16] D. S. Petrov. *Bose–Einstein condensation in low-dimensional trapped gases*. PhD thesis, Universiteit van Amsterdam, 2003.

[17] D. S. Petrov, D. M. Gangardt, and G. V. Shlyapnikov. Low-dimensional trapped gases. *J. Phys. IV France*, 116:5–44, Oct 2004.

[18] B. P. Anderson. Experiments with vortices in superfluid atomc gases. *J. Low Temp Phys*, 161:574–602, 2010.

[19] M. Remoissenet. *Waves called solitons: concepts and experiments*. Springer, 2nd edition edition, 1996.

[20] V. V. Konotop and L. Pitaevskii. Landau dynamics of a grey soliton in a trapped condensate. *Physical Review Letters*, 93(24):240403, December 2004.

[21] R Carretero-Gonzlez, D J Frantzeskakis, and P G Kevrekidis. Nonlinear waves in Bose-Einstein condensates: physical relevance and mathematical techniques. *Nonlinearity*, 21(7):R139, 2008.

[22] D J Frantzeskakis. Dark solitons in atomic boseeinstein condensates: from theory to experiments. *Journal of Physics A: Mathematical and Theoretical*, 43(21):213001, 2010.

[23] S. Burger, K. Bongs, S. Dettmer, W. Ertmer, K. Sengstock, A. Sanpera, G. V. Shlyapnikov, and M. Lewenstein. Dark solitons in Bose–Einstein condensates. *Phys. Rev. Lett.*, 83:5198–5201, Dec 1999.

[24] J. Denschlag, J. E. Simsarian, D. L. Feder, C. W. Clark, L. A. Collins, J. Cubizolles, L. Deng, E. W. Hagley, K. Helmerson, W. P. Reinhardt, S. L. Rolston, B. I. Schneider, and W. D. Phillips. Generating solitons by phase engineering of a Bose–Einstein condensate. *Science*, 287(5450):97–101, 2000.

[25] Ł. Dobrek, M. Gajda, M. Lewenstein, K. Sengstock, G. Birkl, and W. Ertmer. Optical generation of vortices in trapped Bose–Einstein condensates. *Phys. Rev. A*, 60:R3381–R3384, Nov 1999.

[26] K. E. Strecker, G. B. Partridge, A. G. Truscott, and R. G. Hulet. Formation and propagation of matter-wave soliton trains. *Natures*, 417:150, May 2002.

[27] A. L. Marchant, T. P. Billam, T. P. Wiles, M. M. H. Yu, S. A. Gardiner, and S. L. Cornish. Controlled formation and reflection of a bright solitary matter wave. *Nature Communications*, 4:1865, May 2013.

[28] Z. Dutton, M. Budde, C. Slowe, and L. V. Hau. Observation of quantum shock waves created with ultra- compressed slow light pulses in a Bose–Einstein condensate. *Science*, 293(5530):663–668, 2001.

[29] S. Stellmer, C. Becker, P. Soltan-Panahi, E.-M. Richter, S. Dörscher, M. Baumert, J. Kronjäger, K. Bongs, and K. Sengstock. Collisions of dark solitons in elongated Bose–Einstein condensates. *Phys. Rev. Lett.*, 101:120406, Sep 2008.

[30] C. Becker, S. Stellmer, P. Soltan-Panahi, S. Dörscher, M. Baumert, E.-M. Richter, J. Kronjäger, K. Bongs, and K. Sengstock. Oscillations and interactions of dark and dark-bright solitons in Bose–Einstein condensates. *Nature Physics*, 4:496–501, May 2008.

[31] G. Huang, M. G. Velarde, and V. A. Makarov. Dark solitons and their head-on collisions in Bose–Einstein condensates. *Phys. Rev. A*, 64:013617, Jun 2001.

[32] G. Huang, V. A. Makarov, and M. G. Velarde. Two-dimensional solitons in Bose–Einstein condensates with a disk-shaped trap. *Phys. Rev. A*, 67:023604, Feb 2003.

[33] N. V. Hung, P. Ziń, M. Trippenbach, and B. A. Malomed. Two-dimensional solitons in media with stripe-shaped nonlinearity modulation. *Phys. Rev. E*, 82:046602, Oct 2010.

[34] S. Tsuchiya, F. Dalfovo, and L. Pitaevskii. Solitons in two-dimensional Bose–Einstein condensates. *Phys. Rev. A*, 77:045601, Apr 2008.

[35] A. E. Muryshev, H. B. van Linden van den Heuvell, and G. V. Shlyapnikov. Stability of standing matter waves in a trap. *Phys. Rev. A*, 60:R2665–R2668, Oct 1999.

[36] W. Ketterle, D. S. Durfee, and D. M. Stamper-Kurn. Making, probing and understanding Bose–Einstein condensates. *eprint arXiv:cond-mat/9904034*, April 1999.

[37] K. Huang. *Introduction to Statistical Mechanics*. Taylor and Francis, 2nd edition edition, 2001.

[38] F. Dalfovo, S. Giorgini, L. P. Pitaevskii, and S. Stringari. Theory of Bose–Einstein condensation in trapped gases. *Rev. Mod. Phys.*, 71:463–512, 1999.

[39] H.J. Metcalf and P. van der Straten. *Laser Cooling and Trapping*. Graduate Texts in Contemporary Physics. Springer, 1999.

[40] C.J. Foot. *Atomic Physics*. Oxford Master Series in Physics. Oxford University Press, 2005.

[41] H. M. J. M. Boesten, C. C. Tsai, J. R. Gardner, D. J. Heinzen, and B. J. Verhaar. Observation of a shape resonance in the collision of two cold ^{87}Rb atoms. *Phys. Rev. A*, 55:636–640, Jan 1997.

[42] C. Becker. *Multi component Bose–Einstein Condensates*. PhD thesis, University of Hamburg, 2008.

[43] P. Krüger, Z. Hadzibabic, and J. Dalibard. Critical point of an interacting two-dimensional atomic bose gas. *Phys. Rev. Lett.*, 99:040402, Jul 2007.

[44] H. Perrin. Low dimensional bose gases, part 1: Bec and interactions, accessed 20/08/2014. `http://www-lpl.univ-paris13.fr/BEC/BEC/Teaching/lecture1LowD.pdf`.

[45] K. Merloti, R. Dubessy, L. Longchambon, A. Perrin, P.-E. Pottie, V. Lorent, and H. Perrin. A two-dimensional quantum gas in a magnetic trap. *New Journal of Physics*, 15(3):033007, March 2013.

[46] S. Stringari. Dynamics of Bose–Einstein condensed gases in highly deformed traps. *Phys. Rev. A*, 58:2385–2388, Sep 1998.

[47] A. Muñoz Mateo and V. Delgado. Effective mean-field equations for cigar-shaped and disk-shaped Bose–Einstein condensates. *Phys. Rev. A*, 77:013617, Jan 2008.

[48] D. S. Petrov, M. Holzmann, and G. V. Shlyapnikov. Bose–Einstein condensation in quasi-2d trapped gases. *Phys. Rev. Lett.*, 84:2551–2555, Mar 2000.

[49] P. Cladé, C. Ryu, A. Ramanathan, K. Helmerson, and W. D. Phillips. Observation of a 2d bose gas: From thermal to quasicondensate to superfluid. *Phys. Rev. Lett.*, 102:170401, Apr 2009.

[50] S. Stringari. Collective excitations of a trapped bose-condensed gas. *Phys. Rev. Lett.*, 77:2360–2363, Sep 1996.

[51] D. S. Jin, J. R. Ensher, M. R. Matthews, C. E. Wieman, and E. A. Cornell. Collective excitations of a Bose–Einstein condensate in a dilute gas. *Phys. Rev. Lett.*, 77:420–423, Jul 1996.

[52] M.-O. Mewes, M. R. Andrews, N. J. van Druten, D. M. Kurn, D. S. Durfee, C. G. Townsend, and W. Ketterle. Collective excitations of a Bose–Einstein condensate in a magnetic trap. *Phys. Rev. Lett.*, 77:988–991, Aug 1996.

[53] K. Merloti. *Condensat de Bose–Einstein dans un piège habillé: modes collectifs d'un superfluide en dimension deux*. PhD thesis, Univeristé Paris 13, 2014.

[54] J. Fortagh and R. Kleiner. Gross pitaevskii theory, accessed 20/08/2014. `http://www.uni-tuebingen.de/fileadmin/Uni_Tuebingen/Fakultaeten/MathePhysik/Institute/PIT/Festk%C3%B6rperphysik/Dokumente/4_Gross-Pitaevskii_theory.pdf`.

[55] L. P. Pitaevskii and A. Rosch. Breathing modes and hidden symmetry of trapped atoms in two dimensions. *Phys. Rev. A*, 55:R853–R856, Feb 1997.

[56] M.J. Ablowitz. *Nonlinear Dispersive Waves*. Cambridge Texts in Applied Mathematics. Cambridge University Press, 2011.

[57] A. L. Marchant. *Formation of bright solitary matter-waves*. PhD thesis, Durham University, 2012.

[58] N. G. Parker, N. P. Proukakis, and C. S. Adams. Dark soliton dynamics in confined Bose–Einstein condensates. In Chen L. V., editor, *Focus on Soliton Research*. Nova Publishing, 2007.

[59] Y. S Kivshar and B. Luther-Davies. Dark optical solitons: physics and applications. *Phys. Rep.*, 298:81–197, 1998.

[60] A. Weller, J. P. Ronzheimer, C. Gross, J. Esteve, M. K. Oberthaler, D. J. Frantzeskakis, G. Theocharis, and P. G. Kevrekidis. Experimental observation of oscillating and interacting matter wave dark solitons. *Phys. Rev. Lett.*, 101:130401, Sep 2008.

[61] Z. Dutton, M. Budde, C. Slowe, and L. V. Hau. Observation of quantum shock waves created with ultra- compressed slow light pulses in a Bose–Einstein condensate. *Science*, 293(5530):663–668, 2001.

[62] B. P. Anderson, P. C. Haljan, C. A. Regal, D. L. Feder, L. A. Collins, C. W. Clark, and E. A. Cornell. Watching dark solitons decay into vortex rings in a Bose–Einstein condensate. *Phys. Rev. Lett.*, 86:2926–2929, Apr 2001.

[63] P. O. Fedichev and G. V. Shlyapnikov. Dissipative dynamics of a vortex state in a trapped bose-condensed gas. *Phys. Rev. A*, 60:R1779–R1782, Sep 1999.

[64] R. Grimm, M. Weidemüller, and Y. B. Ovchinnikov. Optical Dipole Traps for Neutral Atoms. *Advances in Atomic Molecular and Optical Physics*, 42:95–170, 2000.

[65] M. Holynski. *Creating a Two Dimensional Cold Mixture Experiment*. PhD thesis, University of Birmingham, 2012.

[66] N. Meyer. *Building and characterision of a dual species quantum simulator*. PhD thesis, University of Hamburg, 2014.

[67] D. A. Steck. Rudidium 87 d line data, accessed 20/06/2014. `http://steck.us/alkalidata/rubidium87numbers.pdf`.

[68] M. Hauth. *Entwicklung eines Lasersystems für das Space-Atom-Interferometer*. Diploma thesis, Hamburg, 2010.

[69] G.C. Bjorklund, M.D. Levenson, W. Lenth, and C. Ortiz. Frequency modulation (fm) spectroscopy. *Applied Physics B*, 32(3):145–152, 1983.

[70] G. Ritt, G. Cennini, C. Geckeler, and M. Weitz. Laser frequency offset locking using a side of filter technique. *Applied Physics B*, 79(3):363–365, 2004.

[71] M. Baumert. *Dipole Traps and Optical Lattices for Quantum Simulation.* PhD thesis, University of Birmingham, 2012.

[72] E. Majorana. Atomi orientati in campo magnetico variabile. *Il Nuovo Cimento*, 9(2):43–50, 1932.

[73] W. Petrich, M. H. Anderson, J. R. Ensher, and E. A. Cornell. Stable, tightly confining magnetic trap for evaporative cooling of neutral atoms. *Phys. Rev. Lett.*, 74:3352–3355, Apr 1995.

[74] D. E. Pritchard. Cooling neutral atoms in a magnetic trap for precision spectroscopy. *Phys. Rev. Lett.*, 51:1336–1339, Oct 1983.

[75] T. Esslinger, I. Bloch, and T. W. Hänsch. Bose–Einstein condensation in a quadrupole-ioffe-configuration trap. *Phys. Rev. A*, 58:R2664–R2667, Oct 1998.

[76] R. Dubessy, K. Merloti, L. Longchambon, P.-E. Pottie, T. Liennard, A. Perrin, V. Lorent, and H. Perrin. Rubidium-87 Bose–Einstein condensate in an optically plugged quadrupole trap. *Phys. Rev. A*, 85:013643, Jan 2012.

[77] T. Pyragius. Developing and building an absorption imaging system for Ultracold Atoms. *ArXiv e-prints*, 1209.3408, September 2012.

[78] M. Erhard. *Experimente mit mehrkomponentigen Bose Einstein Kondensated.* PhD thesis, University of Hamburg, 2004.

[79] M. Brinkmann. *Optimierung der Detektion und Auswertung von ^{87}Rb Spinor Kondensaten.* Diploma thesis, University of Hamburg, 2005.

[80] M. Perea Ortiz. PhD thesis, University of Birmingham, to be published.

[81] P. A. Tipler and G. Mosca. *Physics for scientists and engineers.* W.H. Freeman and Company, fifth edition edition, 2004.

[82] T. Bergeman, G. Erez, and H. J. Metcalf. Magnetostatic trapping fields for neutral atoms. *Phys. Rev. A*, 35:1535–1546, 1987.

[83] B. O. Kock. *Magneto-optical trapping of strontium for use as a mobile frequency reference.* PhD thesis, University of Birmingham, 2013.

[84] MatWeb. Copper, cu; annealed, accessed 21/08/2014. `http://www.matweb.com/search/DataSheet.aspx?MatGUID=9aebe83845c04c1db5126fada6f76f7e&ckck=1`.

[85] Resintech Ltd. Epoxy comparison chart, accessed 20/08/2014. `http://www.resitech.co.uk/products/genadhseal.htm`.

[86] Resintech Ltd. Rt111 technical data sheet, accessed 20/08/2014. `http://www.resitech.co.uk/products/genadhseal.htm`.

[87] Master Bond. Supreme 10htnd-3 product description, accessed 20/08/2014. `http://www.masterbond.com/tds/supreme-10ht-nd3`.

[88] MatWeb. Titanium, ti, accessed 21/08/2014. `http://www.matweb.com/search/DataSheet.aspx?MatGUID=66a15d609a3f4c829cb6ad08f0dafc01&ckck=1`.

[89] MatWeb. Accuratus macor machinable glass ceramic, accessed 21/08/2014. `http://www.matweb.com/search/DataSheet.aspx?MatGUID=7e5e8f5aae28433ea61febe328a9efde`.

[90] MatWeb. Victrex(r) peek 450g general purpose, accessed 21/08/2014. `http://www.matweb.com/search/DataSheet.aspx?MatGUID=ffc10b084c4e4dd6975438d9968e1292`.

[91] Rea Magnet Wire Company Inc. Technical data, accessed 01/09/2014. `http://www.reawire.com/what-we-make/technical-data/`.

[92] J.R. Welty, C. E. Wicks, R. E. Wilson, and G. Rorrer. *Fundamentals of Momentum, Heat and Mass Transfer*. Wiley, 4th edition edition, 2000.

[93] EngineeringToolBox. Hydraulic diameter, accessed 21/09/2014. `http://www.engineeringtoolbox.com/hydraulic-equivalent-diameter-d_458.html`.

[94] Paratherm. Paratherm cr heat transfer fluid, accessed 21/09/2014. `http://www.paratherm.com/heat-transfer-fluids/lowtemp/paratherm-cr/`.

[95] D. McGloin, G.C. Spalding, H. Melville, W. Sibbett, and K. Dholakia. Aplications of spatial light modulators in atom optics. *Opt. Express*, 11:158–166, 2003.

[96] M. Reicherter, T. Haist, E. U. Wagemann, and H. J. Tiziani. Optical particle trapping with computer-generated holograms written on a liquid-crystal display. *Opt. Lett.*, 24(9):608–610, May 1999.

[97] E. R. Dufresne, G. C. Spalding, M. T. Dearing, S. A. Sheets, and D. G. Grier. Computer-generated holographic optical tweezer arrays. *Review of Scientific Instruments*, 72(3):1810–1816, 2001.

[98] J. E. Curtis, B. A. Koss, and D. G. Grier. Dynamic holographic optical tweezers. *Optics Communications*, 207(16):169 – 175, 2002.

[99] R. Eriksen, V. Daria, and J. Gluckstad. Fully dynamic multiple-beam optical tweezers. *Opt. Express*, 10(14):597–602, Jul 2002.

[100] R. Dumke, M. Volk, T. Müther, F. B. J. Buchkremer, G. Birkl, and W. Ertmer. Micro-optical realization of arrays of selectively addressable dipole traps: A scalable configuration for quantum computation with atomic qubits. *Phys. Rev. Lett.*, 89:097903, Aug 2002.

[101] D. S. Tasca, R. M. Gomes, F. Toscano, P. H. Souto Ribeiro, and S. P. Walborn. Continuous-variable quantum computation with spatial degrees of freedom of photons. *Phys. Rev. A*, 83(5):052325, may 2011.

[102] M. Mestre, F. Diry, B. Viaris de Lesegno, and L. Pruvost. Cold atom guidance by a holographically-generated laguerre-gaussian laser mode. *The European Physical Journal D*, 57(1):87–94, 2010.

[103] V. Boyer, R.M. Godun, G. Smirne, Cassettari D., Chandrashekar C.M., A.B. Deb, Z.J. Laczik, and C.J. Foot. Dynamic manipulation of Bose–Einstein condensates with a spatial light modulator. *Phys. Rev. A*, 73:013402(R), 2006.

[104] R. M. W. van Bijnen, C. Ravensbergen, D. J. Bakker, G. J. Dijk, S. J. J. M. F. Kokkelmans, and E. J. D. Vredenbregt. Patterned rydberg excitation and ionisation with a spatial light modulator. *ArXiv e-prints*, 1407.6856, July 2014.

[105] Digital Light Innovations. Discovery d4100 developer's kit, accessed 28/08/2014. `https://www.dlinnovations.com/wp/?page_id=746`.

[106] Texas Instruments. Functional block diagram of dlp5500, accessed 25/08/2014. `http://www.ti.com/general/docs/datasheetdiagram.tsp?genericPartNumber=DLP5500&diagramId=321`.

[107] A. Blackmore. *Laser Speckle: Spatial Light Modulator*. Master's thesis, University of Birmingham, 2012.

[108] Mitutoyo. Microscope units and objectives, accessed 28/08/2014. `http://www.mitutoyo.com/pdf/E4191-378_010611.pdf`.

[109] Mitutoyo. Optics glossary, accessed 28/08/2014. `http://mitutoyo.nl/upload/file/Brochures/Optisch%20meten/Optics_glossary_PRNL1305.pdf`.

[110] C.E. Willis. *Laser Speckle and the use of an SLM to create an optical lattice*. Master's thesis, University of Birmingham, 2012.

[111] T. Sprawls. Physical principles of medical imaging- online textbook, accessed 25/09/2014. `http://www.sprawls.org/ppmi2/IMGCHAR/#ImagesContrast`.

[112] W. Ketterle and N.J. Van Druten. Evaporative cooling of trapped atoms. volume 37 of *Advances In Atomic, Molecular, and Optical Physics*, pages 181 – 236. Academic Press, 1996.

[113] Yu. Kagan, E. L. Surkov, and G. V. Shlyapnikov. Evolution of a bose-condensed gas under variations of the confining potential. *Phys. Rev. A*, 54:R1753–R1756, Sep 1996.

[114] Y. Castin and R. Dum. Bose–Einstein condensates in time dependent traps. *Phys. Rev. Lett.*, 77:5315–5319, Dec 1996.

[115] F Dalfovo, C Minniti, S Stringari, and L Pitaevskii. Nonlinear dynamics of a bose condensed gas. *Physics Letters A*, 227(34):259 – 264, 1997.

[116] A. L. Fetter. Quantum mechanics of Bose–Einstein condensates, accessed 22/09/2014. `http://www.iip.ufrn.br/media/pdf/natal-ii.pdf`.

[117] R. Paschotta. *Field Guide to Lasers.* SPIE press, 2008.

[118] R. Riess. Diploma thesis, University of Hamburg, to be published.

[119] Edmund Optics. 1951 usaf glass slide resolution targets, accessed 22/08/2014. `http://www.edmundoptics.com/testing-targets/test-targets/resolution-test-targets/1951-usaf-glass-slide-resolution-targets/1790`.

[120] Edmund Optics. Introduction to modular transfer function, accessed 28/09/2014. `http://www.edmundoptics.com/technical-resources-center/optics/modulation-transfer-function`.

[121] MathWorks United Kingdom. Adjust image intensity values or colormap- matlab imadjust, accessed 22/08/2014. `http://www.mathworks.co.uk/help/images/ref/imadjust.html`.